

The MOSDEF Survey: Direct-Method Metallicities and ISM Conditions at $z \sim 1.5 - 3.5$

Ryan L. Sanders,^{1*} Alice E. Shapley,² Naveen A. Reddy,^{3,4} Mariska Kriek,⁵
 Brian Siana,³ Alison L. Coil,⁶ Bahram Mobasher,³ Irene Shivaei,^{7,8}
 William R. Freeman,³ Mojegan Azadi,⁹ Sedona H. Price,¹⁰ Gene Leung,⁶
 Tara Fetherolf,³ Laura de Groot,¹¹ Tom Zick,⁵ Francesca M. Fornasini,⁹
 and Guillermo Barro¹²

¹*Department of Physics, University of California, Davis, One Shields Ave, Davis, CA 95616, USA*

²*Department of Physics & Astronomy, University of California, Los Angeles, 430 Portola Plaza, Los Angeles, CA 90095, USA*

³*Department of Physics & Astronomy, University of California, Riverside, 900 University Avenue, Riverside, CA 92521, USA*

⁴*Alfred P. Sloan Fellow*

⁵*Astronomy Department, University of California, Berkeley, CA 94720, USA*

⁶*Center for Astrophysics and Space Sciences, University of California, San Diego, 9500 Gilman Dr., La Jolla, CA 92093-0424, USA*

⁷*Department of Astronomy/Steward Observatory, 933 North Cherry Ave, Rm N204, Tucson, AZ, 85721-0065, USA*

⁸*Hubble Fellow*

⁹*Harvard-Smithsonian Center for Astrophysics, 60 Garden Street, Cambridge, MA 02138, USA*

¹⁰*Max-Planck-Institut für extraterrestrische Physik, Postfach 1312, Garching, 85741, Germany*

¹¹*Department of Physics, The College of Wooster, 1189 Beall Avenue, Wooster, OH 44691, USA*

¹²*Department of Physics, University of the Pacific, 3601 Pacific Ave, Stockton, CA 95211, USA*

Accepted XXX. Received YYY; in original form ZZZ

ABSTRACT

We present detections of [O III] λ 4363 and direct-method metallicities for star-forming galaxies at $z = 1.7 - 3.6$. We combine new measurements from the MOSFIRE Deep Evolution Field (MOSDEF) survey with literature sources to construct a sample of 18 galaxies with direct-method metallicities at $z > 1$, spanning $7.5 < 12 + \log(\text{O}/\text{H}) < 8.2$ and $\log(M_*/M_\odot) = 7 - 10$. We find that strong-line calibrations based on local analogs of high-redshift galaxies reliably reproduce the metallicity of the $z > 1$ sample on average. We construct the first mass-metallicity relation at $z > 1$ based purely on direct-method O/H, finding a slope that is consistent with strong-line results. Direct-method O/H evolves by $\lesssim 0.1$ dex at fixed M_* and SFR from $z \sim 0 - 2.2$. We employ photoionization models to constrain the ionization parameter and ionizing spectrum in the high-redshift sample. Stellar models with super-solar O/Fe and binary evolution of massive stars are required to reproduce the observed strong-line ratios. We find that the $z > 1$ sample falls on the $z \sim 0$ relation between ionization parameter and O/H, suggesting no evolution of this relation from $z \sim 0$ to $z \sim 2$. These results suggest that the offset of the strong-line ratios of this sample from local excitation sequences is driven primarily by a harder ionizing spectrum at fixed nebular metallicity compared to what is typical at $z \sim 0$, naturally explained by super-solar O/Fe at high redshift caused by rapid formation timescales. Given the extreme nature of our $z > 1$ sample, the implications for representative $z \sim 2$ galaxy samples at $\sim 10^{10} M_\odot$ are unclear, but similarities to $z > 6$ galaxies suggest that these conclusions can be extended to galaxies in the epoch of reionization.

Key words: galaxies: abundances — galaxies: high-redshift

1 INTRODUCTION

A full understanding of galaxy formation and evolution requires knowledge of the chemical enrichment of galaxies over

* E-mail: rlsand@ucdavis.edu (RLS)

cosmic time. In particular, the gas-phase oxygen abundance (metallicity) of the interstellar medium (ISM) is a sensitive probe of the cycle of baryons into and out of galaxies. The scaling of metallicity with global galaxy properties such as stellar mass (M_*) and star-formation rate (SFR) can reveal the role of gas accretion, star formation, feedback, and outflows in shaping galaxy growth (e.g., Finlator & Davé 2008; Peebles & Shankar 2011; Davé et al. 2012; Lilly et al. 2013). The shape and normalization of metallicity scaling relations also provide valuable tests of baryonic physics prescriptions adopted in numerical simulations (e.g., Ma et al. 2016; Davé et al. 2017, 2019; De Rossi et al. 2017; Torrey et al. 2018, 2019). It is thus of critical importance to obtain accurate metallicity measurements of galaxies at low and high redshifts.

A robust determination of oxygen abundance can be obtained based on atomic physics via the “direct” method. In this approach, the electron temperature of the ionized gas is determined from the ratio of a weak auroral emission line (e.g., [O III] λ 4363 in the rest-optical or O III] λ 1661,1666 in the rest-ultraviolet) to a strong emission line from the same ionic species (e.g., [O III] λ 5007). In combination with hydrogen recombination lines and strong oxygen emission features ([O II] λ 3726,3729, [O III] λ 5007), the total oxygen abundance can be derived from the electron temperature (e.g., Izotov et al. 2006; Osterbrock & Ferland 2006; Pilyugin et al. 2012; Andrews & Martini 2013; Berg et al. 2015; Croxall et al. 2015, 2016; Pilyugin & Grebel 2016).

Since auroral lines are $\sim 100\times$ fainter than the strong lines and not typically detected in the spectra of most galaxies in large spectroscopic surveys, empirical calibrations have been constructed relating strong-line ratios to direct-method metallicity using local H II regions and $z \sim 0$ galaxies with auroral-line detections (e.g., Pettini & Pagel 2004; Pilyugin & Thuan 2005; Marino et al. 2013; Pilyugin & Grebel 2016; Curti et al. 2017). Theoretical strong-line calibrations have also been developed based on photoionization models that reproduce the properties of local H II regions (e.g., Kewley & Dopita 2002; Tremonti et al. 2004; Kobulnicky & Kewley 2004; Dopita et al. 2016). Strong-line metallicity calibrations have led to a detailed understanding of galaxy metallicity scaling relations at $z \sim 0$ (e.g., Tremonti et al. 2004; Kewley & Ellison 2008; Mannucci et al. 2010; Lara-López et al. 2010; Maiolino & Mannucci 2019).

Large samples of galaxies ($N > 1000$) at $z > 1$ with rest-optical strong-line ratio measurements are now available thanks to large spectroscopic surveys including the MOSFIRE Deep Evolution Field (MOSDEF) survey (MOSDEF; Kriek et al. 2015), Keck Baryonic Structure Survey (KBSS; Steidel et al. 2014), FMOS-COSMOS (Kashino et al. 2019), and 3D-HST (Brammer et al. 2012a). Initial work to establish the metallicities of $z > 1$ galaxies across a wide range of M_* and SFR has taken place (e.g., Erb et al. 2006; Cullen et al. 2014; Steidel et al. 2014; Troncoso et al. 2014; Zahid et al. 2014b; Sanders et al. 2015, 2018; Kashino et al. 2017; Maiolino & Mannucci 2019). However, efforts to utilize these large data sets to characterize the metallicity evolution of galaxies as a function of redshift have been hindered by systematic uncertainties associated with the use of $z \sim 0$ strong-line metallicity calibrations at high redshifts.

The strong-line ratio properties of $z > 1$ star-forming galaxies suggest evolution in the physical conditions of the

ionized gas in H II regions (e.g., Kewley et al. 2013a,b; Masters et al. 2014; Steidel et al. 2014; Shapley et al. 2015; Sanders et al. 2016a; Kashino et al. 2017; Strom et al. 2017, 2018). In particular, there is evidence that the ionization parameter, hardness of the ionizing spectrum, ISM density/pressure, and/or N/O ratio evolve with redshift at fixed O/H. Much focus has been given to the position of $z \sim 2$ galaxies in the [O III] λ 5007/H β vs. [N II] λ 6584/H α (BPT; Baldwin et al. 1981) diagram, which is systematically offset from the $z \sim 0$ star-forming sequence (e.g. Shapley et al. 2005; Erb et al. 2006; Hainline et al. 2009; Steidel et al. 2014, 2016; Shapley et al. 2015; Sanders et al. 2016a; Strom et al. 2017, 2018). As a result of these evolving H II region physical conditions, metallicity calibrations produced from $z \sim 0$ empirical datasets or from photoionization models assuming $z \sim 0$ ISM conditions will yield systematically biased metallicities when applied to high-redshift samples. The precise nature of this bias is not currently known given the lack of a consensus on the nature of the ISM conditions at high redshifts.

The most straightforward approach to resolving the problem of measuring metallicities at high redshifts is to obtain determinations of metallicity via the electron temperature method, independent of $z \sim 0$ strong-line calibrations, to characterize the bias of $z \sim 0$ calibrations and understand which low-redshift samples most reliably reproduce high-redshift metallicities. Obtaining electron temperature measurements at $z > 1$ has been observationally difficult due to the extreme faintness of temperature-sensitive auroral emission lines, but efforts over the past decade have produced a sample of > 10 auroral-line measurements at $z \sim 1 - 3$ (Villar-Martín et al. 2004; Yuan & Kewley 2009; Brammer et al. 2012b; Christensen et al. 2012a,b; Stark et al. 2013, 2014; Bayliss et al. 2014; James et al. 2014; Sanders et al. 2016b; Kojima et al. 2017; Berg et al. 2018; Patrício et al. 2018; Gburek et al. 2019). Many of these $z > 1$ auroral-line detections have taken advantage of strong gravitational lensing to boost line fluxes, or otherwise target particularly bright line emitters in which auroral lines can be detected with current facilities.

In this paper, we present three new detections of [O III] λ 4363 and derive temperature-based metallicities for galaxies at $z = 1.7 - 3.6$ from the MOSDEF survey (Kriek et al. 2015), increasing the number of galaxies at $z > 1$ with [O III] λ 4363 detections by $\sim 50\%$. We combine these measurements with targets from the literature to construct the largest sample of $z > 1$ galaxies with direct-method metallicities to-date ($N = 18$). We utilize this $z > 1$ auroral-line sample to investigate the evolution of strong-line calibrations with redshift, construct metallicity scaling relations based purely on the direct method at $z > 1$ for the first time, and place constraints on the ionization parameters and ionizing spectra present in these galaxies via photoionization modeling.

This paper is organized as follows. In Section 2, we describe the observations, $z > 1$ auroral-line sample, and derived galaxy properties. Using temperature-based metallicities, we characterize the evolution of strong-line metallicity calibrations and metallicity scaling relations, including the mass-metallicity and fundamental metallicity relations, in Section 3. In Section 4, we leverage the unique combination of direct-method metallicities and photoionization models

to constrain the ionization state of the ionized ISM in star-forming galaxies at $z > 1$. However, our sample of high-redshift auroral-line emitters is not representative of typical $\sim L^*$ galaxies at $z \sim 1-3$. In Section 5, we discuss the implications of our results for representative spectroscopic samples at $z \sim 2$, extreme emission-line galaxies at $z \sim 1-2$, and typical galaxies in the epoch of reionization at $z > 6$. Finally, we summarize our results and conclusions in Section 6.

We adopt the following abbreviations for strong emission-line ratios:

$$O3 = [\text{O III}]\lambda 5007 / H\beta \quad (1)$$

$$O2 = [\text{O II}]\lambda\lambda 3726, 3729 / H\beta \quad (2)$$

$$\text{Ne3} = [\text{Ne III}]\lambda 3869 / H\beta \quad (3)$$

$$R23 = ([\text{O III}]\lambda\lambda 4959, 5007 + [\text{O II}]\lambda\lambda 3726, 3729) / H\beta \quad (4)$$

$$O32 = [\text{O III}]\lambda 5007 / ([\text{O II}]\lambda\lambda 3726, 3729) \quad (5)$$

$$\text{Ne3O2} = [\text{Ne III}]\lambda 3869 / ([\text{O II}]\lambda\lambda 3726, 3729) \quad (6)$$

Emission-line wavelengths are given in air, and all magnitudes are on the AB scale (Oke & Gunn 1983). We assume a Λ CDM cosmology with $H_0 = 70 \text{ km s}^{-1} \text{ Mpc}^{-1}$, $\Omega_m = 0.3$, and $\Omega_\Lambda = 0.7$.

2 DATA, MEASUREMENTS, & DERIVED QUANTITIES

2.1 The MOSDEF Survey

The MOSDEF survey was a four-year program that utilized the MOSFIRE spectrograph (McLean et al. 2012) on the 10 m Keck I telescope to obtain near-infrared (rest-frame optical) spectra of ~ 1500 galaxies at $1.37 \leq z \leq 3.80$ (Kriek et al. 2015). Targets were selected in the five CANDELS fields (AEGIS, COSMOS, GOODS-N, GOODS-S, and UDS; Grogin et al. 2011; Koekemoer et al. 2011) down to limiting magnitudes of $H = 24.0, 24.5, \text{ and } 25.0$ at $1.37 \leq z \leq 1.70, 2.09 \leq z \leq 2.61, \text{ and } 2.95 \leq z \leq 3.80$, respectively, as determined from *HST*/WFC3 F160W imaging. Strong rest-optical emission lines fall in near-infrared windows of atmospheric transmission in these three redshift ranges. Target selection was performed using the photometric and spectroscopic catalogs of the 3D-HST survey (Brammer et al. 2012a; Skelton et al. 2014; Momcheva et al. 2016) based on observed *H*-band magnitudes and redshifts (spectroscopic when available, otherwise photometric). Completed in 2016, the full survey targeted ~ 1500 galaxies and yielded ~ 1300 robust redshifts: ~ 300 at $z \sim 1.5$, ~ 700 at $z \sim 2.3$, and ~ 300 at $z \sim 3.4$. Exposure times were typically 1 h per filter for masks targeting galaxies in the lowest redshift bin at $z \sim 1.5$, and 2 h per filter for $z \sim 2.3$ and $z \sim 3.4$ masks. A custom IDL pipeline was used to reduce the data and produce two-dimensional science and error spectra for each slit on a mask

that has been flat-fielded, sky-subtracted, cleaned of cosmic rays, rectified, and wavelength- and flux-calibrated. One-dimensional science and error spectra were optimally extracted (Horne 1986) using **BMEP**¹ (Freeman et al. 2019) and corrected for slit losses based on the *HST*/WFC3 F160W image for each object convolved with the average seeing for each filter and mask combination (Reddy et al. 2015). Full details of the survey design, execution, and data reduction can be found in Kriek et al. (2015).

2.2 Measurements & Derived Quantities

We measured emission-line fluxes by fitting Gaussian profiles to the one-dimensional science spectra, and flux uncertainties are estimated using a Monte Carlo method by perturbing the science spectrum according to the error spectrum and remeasuring the flux 1,000 times. The uncertainty in the line flux was taken to be the 68th percentile half-width of the resulting distribution. Redshifts were measured from the highest signal-to-noise (S/N) ratio line, almost always $H\alpha$ or $[\text{O III}]\lambda 5007$.

Stellar masses (M_*) were estimated by fitting flexible stellar population synthesis models (Conroy et al. 2009) to rest-frame UV through near-infrared photometry using the spectral energy distribution (SED) fitting code **FAST** (Kriek et al. 2009). We assumed solar metallicity, constant star-formation histories, the Calzetti et al. (2000) attenuation curve, and a Chabrier (2003) initial mass function (IMF). Redshift is fixed to the spectroscopic redshift determined from strong optical emission lines. Photometry was corrected for emission line contamination based on the measured line fluxes prior to fitting.

The best-fit SED model was used to correct for the effects of stellar absorption on hydrogen Balmer emission line fluxes. Emission-line equivalent widths were measured using the observed line flux relative to the continuum level inferred from the best-fit SED model at the line center (Reddy et al. 2018). We calculated nebular reddening using the available hydrogen Balmer emission lines, assuming a Cardelli et al. (1989) extinction curve and intrinsic ratios of $H\alpha/H\beta = 2.86$, $H\gamma/H\beta = 0.468$, and $H\delta/H\beta = 0.259$ (Osterbrock & Ferland 2006). Star-formation rates (SFRs) were calculated from the dust-corrected luminosity of the highest S/N hydrogen Balmer line (always $H\alpha$ or $H\beta$) using the solar metallicity calibration of Hao et al. (2011) converted to a Chabrier (2003) IMF.

For density and $[\text{O III}]\lambda 4363$ temperature calculations, we adopted the effective collision strengths of Tayal (2007) for O II and Storey et al. (2014) for O III, with transition probabilities for both species taken from the NIST MCHF database (Fischer & Tachiev 2014). For temperature calculations using $[\text{O III}]\lambda\lambda 1661, 1666$, the Storey et al. (2014) collision strengths cannot be used since they include only five levels, and we instead employed the six-level O III collision strengths from Aggarwal & Keenan (1999). Calculations of electron temperature from $[\text{O III}]\lambda 4363$ using either set of O III collision strengths fall within $\sim 3\%$ of each

¹ Source code and installation instructions available at <https://github.com/billfreeman44/bmep>

other. When both components of the [O II] $\lambda\lambda 3726, 3729$ doublet are detected with $S/N \geq 3$, electron density was calculated using a five-level atom approximation (Sanders et al. 2016a) and solved iteratively with the electron temperature. Otherwise, an electron density of $n_e = 250 \text{ cm}^{-3}$ was assumed,² a value typical of star-forming galaxies at $z \sim 2$ (e.g., Sanders et al. 2016a; Steidel et al. 2016; Strom et al. 2017). The electron temperature of the O^{2+} zone (T_3) was determined using the IRAF routine `nebular.temden` (Shaw & Dufour 1994). The temperature of the O^+ zone (T_2) was estimated assuming the T_3 - T_2 relation of Campbell et al. (1986): $T_2 = 0.7T_3 + 3,000 \text{ K}$. The equations of Izotov et al. (2006) were used to calculate ionic abundances. The total oxygen abundance was taken to be $O/H = O^+/H + O^{2+}/H$, assuming neutral and O^{3+} contributions are negligible within the ionized nebulae. Assuming other T_3 - T_2 relations (e.g., Pilyugin et al. 2009) changes the inferred T_2 by $\lesssim 10\%$, corresponding to changes in $O/H \lesssim 0.05 \text{ dex}$ for the vast majority of our sample that are high-excitation and dominated by O^{2+} over O^+ . Thus, assuming other T_3 - T_2 relations does not affect our results.

Uncertainties on properties calculated from emission line strengths were estimated using a Monte Carlo method in which the measured line fluxes were perturbed according to their uncertainties and all such properties (reddening, equivalent widths, SFR, line ratios, density, temperature, and abundances) were remeasured 1000 times. The uncertainty on each property was taken to be the 16th and 84th percentile of the resulting distribution. In this way, uncertainties on line ratios, SFRs, temperatures, and abundances include errors on line fluxes and nebular reddening. Uncertainties on stellar masses were estimated by perturbing the photometry according to the errors and refitting the SED 500 times.

For objects taken from the literature, all properties excluding stellar masses and equivalent widths were calculated from the observed emission-line fluxes using the same method described above, such that abundances and line ratios can be fairly compared. Any exceptions to this methodology are noted in Appendices A1 and A2. Stellar masses and equivalent widths were taken from literature sources, with all masses converted to a Chabrier (2003) IMF.

2.3 Sample Selection

2.3.1 MOSDEF [O III] $\lambda 4363$ emitters

We visually inspected the spectra of all MOSDEF targets with robust redshifts and wavelength coverage of 4364.436 Å (the vacuum wavelength of [O III] $\lambda 4363$) and searched for detections of the line. We found that several galaxies with formal $S/N > 2$ for [O III] $\lambda 4363$ in fact have spurious detections due to noise associated with sky lines. After culling out such false-positives, this search yielded 6 detections of [O III] $\lambda 4363$, the spectra of which are presented in Figure 1. The 6 sources are star-forming galaxies spanning $z = 1.67 - 3.63$ with [O III] $\lambda 4363$ significance of $2.0\text{--}7.7\sigma$. While two of the galaxies (GOODS-S-41547 and COSMOS-23895) have low- S/N detections of [O III] $\lambda 4363$ (2.0σ and

2.6σ , respectively), these line identifications were made in conjunction with a precise determination of the systemic redshift and line width from multiple strong lines. Additionally, we required identification of both positive and negative traces for [O III] $\lambda 4363$ at the correct y -pixel locations (Fig. 1). None of these galaxies host an active galactic nucleus (AGN) according to their X-ray and rest-frame infrared properties (Coil et al. 2015; Azadi et al. 2017). All six targets are low-mass ($\log(M_*/M_\odot) \lesssim 9.5$) and highly star-forming ($\log(\text{sSFR}/\text{Gyr}^{-1}) \gtrsim 0.75$).

We cannot determine direct-method metallicities for two of the six targets because of wavelength coverage: AEGIS-32546 at $z = 2.01$ lacks coverage of $H\alpha$, $H\beta$, and [O II]; GOODS-S-35910 at $z = 2.65$ lacks coverage of [O III] $\lambda\lambda 4959, 5007$ and [O II]. The other four galaxies have detections of [O III] $\lambda 4363$, [O III] $\lambda\lambda 4959, 5007$, [O II], $H\beta$, and at least one other hydrogen Balmer line, comprising the MOSDEF [O III] $\lambda 4363$ emitter sample for which robust determinations of nebular reddening, electron temperature, and nebular oxygen abundance can be obtained. The emission-line fluxes of these four galaxies are given in Table 1, and their properties are presented in Table 2. The [O III] $\lambda 4363$ detection for COSMOS-1908 was previously published in Sanders et al. (2016b). We note that the emission-line fluxes and properties of COSMOS-1908 presented in this work differ slightly due to updates to the data reduction pipeline and SED fitting procedure.

We produced a composite spectrum of the four MOSDEF [O III] $\lambda 4363$ emitters following the median stacking methodology described in Sanders et al. (2018), with the exception that we normalized the spectra by [O III] $\lambda 5007$ flux instead of $H\alpha$ flux to prevent the composite electron temperature measurement from being dominated by the brightest [O III] $\lambda 5007$ emitter in the sample. The composite spectrum is displayed in Figure 2. The significance of [O III] $\lambda 4363$ in the stacked spectrum is 6.6σ . The M_* and SFR of the composite were taken to be the median M_* and SFR of the individual galaxies. Emission-line equivalent widths were derived for the composite by dividing the composite line luminosity by the median luminosity density at line center of the set of best-fit SED models of galaxies in the composite. We have confirmed that this methodology reproduces the average equivalent widths of samples of individual MOSDEF galaxies for which the lines of interest are detected. The emission line luminosities and properties derived from the MOSDEF [O III] $\lambda 4363$ emitter composite spectrum are given in Tables 1 and 2, respectively.

² When $n_e < 3,000 \text{ cm}^{-3}$, changes in density affect inferred O^{2+} electron temperatures by at most 1%.

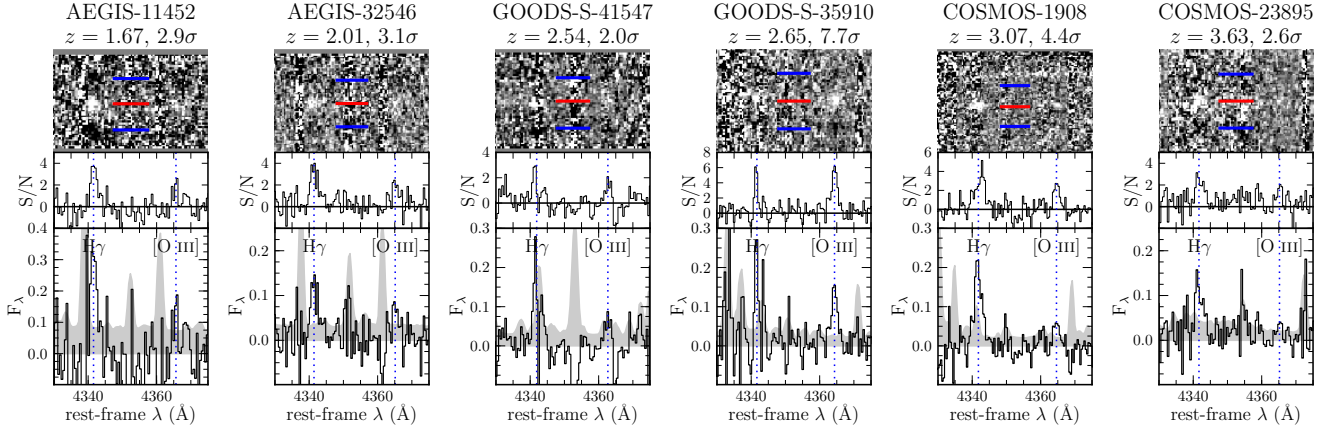


Figure 1. Spectra of MOSDEF targets with $[\text{O III}]\lambda 4363$ detections. The redshift and integrated signal-to-noise ratio (S/N) of $[\text{O III}]\lambda 4363$ are given below the object ID. TOP: Two-dimensional science spectrum. Red and blue lines show the locations of the positive and negative traces, respectively, of the target based on the y-position of strong lines. A positive and negatives can be identified for each $[\text{O III}]\lambda 4363$ detection. MIDDLE: S/N spectrum. Positive peaks in S/N can be seen for both $\text{H}\gamma$ and $[\text{O III}]\lambda 4363$. BOTTOM: One-dimensional science (black line) and error (gray shaded region) spectra. The central wavelengths of $\text{H}\gamma$ and $[\text{O III}]\lambda 4363$ are shown by dotted blue lines.

Table 1. Observed emission-line fluxes of MOSDEF $[\text{O III}]\lambda 4363$ emitters in units of $10^{-17} \text{ erg s}^{-1} \text{ cm}^{-2}$.

Object	$[\text{O II}]\lambda 3726$	$[\text{O II}]\lambda 3729$	$[\text{Ne III}]\lambda 3869$	$\text{H}\delta$	$\text{H}\gamma$	$[\text{O III}]\lambda 4363$	$\text{H}\beta$	$[\text{O III}]\lambda 5007$	$\text{H}\alpha$
AEGIS 11452	2.57 ± 0.50	4.32 ± 0.66	1.92 ± 0.30	1.93 ± 0.40	3.29 ± 0.64	0.82 ± 0.28	7.54 ± 0.35	36.1 ± 0.29	19.7 ± 0.39
GOODS-S 41547	13.3 ± 1.41	15.6 ± 0.75	—	—	5.56 ± 1.79	1.40 ± 0.70	11.1 ± 1.33	57.5 ± 0.53	31.7 ± 0.83
COSMOS 1908	1.06 ± 0.16	1.22 ± 0.14	1.74 ± 0.19	1.22 ± 0.36	2.29 ± 0.28	0.53 ± 0.12	4.82 ± 0.25	33.8 ± 0.65	—
COSMOS 23895	2.17 ± 0.35	2.18 ± 0.22	—	—	1.57 ± 0.30	0.26 ± 0.10	1.96 ± 0.21	13.1 ± 0.28	—
composite ^a	0.10 ± 0.01	0.17 ± 0.01	—	—	0.08 ± 0.007	0.02 ± 0.003	0.17 ± 0.008	1.00 ± 0.007	—

^a Line fluxes of the composite spectrum of the four MOSDEF $[\text{O III}]\lambda 4363$ emitters are reddening-corrected and normalized to $[\text{O III}]\lambda 5007$.

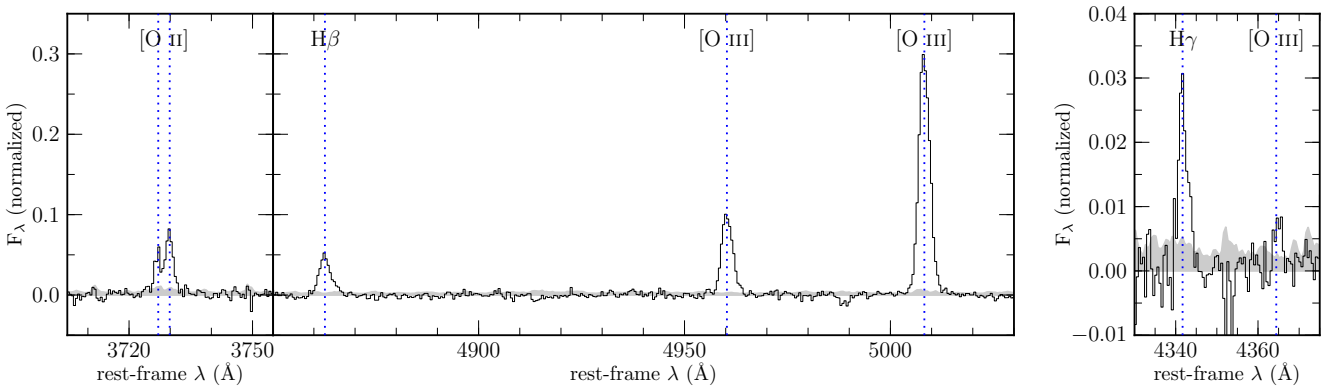


Figure 2. Composite spectrum of four MOSDEF targets with detections of $[\text{O III}]\lambda 4363$ and wavelength coverage of $[\text{O II}]\lambda 3726, 3729$, $\text{H}\beta$, and $[\text{O III}]\lambda 4959, 5007$. The gray shaded region denotes the composite error spectrum. The left and middle panels show the strong lines, while the right panel displays a zoom-in on $\text{H}\gamma$ and $[\text{O III}]\lambda 4363$. Central wavelengths of emission features are identified by blue dotted lines. The significance of $[\text{O III}]\lambda 4363$ is 6.6σ in the composite spectrum.

Table 2. Derived properties of the $z > 1$ auroral-line sample.

Object	z	$\log\left(\frac{M_*}{M_\odot}\right)$	SFR ($M_\odot \text{ yr}^{-1}$)	$\log\left(\frac{\text{sSFR}}{\text{Gyr}^{-1}}\right)$	$E(B-V)_{\text{gas}}$	n_e (cm^{-3})	T_3 (K)	$12+\log(\text{O}/\text{H})$	S/N_{aur}^i (\AA)	$\text{EW}_0([\text{O III}]\lambda 5007)$ (\AA)	$\text{EW}_0(\text{H}\beta)$
MOSDEF [O III] λ 4363											
AEGIS 11452	1.6715	$9.48^{+0.08}_{-0.36}$	17^{+1}_{-1}	$0.75^{+0.38}_{-0.08}$	$0.00^{+0.00}_{-0.00}$	$<381^a$	16200^{+3100}_{-2600}	$7.72^{+0.19}_{-0.16}$	2.9	348 ± 3	105 ± 5
GOODS-S 41547	2.5451	$9.3^{+0.13}_{-0.06}$	77^{+30}_{-18}	$1.58^{+0.14}_{-0.16}$	$0.27^{+0.13}_{-0.11}$	278^{+194}_{-176}	16800^{+4700}_{-4200}	$7.84^{+0.33}_{-0.24}$	2.0	448 ± 4	110 ± 13
COSMOS 1908	3.0767	$8.93^{+0.1}_{-0.1}$	53^{+65}_{-2}	$1.79^{+0.37}_{-0.06}$	$0.00^{+0.23}_{-0.00}$	280^{+373}_{-240}	13700^{+1800}_{-1200}	$8.02^{+0.10}_{-0.13}$	4.4	1845 ± 36	343 ± 18
COSMOS 23895	3.6372	$9.43^{+0.13}_{-0.07}$	32^{+4}_{-3}	$1.07^{+0.08}_{-0.14}$	$0.00^{+0.00}_{0.00}$	531^{+482}_{-346}	15300^{+2800}_{-3000}	$7.99^{+0.26}_{-0.17}$	2.6	491 ± 11	98 ± 11
composite	2.81^b	$9.37^{+0.05b}_{-0.14}$	42^{+2b}_{-2}	$1.25^{+0.09b}_{-0.11}$	—	$<543^a$	15400^{+2400}_{-500}	$7.90^{+0.09}_{-0.09}$	6.6	770 ± 231	120 ± 36
Literature [O III] λ 4363											
S13 ^c	1.425	$8.33^{+0.1}_{-0.14}$	7^{+1}_{-1}	$1.48^{+0.18}_{-0.09}$	$0.03^{+0.08}_{-0.03}$	201^{+132}_{-118}	15400^{+1100}_{-1000}	$7.95^{+0.07}_{-0.07}$	7.3	>320	—
J14 ^{c,d}	1.433	—	5^{+2}_{-1}	—	$0.08^{+0.09}_{-0.07}$	324^{+112}_{-120}	11700^{+2200}_{-2500}	$8.12^{+0.34}_{-0.21}$	1.7	—	—
C12a ^{c,e}	1.8339	$7.7^{+0.1}_{-0.1}$	$1.4^{+3}_{-0.9}$	$1.44^{+0.54}_{-0.44}$	$0.31^{+0.32}_{-0.34}$	171^{+204}_{-145}	20900^{+5900}_{-4000}	$7.46^{+0.23}_{-0.22}$	3.4	482 ± 124	100 ± 26
Literature O III] λ 1663											
S14a ^c	1.7024	$7.78^{+0.1}_{-0.1}$	$0.2^{+0.1}_{-0.1}$	$0.52^{+0.10}_{-0.10}$	$0.03^{+0.03}_{-0.03}$	—	13300^{+700}_{-1400}	$8.04^{+0.10}_{-0.08}$	3.5	1033 ± 100	172 ± 20
B18 ^{c,f}	1.8443	$8.26^{+0.1}_{-0.1}$	12^{+4}_{-1}	$1.82^{+0.18}_{-0.07}$	$0.00^{+0.08}_{-0.00}$	—	15400^{+1600}_{-100}	$7.52^{+0.08}_{-0.04}$	103	1575 ± 75	520 ± 40
C12b ^c	1.9634	$10.57^{+0.08}_{-0.08}$	10^{+2}_{-2}	$-0.5^{+0.12}_{-0.10}$	$0.23^{+0.01}_{-0.01}$	82^{+10}_{-10}	12400^{+400}_{-400}	$8.14^{+0.04}_{-0.03}$	7.5	—	—
S14b ^c	2.0596	$7.41^{+0.1}_{-0.1}$	$1.6^{+0.3}_{-0.1}$	$1.80^{+0.12}_{-0.09}$	$0.00^{+0.01}_{-0.00}$	—	22800^{+3500}_{-2700}	$7.30^{+0.09}_{-0.14}$	3.5	—	—
K17	2.159	$9.24^{+0.15}_{-0.15}$	14^{+19}_{-1}	$0.90^{+0.38}_{-0.11}$	$0.00^{+0.36}_{-0.04}$	—	12300^{+6100}_{-300}	$8.26^{+0.02}_{-0.30}$	6.5	—	—
Ste14c	2.1742	$8.97^{+0.1}_{-0.1}$	30^{+3}_{-1}	$1.51^{+0.12}_{-0.08}$	$0.00^{+0.04}_{-0.00}$	380^{+161}_{-142}	12700^{+800}_{-400}	$8.15^{+0.04}_{-0.06}$	5.5	1051 ± 34	170 ± 10
Ste14a	2.1889	$9.02^{+0.1}_{-0.1}$	44^{+9}_{-7}	$1.62^{+0.12}_{-0.13}$	$0.19^{+0.07}_{-0.06}$	2899^{+1385}_{-834}	14600^{+1400}_{-1100}	$8.03^{+0.06}_{-0.06}$	7.5	698 ± 68	80 ± 15
Ste14b	2.3054	$8.87^{+0.1}_{-0.1}$	27^{+4}_{-1}	$1.55^{+0.12}_{-0.08}$	$0.00^{+0.05}_{-0.00}$	781^{+220}_{-172}	12800^{+800}_{-300}	$8.10^{+0.02}_{-0.06}$	7.7	759 ± 89	102 ± 15
V04 ^c	3.357	$7.67^{+0.1g}_{-0.1}$	48^{+13}_{-9}	$3.01^{+0.16e}_{-0.14}$	$0.00^{+0.00}_{-0.00}$	—	17600^{+400}_{-400}	$7.76^{+0.04}_{-0.03}$	14.3	—	—
C12c ^c	3.5073	$9.16^{+0.21}_{-0.21}$	4^{+8}_{-1}	$0.39^{+0.60}_{-0.17}$	$0.00^{+0.23}_{-0.00}$	415^{+301}_{-206}	16200^{+6200}_{-200}	$7.76^{+0.01}_{-0.30}$	12.7	—	—
B14 ^c	3.6252	$9.5^{+0.35}_{-0.35}$	27^{+14}_{-8}	$0.93^{+0.40}_{-0.38}$	$0.32^{+0.06}_{-0.06}$	560^{+84}_{-73}	13700^{+1000}_{-1000}	$8.10^{+0.08}_{-0.08}$	6.9	—	—
KBSS-LM1 ^h	2.40^b	$9.8^{+0.3b}_{-0.3}$	$28^{+1.3}_{-1.2}$	$0.65^{+0.3}_{-0.3}$	$0.24^{+0.01}_{-0.02}$	404^{+67}_{-54}	12400^{+400}_{-400}	$8.14^{+0.03}_{-0.03}$	8.6	—	—

^a 3σ upper limit. ^b Median redshift, M_* , and SFR of the galaxies in the composite. sSFR is calculated from the median M_* and SFR. ^c Gravitationally-lensed. ^d Also has a [O III] λ 1663 detection reported in James et al. (2014). We adopt the electron temperature and O/H derived from [O III] λ 4363 (see Appendix A). ^e Also has a [O III] λ 1663 detection reported in Christensen et al. (2012b). We adopt the electron temperature and O/H derived from [O III] λ 4363 that yields smaller uncertainties. ^f Also has a [O III] λ 4363 detection reported in Brammer et al. (2012b). We adopt the electron temperature and O/H derived from [O III] λ 1663 that yields smaller uncertainties. ^g Lower limit on the total stellar mass and upper limit on sSFR. See Appendix A. ^h Composite spectrum of 30 galaxies from the KBSS survey, presented in Steidel et al. (2016). SFR and sSFR are calculated using the dust-corrected H α luminosity of the composite. ⁱ The signal-to-noise ratio on the auroral feature [O III] λ 4363 or [O III] λ 1663, as appropriate for each subsample.

2.3.2 Literature [O III] λ 4363 and O III] λ 1661,1666 emitters

We have searched the literature for galaxies at $z > 1$ with detections of [O III] λ 4363, and found 4 targets for which detections of the requisite lines to determine both dust reddening and total oxygen abundance are additionally available (Brammer et al. 2012b; Christensen et al. 2012b; Stark et al. 2013; James et al. 2014).³ Based on the work presented in Kojima et al. (2017) and Patrício et al. (2018), we have additionally compiled a sample of 12 star-forming galaxies at $z > 1$ from the literature with detections of the O III] λ 1661,1666 doublet (hereafter O III] λ 1663) with the additional detection of lines necessary to determine both the reddening correction and total oxygen abundance (Villar-Martín et al. 2004; Christensen et al. 2012a,b; Bayliss et al. 2014; Stark et al. 2014; Steidel et al. 2014; Erb et al. 2016; Kojima et al. 2017; Berg et al. 2018). The stellar masses and SFRs of literature targets that are gravitationally lensed have been corrected for magnification, and include uncertainties on the magnification when available. There are 3 literature sources that have both [O III] λ 4363 and O III] λ 1663 detections (J14, C12a, and B18). The metallicities based on either auroral line are consistent with one another in each case. We calculate the electron temperature and oxygen abundance using [O III] λ 4363 for J14, [O III] λ 4363 for C12a, and O III] λ 1663 for B18 (see Appendix A). The derived properties of the literature targets are presented in Table 2, and detailed descriptions of the calculations for each literature source are provided in Appendix A.

The literature $z > 1$ auroral sample thus comprises 14 individual galaxies, and the total $z > 1$ auroral-line sample size is 18 when combined with the MOSDEF [O III] λ 4363 emitters. The significance of the auroral-line detections ([O III] λ 4363 or O III] λ 1663) of the total sample spans $1.7 - 103\sigma$, with a median value of 6.0σ and an interquartile spanning $3.5 - 7.5\sigma$. Only two objects have $S/N < 2.5$ (GOODS-S-41547 and J14), and our results do not significantly change if these objects are excluded. For comparison, we additionally include the KBSS-LM1 composite rest-UV and rest-optical spectrum of 30 galaxies at $2.1 < z < 2.6$ from Steidel et al. (2016), with a 8.6σ O III] λ 1663 detection. The stellar mass of the KBSS-LM1 composite was taken to be the median mass of the individual galaxies. Composites are not included in any fitting function or sample median calculations.

3 DIRECT-METHOD METALLICITY CALIBRATIONS & SCALING RELATIONS AT $z > 1$

In this section, we use the largest temperature-based metallicity sample at $z > 1$ to-date to assess the applicability of several strong-line metallicity indicators from $z \sim 0 - 3.5$, construct the mass-metallicity relation based on the direct

method for the first time at $z > 1$, and investigate dependence of O/H on SFR.

3.1 Metallicity calibrations at $z > 1$

Using our sample of 18 individual galaxies at $z > 1$ with auroral-line detections and temperature-based metallicities, we investigate whether strong-line metallicity calibrations change with redshift. Recently, Patrício et al. (2018) used a sample of 16 $z > 1$ auroral-line emitters to test the reliability of various sets of strong-line metallicity calibrations at high redshifts by comparing the derived metallicity from each calibration to the temperature-based metallicity. Our approach differs from that of Patrício et al. in that we do not test specific sets of parameterized calibrations, but instead perform a purely empirical comparison of strong-line ratios at fixed direct-method metallicity between various samples to understand which calibrating samples best match the high-redshift galaxies. This empirical approach was employed in earlier works by Jones et al. (2015) at $z \sim 0.8$ and Sanders et al. (2016b) at $z \sim 1 - 3$. We perform our analysis on individual galaxies at $z > 1$ and only include stacks for comparison.

We present strong-line ratios as a function of temperature-based oxygen abundance for the $z > 1$ auroral-line sample in Figure 3. Galaxies are color-coded by redshift, while shapes encode whether [O III] λ 4363 or O III] λ 1663 was used to derive the nebular metallicity. Here, we investigate the behavior of five line ratios: O3, O2, R23, O32, and Ne3O2. We do not explore the strong-line ratios involving [N II] at this time because only 4 $z > 1$ galaxies have detections of [N II] λ 6584, while over half of the sample (10/18) does not have spectral coverage of [N II]. It is therefore not possible to draw confident conclusions about nitrogen-based metallicity indicators with the current $z > 1$ auroral-line sample. The five line-ratios presented in Figure 3 have the advantage of being accessible from the ground to $z = 3.80$, and will be observable with JWST/NIRCam and NIRSpectroscopy to $z \sim 9$.

The small sample size ($N = 18$), large typical uncertainties in O/H, and small dynamic range in metallicity ($7.5 \leq 12 + \log(O/H) \leq 8.1$; $0.07 - 0.25 Z_{\odot}$) of the $z > 1$ galaxies precludes the construction of new calibrations based on the high-redshift sample alone. While we cannot reliably constrain the shape of high-redshift metallicity calibrations, we can use mean sample properties to look for evolution in the normalization of calibrations at $12 + \log(O/H) \sim 8.0$ ($0.2 Z_{\odot}$). In each panel of Figure 3, we calculate the median $12 + \log(O/H)$ and line ratio of $z > 1$ galaxies with detections of that line ratio, displayed as black open diamonds. Limits and stacks are not included in median calculations. We note that there are at most 3 limits in any particular panel. We determine the uncertainty on median values by bootstrap resampling, perturbing the data points according to the uncertainties, and remeasuring the median 500 times. The 1σ confidence bounds are taken from the 68th percentile width of the resulting distribution. We compare the $z > 1$ sample and medians to low- and intermediate-redshift samples to investigate potential evolution: individual $z = 0$ H II regions (black line; Pilyugin & Grebel 2016; Sanders et al. 2017), $z \sim 0$ star-forming galaxies from the Sloan Digital Sky Survey (SDSS, gray points; Izotov et al. 2006), and $z \sim 0.8$ star-forming galaxies from DEEP2 (orange points; Jones et al.

³ Yuan & Kewley (2009) also reported a detection of [O III] λ 4363 in a lensed $z = 1.706$ star-forming galaxy. The claimed detection appears to be a misidentification of H γ , as described in Appendix A3. Accordingly, we do not include the source from Yuan & Kewley (2009) in our sample.

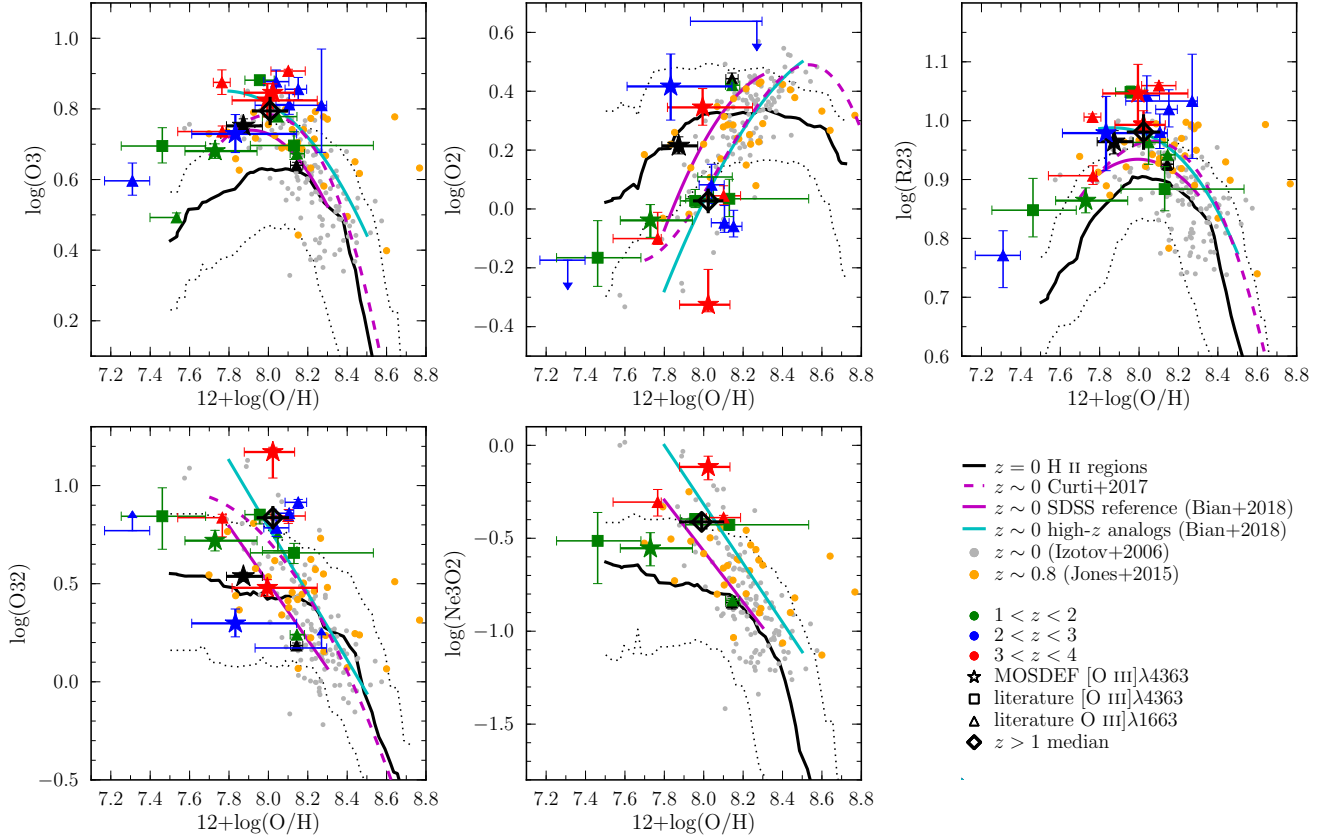


Figure 3. Strong optical emission-line ratios vs. direct-method metallicity for $z > 1$ galaxies and low-redshift samples. Points are color-coded by redshift and shapes show the auroral line used for electron temperature calculation ($[\text{O III}]\lambda 4363$ or $[\text{O III}]\lambda 1663$). MOSDEF targets are given by stars. The composite spectra of MOSDEF $[\text{O III}]\lambda 4363$ emitters and Steidel et al. (2016, KBSS-LM1) are shown as a black star and triangle, respectively. The median of individual $z > 1$ galaxies is given by the black open diamond in each panel. The low-redshift comparison samples include galaxies at $z \sim 0$ (gray circles; Izotov et al. 2006) and $z \sim 0.8$ (orange circles; Jones et al. 2015). The cyan line shows the best-fit relations of local analogs of $z \sim 2$ galaxies from Bian et al. (2018), while the magenta line displays their local reference sample. The dashed magenta line shows the $z \sim 0$ calibrations of Curti et al. (2017). The median relation and 68th percentile scatter of individual $z = 0$ H II regions are displayed, respectively, by the solid and dotted black lines. The median of the $z > 1$ galaxies is well-matched to the $z \sim 0$ Izotov et al. (2006) and $z \sim 0.8$ Jones et al. (2015) samples, and closely matches the Bian et al. (2018) high-redshift analog relations for all 5 line ratios.

2015). The oxygen abundances of each sample have been recalculated using our methodology.

Considering the $z > 1$ sample alone, we find that O3 and R23 are saturated over the range of metallicity spanned by the bulk of the high-redshift galaxies ($7.7 < 12 + \log(\text{O}/\text{H}) < 8.1$; $0.1 - 0.25 Z_{\odot}$), which reside in the turnover regime between the “upper” and “lower” branches of these indices. O3 and R23 thus cannot be utilized as reliable metallicity indicators for high-redshift galaxies falling in this oxygen abundance range, even when used in combination with an additional line-ratio to break the upper/lower branch degeneracy. Earlier works have highlighted similar issues with obtaining metallicities from R23 at $z \sim 2$ (Steidel et al. 2014; Sanders et al. 2018). The $z > 1$ galaxies display a wide dynamic range in O2, but the scatter in line ratio at fixed O/H is largest for O2, suggesting that O2 is a poor metallicity indicator at $z > 1$ as well. The large scatter

in O2 at fixed O/H may signify significant galaxy-to-galaxy variation in the nebular attenuation curve at $z > 1$.

In contrast, O32 and Ne3O2 have a monotonic dependence on direct-method metallicity for all of the samples displayed in Figure 3. The number of $z > 1$ galaxies with $[\text{Ne III}]$ detections is small and thus scatter is difficult to evaluate, but the scatter in O32 at fixed O/H of the $z > 1$ sample is comparable to that of the lower-redshift samples after accounting for measurement uncertainties (typically much larger at $z > 1$). O32 thus appears to be the best strong-line metallicity indicator for $z > 1$ samples with nebular metallicities $\lesssim 1/3 Z_{\odot}$, displaying the highest utility over the range of metallicities in our sample. Given the tight relation between O32 and Ne3O2 at sub-solar metallicities (Levesque & Richardson 2014; Strom et al. 2017), Ne3O2 should perform equally well and has the additional advantage of not requiring a reddening-correction.

The $z > 1$ auroral-line sample displays significantly

higher excitation than local H II regions at fixed O/H, with higher O3, O32, and Ne3O2 and lower O2 on average. The $z > 1$ sample also has significantly higher R23 values than are typical of the local H II regions. While in reasonable agreement at $12+\log(\text{O}/\text{H}) \sim 8.3$, the H II regions diverge from the $z \sim 0$ and $z > 1$ galaxy samples at $12+\log(\text{O}/\text{H}) < 8.0$, flattening in O32 and Ne3O2 and dropping off steeply in O3 and R23. This divergent behavior may indicate that the local H II region sample is significantly incomplete in the metal-poor regime, lacking high-excitation star-forming regions that must be present in star-forming galaxies with high O32 based on integrated spectra. We caution against utilizing empirical calibrations based on individual local H II regions at oxygen abundances below $0.2 Z_{\odot}$ ($12+\log(\text{O}/\text{H})=8.0$) for either low- or high-redshift galaxies.

Bian et al. (2018, hereafter BKD18) recently constructed metallicity calibrations for use at high redshifts by stacking spectra of $z \sim 0$ galaxies from SDSS that fall in the same region of the BPT diagram as $z \sim 2$ galaxies, and deriving temperature-based metallicities from these stacks. Their approach differs from past studies that have selected analogs based on global galaxy properties (e.g., sSFR; Brown et al. 2016; Cowie et al. 2016) in that BKD18 have selected high-redshift analogs based directly on strong-line ratios that should be more closely linked to the local gas conditions in H II regions. Stacks of a local reference sample that traces the average $z \sim 0$ BPT sequence were also constructed. Functional fits to the BKD18 high-redshift analogs and $z \sim 0$ reference sample are shown in Figure 3 (cyan and magenta lines, respectively). We find that the median of the $z > 1$ sample (black diamonds) closely matches the high-redshift analogs in O3, O2, R23, and O32 at fixed O/H, being $\geq 2\sigma$ inconsistent with the $z \sim 0$ reference sample in each case. For Ne3O2, the $z > 1$ median falls midway between the high-redshift analog and $z \sim 0$ reference lines, displaying 1σ consistency with both. [Ne III] detections were only reported for 8 out of 18 galaxies in our $z > 1$ sample. Consequently, the median O/H uncertainty is largest in the Ne3O2 panel. Collectively, the panels in Figure 3 demonstrate that the high-redshift analog calibrations of BKD18 reliably reproduce the properties of the $z > 1$ auroral-line sample on average, while the $z \sim 0$ reference calibrations fail to do so.

We additionally show the $z \sim 0$ empirical metallicity calibrations of Curti et al. (2017, hereafter C17) in Figure 3 (dashed magenta lines). The $z > 1$ median values display good agreement with the C17 $z \sim 0$ O3, O2, R23, and O32 calibrations. At first glance, this consistency appears to suggest negligible evolution in strong-line calibrations with redshift. However, this is not the case when the calibration sample of C17 is considered. C17 stacked SDSS galaxies in bins of strong-line ratio in the O3 vs. O2 diagram. The composites only reach down to $12+\log(\text{O}/\text{H}) \approx 8.1$, and C17 supplemented the stacked sample using individual SDSS galaxies with [O III] $\lambda 4363$ detected at $>10\sigma$ to extend the calibrations to $12+\log(\text{O}/\text{H}) \approx 7.7$. The C17 fits are dominated by this individual [O III] $\lambda 4363$ -detected sample at $12+\log(\text{O}/\text{H}) \leq 8.4$, the region of overlap with our $z > 1$ sample and the BKD18 calibrations. The stringent S/N cut on the faint auroral line leads to a sample that is biased significantly high in sSFR compared to typical $z \sim 0$ galaxies, with 80% lying ≥ 0.7 dex above the mean $z \sim 0$ M_* -SFR relation and the bulk of the sample scattering around the $z \sim 2$ M_* -SFR relation

and coincident with the BKD18 high-redshift analogs (see Appendix B). Thus, at $12+\log(\text{O}/\text{H}) \lesssim 8.4$, the C17 calibration sample is largely composed of high-redshift analogs that have ISM conditions shifted away from the local norm and towards what is typical at $z > 1$. The coincidence of the C17 calibrations with the $z > 1$ median values in Figure 3 is therefore *not* indicative of redshift invariant metallicity calibrations, but is instead a reflection of the C17 calibrations tracing normal $z \sim 0$ ISM conditions at high metallicities ($12+\log(\text{O}/\text{H}) \gtrsim 8.4$) and extreme ISM conditions typical of $z > 1$ at low metallicities ($12+\log(\text{O}/\text{H}) \lesssim 8.4$).

Interestingly, the Izotov et al. (2006) $z \sim 0$ SDSS sample does not follow the BKD18 local reference sample, but instead lies in between the reference and high-redshift analog lines. Similarly to the case of the C17 [O III] $\lambda 4363$ -detected SDSS sample, this trend is due to the requirement of a [O III] $\lambda 4363$ detection and large H β flux by Izotov et al. (2006), which preferentially selects high-sSFR and high-excitation galaxies with bright [O III] $\lambda 4363$. Such galaxies likely have ISM conditions that are shifted away from the local average and towards what is typical at high redshift. Thus, the Izotov et al. (2006) sample is not representative of $z \sim 0$ galaxies, but instead matches the $z > 1$ sample suitably well within the current uncertainties. Jones et al. (2015) have previously shown that their [O III] $\lambda 4363$ sample at $z \sim 0.8$ matches the Izotov et al. (2006) sample in these line-ratio vs. O/H spaces, and we find that the $z \sim 0.8$ galaxies also agree with the $z > 1$ sample on average.

In summary, the median O3, O2, R23, O32, and Ne3O2 of 18 individual $z > 1$ galaxies agree with the values for the Izotov et al. (2006) $z \sim 0$, Jones et al. (2015) $z \sim 0.8$, and BKD18 high-redshift analog samples at fixed temperature-based O/H. In contrast, the $z > 1$ sample displays systematically higher excitation at fixed O/H compared to the BKD18 SDSS local reference sample and individual $z \sim 0$ H II regions. Calibrations based on $z = 0$ H II regions are not reliable at $z > 1$ for $12+\log(\text{O}/\text{H}) \lesssim 8.0$ ($0.2 Z_{\odot}$). Calibrations based on typical $z \sim 0$ galaxies tend to underestimate O/H at $z > 1$ by $\sim 0.1 - 0.3$ dex on average. The BKD18 high-redshift analog O32 and Ne3O2 calibrations display the highest utility for application at high redshifts, reproducing the metallicities of our $z > 1$ auroral-line sample to within ~ 0.1 dex on average while maintaining a monotonic sensitivity to O/H.

We stress that these conclusions only apply over the range of metallicities probed by our $z > 1$ auroral-line sample ($7.5 \leq 12+\log(\text{O}/\text{H}) \leq 8.1$; $0.07 - 0.25 Z_{\odot}$), and only for galaxies with similar properties (i.e., low M_* and high sSFR). The $z > 1$ sample presented in Figure 3 is not representative of typical galaxies at $z \sim 1 - 3$ in large rest-optical spectroscopic surveys (e.g., MOSDEF, KBSS, 3D-HST, FMOS-COSMOS), which have $\log(M_*/M_{\odot}) \sim 10.0$ and lie on the mean M_* -SFR relation (Kriek et al. 2015; Steidel et al. 2014; Brammer et al. 2012a; Kashino et al. 2019). Based on commonly applied $z \sim 0$ strong-line methods, the majority of $z \sim 2$ galaxies at $\log(M_*/M_{\odot}) > 9.5$ are expected to have higher O/H than our $z > 1$ auroral-line sample (Steidel et al. 2014; Sanders et al. 2015, 2018), even when allowing for a factor of two systematic uncertainty in strong-line metallicities. We discuss implications for the typical $z \sim 1 - 3$ galaxy population in Section 5.1. Additionally, our conclusions regarding metallicity calibration evolution are based on the mean properties of the $z > 1$ sample, and a detailed

analysis of the scatter awaits a larger sample. We thus caution that the stated < 0.1 dex precision of the BKD18 high-redshift analog calibrations is applicable for population averages only, and that the metallicity of an individual galaxy may not be well-determined using this method.

3.2 Direct-method metallicity scaling relations at $z > 1$

The $z > 1$ auroral-line sample spans a wide dynamic range in stellar mass, with $\log(M_*/M_\odot) \sim 7.5 - 10.0$. We use this sample to explore the dependence of gas-phase oxygen abundance on stellar mass based entirely on direct-method metallicities for the first time at $z > 1$, and constrain the evolution of the mass-metallicity relation (MZR) from $z \sim 0$ to $z \sim 2$. Two galaxies in the $z > 1$ auroral-line sample (C12b and C12c) are identified as possible ongoing mergers due to morphology and close companions (Christensen et al. 2012a; Patrício et al. 2016). Mergers in the local universe have been shown to deviate from the mean $z \sim 0$ MZR, having systematically lower metallicities and higher SFRs at fixed M_* (Ellison et al. 2008; Scudder et al. 2012). In contrast, recent theoretical and observational work suggests that the SFR and O/H of close galaxy pairs may not be systematically offset from isolated galaxies at $z \sim 2$ (Fensch et al. 2017; Wilson et al. 2019). However, it is not clear if the two potential mergers in our sample fall into the merger stage and pair separation over which such conclusions are valid. To avoid introducing systematic biases from these merging systems, we exclude them from the sample used to construct metallicity scaling relations with global galaxy properties (SFR and M_*). We show these two excluded mergers as open triangles in the figures in this section and discuss their behavior in comparison to the rest of the $z > 1$ sample where appropriate. We also exclude J14, which lacks a reliable M_* estimate, and V04, which does not have a total M_* determination available (see Appendix A).

In the sections below, we investigate the shape and evolution of the MZR and its dependence on SFR. In Section 3.2.1, we present the MZR at $z \sim 2.2$ based purely on direct-method metallicities. We begin with the correlation between M_* and O/H displayed by the derived properties given in Table 2, and then correct for biases in the SFR and redshift distributions of the $z > 1$ auroral-line sample to produce a direct-method MZR representative of typical star-forming galaxies at $z \sim 2$ (equation 11). In Section 3.2.2, we investigate the evolution of the relation between M_* , SFR, and direct-method O/H from $z \sim 0 - 2.2$. We consider systematic effects on the comparison of galaxy properties of the low- and high-redshift samples in Section 3.2.3.

3.2.1 The direct-method $z \sim 2.2$ mass-metallicity relation

With the remaining high-redshift auroral-line sample of 14 galaxies, we construct the direct-method MZR at $z > 1$ for the first time, shown in the left panel of Figure 4. The median redshift of the $z > 1$ MZR sample is $z_{\text{med}} = 2.17$. We calculate mean values in two bins of stellar mass divided at $\log(M_*/M_\odot) = 8.5$, with 5 galaxies in the low-mass bin and 9 galaxies in the high-mass bin. The binned means are shown in Figure 4 as black open diamonds, with $\log(M_*^{\text{mean}}/M_\odot) =$

$[7.90 \pm 0.16, 9.19 \pm 0.10]$ and $12 + \log(\text{O}/\text{H})^{\text{mean}} = [7.66 \pm 0.14, 8.03 \pm 0.08]$ for the low- and high-mass bins, respectively. We observe a positive correlation between direct-method O/H and M_* for both the means and individual galaxies, though with significant scatter for the latter. Using an orthogonal distance regression, we fit a linear relation to the 14 individual $z > 1$ galaxies (excluding the open triangles and stacks), obtaining:

$$12 + \log(\text{O}/\text{H}) = (0.277 \pm 0.081) \times \log(M_*/M_\odot) + (5.48 \pm 0.70) \quad (7)$$

with a strong covariance between slope and intercept of $\rho = 0.9975$. The best-fit line is shown in the left panel of Figure 4 as a solid blue line. The $z > 1$ mergers do not appear to be strong outliers compared to the full $z > 1$ sample.

We compare to two $z < 1$ samples with auroral-line detections to investigate metallicity evolution at fixed M_* . The M_* -binned $z \sim 0$ SDSS stacks of Andrews & Martini (2013) are shown as gray squares in the left panel of Figure 4. The open squares show the values derived by Andrews & Martini (2013), while the filled squares denote the derived metallicities after correcting for contamination from diffuse ionized gas (DIG) according to Sanders et al. (2017), shifted ~ 0.05 dex lower in O/H. The orange line shows the best-fit MZR to a sample of $z \sim 0.8$ galaxies with [O III] $\lambda 4363$ detections from Ly et al. (2016). The $z \sim 0.8$ MZR lies approximately midway between the $z \sim 0$ and $z \sim 2.2$ MZRs. Compared to $z \sim 0$, we find that O/H at fixed M_* is 0.3 dex lower at $z \sim 0.8$ and 0.55 dex lower at $z \sim 2.2$ at $\log(M_*/M_\odot) \approx 9.2$, where the majority of the $z > 1$ auroral-line sample lies. This amount of metallicity evolution is larger than is seen in studies using strong-line methods on representative samples of galaxies at similar M_* , which find 0.3 – 0.4 dex evolution between $z \sim 0$ and $z \sim 2.3$ (Erb et al. 2006; Steidel et al. 2014; Sanders et al. 2015, 2018).

A major concern when comparing the gas-phase metallicities of different samples is how representative the SFRs are over the range of M_* . In the local universe, there is a well-established relationship between M_* , SFR, and O/H such that galaxies with higher SFR have lower O/H at fixed M_* , known as the “fundamental metallicity relation” (FMR; e.g., Mannucci et al. 2010; Lara-López et al. 2010; Yates et al. 2012; Andrews & Martini 2013; Salim et al. 2014; Cresci et al. 2019). A M_* -SFR-O/H relation has also been shown to exist at $z \sim 1 - 2.5$ using strong-line metallicities with a similar strength of SFR dependence as at $z \sim 0$ (Zahid et al. 2014b; Sanders et al. 2018). Thus, if a sample is biased in SFR at fixed M_* , then its metallicity will not be representative of typical galaxies at the same M_* . Samples selected to have detections of [O III] $\lambda 4363$ are often biased towards higher SFR at fixed M_* due to the faintness of the feature, and thus the MZR evolution displayed in the left panel of Figure 4 may be artificially large.

In Figure 5, we place the $z > 1$ auroral-line sample on the M_* -SFR diagram. We compare to the best-fit M_* -SFR relation from Sanders et al. (2018) for a representative sample of $z \sim 2.3$ star-forming galaxies with $\log(M_*/M_\odot) = 9.0 - 11.0$ from MOSDEF, with SFRs derived from dust-corrected $H\alpha$ luminosities (dashed blue line):

$$\log(\text{SFR}/M_\odot \text{ yr}^{-1}) = 0.67 \times \log(M_*/M_\odot) - 5.33 \quad (8)$$

Given the redshift range of the $z > 1$ auroral line sample

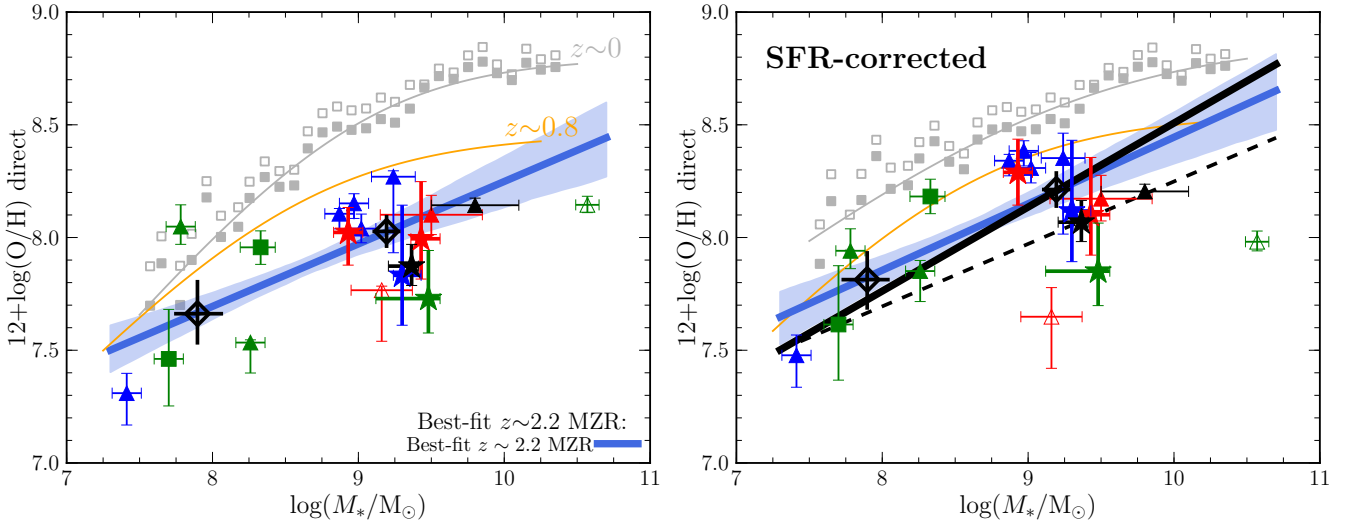


Figure 4. LEFT: The stellar mass—gas-phase metallicity relation (MZR) at $z \sim 2.2$ using electron temperature measurements. Points with error bars are as in Figure 3. Hollow triangles denote the two galaxies identified as probable mergers (C12b, C12c), which are excluded when fitting the MZR. The solid blue line shows the best-fit linear relation to individual $z > 1$ galaxies (equation 7), with the 1σ confidence interval given by the blue-shaded region. The mean values in two bins in stellar mass divided at $\log(M_*/M_\odot) = 8.5$ are displayed as black open diamonds. The orange line shows the direct-method MZR at $z \sim 0.8$ from Ly et al. (2016). The $z \sim 0$ M_* -binned stacks of Andrews & Martini (2013) are presented as gray squares, where the filled squares have been corrected for DIG emission and flux-weighting effects using the models of Sanders et al. (2017). The best-fit $z \sim 0$ MZR is given by the gray line. RIGHT: The MZR based on direct-method metallicities, where O/H has been corrected for biases in SFR of each sample relative to the mean M_* -SFR relation at each redshift. Corrected O/H values should represent typical galaxies on the M_* -SFR relation at each redshift. The blue line in the right panel shows the best-fit $z \sim 2.2$ MZR to the SFR-corrected sample (equation 10). The uncorrected best-fit MZR from the left panel is displayed as a black dashed line, lying ~ 0.2 dex below the SFR-corrected MZR. The solid black line displays the best-fit $z \sim 2.2$ MZR after additionally correcting for the low-redshift bias of the low-mass bin (equation 11), and is the most robust representation of the MZR at $z \sim 2.2$ presented here.

($1.4 < z < 3.7$) and the evolution of the M_* -SFR relation with redshift, we fix the slope of the M_* -SFR relation to that of equation 8 and shift the normalization to estimate mean M_* -SFR relations at $z \sim 1.5$ (green dashed line) and $z \sim 3.4$ (red dashed line) with offsets calculated according to the best-fit SFR(M_* , z) relation of Speagle et al. (2014) (-0.21 dex for $z \sim 1.5$ and $+0.15$ dex for $z \sim 3.4$). We find that the $z > 1$ galaxies have significantly higher SFR at fixed M_* than is typical for galaxies at the same redshifts, with only one galaxy in the $z > 1$ MZR sample falling below its corresponding M_* -SFR relation.

We plot the median M_* and SFR values of the Andrews & Martini (2013) stacks in Figure 5 (gray squares), and find that their SDSS sample is significantly biased in SFR at $\log(M_*/M_\odot) < 8.75$. We fit a linear relation to the Andrews & Martini (2013) stacks above $\log(M_*/M_\odot) = 9.0$ to determine the mean $z \sim 0$ M_* -SFR relation (gray dashed line), recovering a slope that is nearly identical to that of the $z \sim 2.3$ relation from Sanders et al. (2018). The $z \sim 0.8$ MZR sample has been shown to be biased in SFR ~ 0.3 dex higher than representative samples at the same redshift (Ly et al. 2016).

If the dependence of O/H on SFR at fixed M_* is known, then SFR biases can be corrected for to obtain representative MZRs for each sample. The strength of the SFR dependence of the FMR can be quantified by the slope of the anticorrelation between residuals around the M_* -SFR relation ($\Delta\log(\text{SFR})$) and residuals around the MZR ($\Delta\log(\text{O}/\text{H})$) (e.g., Salim et al. 2015; Davé et al. 2017; Kashino et al. 2017;

Sanders et al. 2018). Using the Andrews & Martini (2013) $z \sim 0$ SDSS stacks binned in M_* +SFR and corrected for DIG (Sanders et al. 2017), we fit $\Delta\log(\text{O}/\text{H})$ vs. $\Delta\log(\text{SFR})$ using direct-method metallicities (gray points and black dashed line in Figure 6) and find that

$$\Delta\log(\text{O}/\text{H}) \propto -0.29 \times \Delta\log(\text{SFR}/M_\odot \text{ yr}^{-1}) \quad (9)$$

This dependence of O/H on SFR is approximately twice as strong as is seen when using strong-line metallicity calibrations (Salim et al. 2014; Sanders et al. 2018), but the FMR is known to have a stronger SFR dependence when direct-method metallicities are employed (Andrews & Martini 2013; Sanders et al. 2017). This best-fit relation can be used to correct the metallicity of samples in the left panel of Figure 4 for SFR biases, assuming the SFR dependence of direct-method O/H at fixed M_* does not change with redshift.⁴

We correct the oxygen abundances of the $z \sim 0$ and $z > 1$

⁴ At fixed M_* , $z \sim 0$ samples display a non-linear SFR dependence of O/H at high masses ($\log(M_*/M_\odot) \gtrsim 10.0$) and low SFRs (i.e., below the mean $z \sim 0$ SFR- M_* relation) (e.g., Mannucci et al. 2010; Yates et al. 2012; Cresci et al. 2019). All of the galaxies to which we apply eq. 9 have $\log(M_*/M_\odot) < 10.0$ and lie significantly above the local SFR- M_* relation, a regime in which both local and high-redshift studies have demonstrated a linear dependence of O/H on SFR at fixed M_* (Mannucci et al. 2010; Sanders et al. 2018; Cresci et al. 2019). The linear approximation in eq. 9 is thus appropriate to carry out SFR bias correction on these samples.

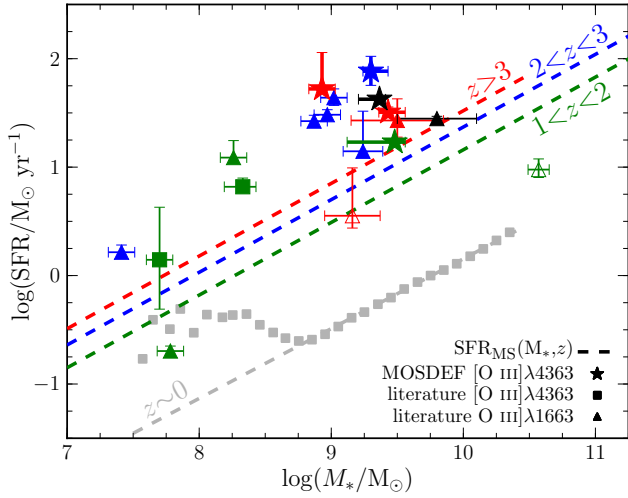


Figure 5. SFR vs. M_* for the $z > 1$ auroral-line sample. Points with error bars are as in Figure 3. The dashed blue line shows the best-fit SFR- M_* relation at $z \sim 2.3$ from Sanders et al. (2018). The green and red dashed lines show the SFR- M_* relation at $z \sim 1.5$ and $z \sim 3.4$, respectively, constructed by shifting the normalization of the $z \sim 2.3$ relation by $\Delta \log(\text{SFR})$ as given by the model of Speagle et al. (2014). The majority of the $z > 1$ sample is significantly elevated above the mean M_* -SFR relation in each redshift bin. The gray dashed line shows the best-fit SFR- M_* relation to the Andrews & Martini (2013) M_* -binned stacks at $\log(M_*/M_\odot) > 9.0$. The best-fit $z \sim 0$ relation displays a nearly identical slope to the $z \sim 2.3$ relation despite being fit independently. The Andrews & Martini (2013) stacks below $\log(M_*/M_\odot) = 8.75$ display a large bias in SFR at fixed M_* .

MZR samples for SFR biases according to equation 9 and $\Delta \log(\text{SFR})$ relative to the M_* -SFR relation at each redshift (Figure 5). For the $z \sim 0.8$ MZR of Ly et al. (2016), we shift their best-fit MZR adopting an average $\Delta \log(\text{SFR}) = 0.3$ dex. The resulting SFR-corrected MZR at $z \sim 0-2.2$ is presented in the right panel of Figure 4. Correcting for the SFR biases present in each sample shifts the relations in the left panel of Figure 4 such that they are now representative of galaxy populations falling on the mean M_* -SFR relation at each redshift. We fit the SFR-corrected $z \sim 2.2$ MZR and obtain

$$12 + \log(\text{O}/\text{H}) = (0.295 \pm 0.080) \times \log(M_*/M_\odot) + (5.49 \pm 0.68) \quad (10)$$

with a covariance of $\rho = 0.998$ between the slope and intercept. The SFR-corrected $z \sim 2.2$ MZR fit is ~ 0.2 dex higher in metallicity than the uncorrected fit (equation 7), but has a similar slope. The mean SFR-corrected metallicity of the low- and high-mass bin is $12 + \log(\text{O}/\text{H})_{\text{med}} = 7.81 \pm 0.13$ and 8.21 ± 0.08 , respectively.

We test whether the SFR dependence described by equation 9 was appropriate to apply to the $z > 1$ sample by plotting the high-redshift galaxies in Figure 6, where $\Delta \log(\text{SFR})$ is determined relative to the M_* -SFR relation matched in redshift for each galaxy (Fig. 5) and $\Delta \log(\text{O}/\text{H})$ is determined using the uncorrected metallicities (i.e., those displayed in Table 2) relative to the SFR-corrected MZR of equation 10. We find a weak anticorrelation between $\Delta \log(\text{O}/\text{H})$ and $\Delta \log(\text{SFR})$, with a significance of $\approx 2\sigma$. We

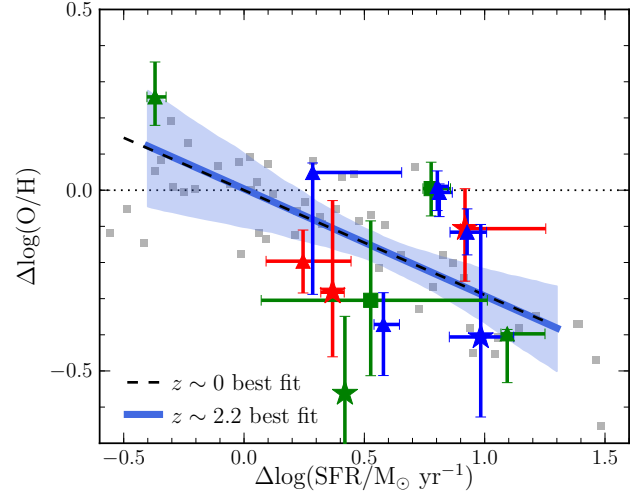


Figure 6. Deviation plot comparing the residuals around the MZR ($\Delta \log(\text{O}/\text{H})$) to residuals around the mean SFR- M_* relation ($\Delta \log(\text{SFR})$). The best-fit MZR after SFR correction (equation 10) and the uncorrected O/H values are used to calculate the O/H residuals at $z > 1$. Colored points are as in Figure 3. The gray squares show the M_* -SFR binned $z \sim 0$ stacks of Andrews & Martini (2013), with a best-fit given by the dashed black line (equation 9). A weak anticorrelation is present at $z > 1$, suggesting a dependence of direct-method O/H on SFR at fixed M_* quantitatively similar to the $z \sim 0$ direct-method FMR (blue line, with 1σ uncertainty given by the light blue shaded region).

fit a linear relation to the $z > 1$ sample, finding a slope of -0.30 ± 0.16 , remarkably consistent with the $z \sim 0$ slope. This relation is tentative evidence for the existence of a M_* -SFR-O/H relation at $z \sim 2.2$ based purely on direct-method metallicities, although the current sample has only one galaxy falling below the mean M_* -SFR relation (i.e., with $\Delta \log(\text{SFR}) < 0$). We conclude that equation 9 and our method of correcting for SFR biases are applicable at high redshifts.

The scatter of the $z > 1$ sample around the best-fit MZR is slightly smaller after correcting for SFR. Indeed, the most significant outliers in the left panel of Figure 4 were also outliers in SFR compared to the rest of the sample, and are no longer outliers in the right panel. The $z > 1$ mergers (open triangles) are not strong outliers in the left panel, but fall well below the best-fit $z \sim 2.2$ MZR in the right panel, suggesting that they do not have the same relation between M_* , SFR, and O/H as the rest of the sample.

The best-fit $z \sim 2.2$ MZR in equation 10 has a slightly shallower slope than is typically seen in strong-line metallicity studies (e.g., Erb et al. 2006; Cullen et al. 2014; Maier et al. 2014; Steidel et al. 2014; Sanders et al. 2015, 2018). This flattening is due to the redshifts of the galaxies in each mass bin. The median redshift of galaxies in the high-mass bin is 2.31, while the median redshift in the low-mass bin is 1.83. It is thus expected that the high-mass bin will have evolved farther from the $z \sim 0$ MZR than the low-mass bin, artificially flattening the observed MZR of our $z > 1$ auroral-line sample. Consequently, the true $z \sim 2.2$ MZR is steeper than equation 10.

In the high-mass bin, we find that O/H at

$\log(M_*/M_\odot) \approx 9.2$ decreases by 0.2 dex from $z \sim 0$ to $z \sim 0.8$ and by 0.4 ± 0.1 dex from $z \sim 0$ to $z \sim 2.3$. At $\log(M_*/M_\odot) \approx 7.9$, O/H is lower by 0.2 dex at $z \sim 0.8$ and 0.35 ± 0.15 dex at $z \sim 1.8$ compared to $z \sim 0$. These values suggest a roughly linear evolution in $\log(\text{O}/\text{H})$ at fixed M_* with redshift of $d\log(\text{O}/\text{H})/dz \approx 0.2$ that does not display a strong dependence on M_* below $\sim 10^{9.5} M_\odot$ out to $z \sim 2.3$. Accordingly, we find that the low-mass bin would have 0.10 dex lower O/H when “evolved” from $z = 1.83$ to $z = 2.31$. We alter the slope and intercept of equation 10 such that the line has the same O/H at $\log(M_*/M_\odot) = 9.19$ but yields a value 0.10 dex lower at $\log(M_*/M_\odot) = 7.90$, obtaining:

$$12 + \log(\text{O}/\text{H}) = 0.373 \times \log(M_*/M_\odot) + 4.78 \quad (11)$$

where the uncertainties in equation 10 can be applied to the slope and intercept here.

After correcting for SFR and sample redshift biases, we find that O/H at $\log(M_*/M_\odot) = 7.5-9.5$ decreases by 0.2 dex at fixed M_* from $z \sim 0$ to $z \sim 0.8$, and by 0.4 ± 0.1 dex at fixed M_* from $z \sim 0$ to $z \sim 2.3$. This MZR evolution is consistent with what is found using strong-line methods at $z \sim 0.5 - 1$ (Savaglio et al. 2005; Maiolino et al. 2008; Zahid et al. 2014a; Troncoso et al. 2014) and consistent with strong-line studies at $z \sim 2$ that find $\sim 0.25 - 0.4$ dex evolution in O/H at fixed M_* (e.g., Erb et al. 2006; Maier et al. 2014; Steidel et al. 2014; Sanders et al. 2015, 2018).

Our final $z \sim 2.3$ slope of 0.373 ± 0.080 is consistent within the uncertainties with previous results at $z \sim 2$ based on a number of strong-line metallicity indicators (e.g., Erb et al. 2006; Henry et al. 2013; Maier et al. 2014; Sanders et al. 2015, 2018). Sanders et al. (2018) found a $z \sim 2.3$ MZR slope of 0.26, 0.30, 0.34, and 0.30 when using O32, O3N2, N2, and N2O2 strong-line calibrations, respectively. Steidel et al. (2014) find a shallow $z \sim 2.3$ MZR slope of 0.20 based on the N2 and O3N2 indicators, in contrast to other strong-line works. Our direct-method results disagree with such a shallow MZR slope at the 2.2σ level, favoring a steeper slope but not statistically ruling out a shallower slope. A larger $z > 1$ auroral-line sample is needed to tightly constrain the high-redshift MZR slope via the direct-method.

3.2.2 The direct-method fundamental metallicity relation from $z \sim 0 - 2.2$

The $z \sim 0$ FMR has been claimed to be redshift independent, such that galaxies at $z = 0 - 2.5$ all follow the same M_* -SFR-O/H relation, with high-redshift galaxies having lower metallicities in proportion to their higher SFRs at fixed M_* (e.g., Mannucci et al. 2010; Cresci et al. 2019). In Sanders et al. (2018), we showed that $z \sim 2.3$ galaxies were offset ~ 0.1 dex below the $z \sim 0$ FMR using a direct comparison of strong-line metallicities at fixed M_* and SFR. Whether the FMR is in fact redshift invariant remains an open question given the uncertainties associated with strong-line metallicities at high redshifts. It is thus of interest to test the universality of the FMR using direct-method metallicities. We cannot perform a direct comparison following Sanders et al. (2018) because there are not enough local analogs with [O III] $\lambda 4363$ detections matched in M_* and SFR to our $z > 1$ sample. In lieu of a direct comparison, we rely on parameterized forms of the FMR.

Mannucci et al. (2010) constructed a planar parameterization of the $z \sim 0$ M_* -SFR-O/H relation that is described by O/H as a function of $\mu_\alpha = \log(M_*) - \alpha \times \log(\text{SFR})$. Using strong-line metallicities, Mannucci et al. found that $\alpha = 0.32$ minimized the scatter in O/H at fixed μ_α . We plot $12 + \log(\text{O}/\text{H})$ vs. $\mu_{0.32}$ for the $z > 1$ and low-redshift MZR samples in the top panel of Figure 7. There are offsets between the $z \sim 0$, $z \sim 0.8$, and $z \sim 2.2$ samples, such that galaxies at higher redshift fall lower in O/H at fixed $\mu_{0.32}$. However, the direct-method FMR has been found to have stronger SFR dependence than when using strong-line metallicities. Andrews & Martini (2013) find a value of $\alpha = 0.66$ minimizes the FMR scatter using direct-method metallicity, while Sanders et al. (2017) find a best-fit value of $\alpha = 0.63$ after correcting for DIG contamination. We adopt $\alpha = 0.63$, and present the resulting FMR projection in the bottom panel of Figure 7. The $z \sim 2.2$ sample is consistent with both the $z \sim 0$ and $z \sim 0.8$ samples to within ~ 0.1 dex at fixed $\mu_{0.63}$. This comparison is the first test of the universality of the FMR at high redshifts using temperature-based metallicities. This result suggests that, on average, O/H does not vary by more than ~ 0.1 dex at fixed M_* and SFR from $z = 0$ to $z \sim 2.2$, in agreement with results using strong-line metallicities (Sanders et al. 2018; Cresci et al. 2019).

3.2.3 Systematic effects on O/H, SFR, and M_* comparison

A concern when comparing metallicity scaling relations across multiple galaxy samples is whether the metallicities, M_* , and SFRs of each sample can be fairly compared. The metallicities of all samples in this work have been determined via the direct-method based on either [O III] $\lambda 4363$ or O III] $\lambda 1663$ and can be directly compared in an unbiased manner, even when the samples span a large range in redshift. The SFRs of all samples have been determined using reddening-corrected Balmer emission lines and calibrations within $\approx 10\%$ of one another in normalization, such that the comparison of SFRs between our low- and high-redshift samples is robust. Stellar mass determinations require a number of assumptions regarding the stellar population templates, attenuation curve, IMF, and star-formation history. We have shifted all stellar masses and SFRs to a Chabrier (2003) IMF.

Even when utilizing the same IMF, differences in SED-fitting assumptions can result in systematic uncertainties of ~ 0.3 dex in M_* (e.g., Reddy et al. 2012). Details of the SED fitting were not included in all of the references from which we obtained M_* for the $z > 1$ aurora-line sample. However, we have confirmed that over half of the $z > 1$ sample was fit with Bruzual & Charlot (2003) stellar population synthesis models, a constant or declining star-formation history, a Calzetti et al. (2000) attenuation curve, and metallicities ranging from $0.2 - 1.0 Z_\odot$. Based on changing the SED-fitting assumptions for the MOSDEF $z \sim 2$ star-forming galaxy sample, stellar masses under the range of assumptions described above typically vary by $\sim 0.1 - 0.2$ dex compared to M_* derived under our fiducial assumptions (Sec. 2.2). Furthermore, this range of assumptions is similar to those used in M_* determination of the $z \sim 0$ and $z \sim 0.8$ samples (Brinchmann et al. 2004; Andrews & Martini 2013; Ly et al. 2016). Given our best-fit $z \sim 2$ MZR slope of ≈ 0.37 ,

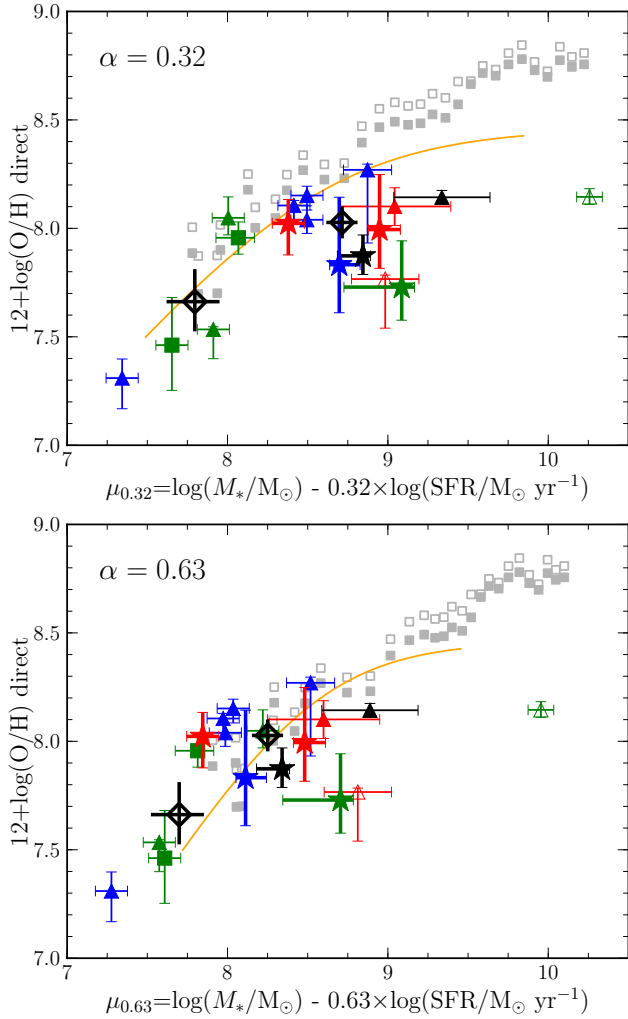


Figure 7. The Mannucci et al. (2010) planar projection of the FMR. Points and lines are as in Figure 4. The $z > 1$ sample is significantly offset from the $z \sim 0$ FMR when using $\alpha = 0.32$ (top panel), the best-fit value from Mannucci et al. (2010) based on strong-line metallicities. When using the best-fit $z \sim 0$ value, $\alpha = 0.63$ (bottom panel), from Sanders et al. (2017) based on direct-method metallicities, the $z > 1$ galaxies fall within ~ 0.1 dex of the $z \sim 0$ FMR on average.

a systematic offset of 0.2 dex in M_* between the samples at each redshift would introduce a systematic bias of ~ 0.07 dex in the inferred O/H evolution, smaller than the typical uncertainties on O/H in the $z > 1$ sample. We conclude that the metallicity evolution results presented herein are not significantly affected by systematic biases associated with the determination of O/H, SFR, or M_* for each sample.

An additional concern is whether sample selection effects are present beyond SFR biases (which we have corrected for). This is a particular concern at high redshift where the sample size is small and selection requires the detection of extraordinarily weak emission lines. Even at fixed M_* and SFR, the auroral-line detection criterion will select galaxies with higher excitation and lower O/H than average such that we are incomplete in metallicity sampling. Furthermore, since the detection cut is made on a weak emis-

sion line, an additional bias will be present where galaxies are preferentially detected when positive noise fluctuations occur, leading to an overestimate of the auroral-line fluxes among low-S/N detections. Both of these effects bias the mean metallicity of our sample low. Given that 10/18 of the $z > 1$ auroral-line sample have $S/N_{\text{aur}} > 5$ (Tab. 2) and a positive noise fluctuation is not expected to be present for all low-S/N detections, we expect that the latter bias has a minimal effect on the sample average metallicities from which we draw conclusions. The former bias is likely present to some extent.

We estimate the magnitude of the excitation bias by selecting a sample of MOSDEF star-forming galaxies at $z \sim 2.3$ matched in M_* and SFR to a subset of the $z > 1$ auroral-line sample. We can only make such a match in the narrow range of overlap at $9.0 \leq \log(M_*/M_\odot) \leq 9.5$ and $\log(\text{SFR}/M_\odot \text{ yr}^{-1}) \geq 1.1$, where there are 5 auroral-line sources and 15 MOSDEF $z \sim 2.3$ galaxies. The MOSDEF galaxies should be representative at this redshift, M_* , and SFR since they are selected according to a rest-optical magnitude limit. The two subsamples are closely matched in M_* and SFR, with mean values of $\langle \log(M_*/M_\odot) \rangle = [9.33 \pm 0.08, 9.37 \pm 0.02]$ and $\langle \log(\text{SFR}/M_\odot \text{ yr}^{-1}) \rangle = [1.47 \pm 0.05, 1.34 \pm 0.04]$ for the auroral-line and MOSDEF targets, respectively. The auroral-line subsample has $\langle \log(\text{O}32) \rangle = 0.54 \pm 0.08$ and $\langle \log(\text{O}3) \rangle = 0.80 \pm 0.03$, systematically higher than the M_* - and SFR-matched MOSDEF subsample with $\langle \log(\text{O}32) \rangle = 0.42 \pm 0.02$ and $\langle \log(\text{O}3) \rangle = 0.70 \pm 0.02$. Based on the BKD18 high-redshift analog O32 calibration, the O32 difference of 0.12 ± 0.08 dex corresponds to a bias in O/H of -0.07 ± 0.05 dex for the auroral-line subsample. Part of this O/H difference can be accounted to the slightly higher SFR of the auroral-line subsample (see eq. 9). We conclude that the high-excitation selection biases our sample-averaged metallicities by < 0.1 dex and thus does not significantly affect our conclusions regarding the evolution of metallicity calibrations, the MZR, and the FMR.

4 PHOTOIONIZATION MODELING: STELLAR METALLICITY & IONIZATION PARAMETER

Photoionization models of H II regions utilizing state-of-the-art stellar models are powerful tools for extracting information about the ionization state and chemical abundances of ionized gas from observed nebular emission-line strengths (e.g., Kewley & Dopita 2002; Steidel et al. 2014; Dopita et al. 2016; Strom et al. 2018; Kashino & Inoue 2019). However, degeneracies between the ionization state and nebular metallicity are significant when only the strong optical emission-line ratios are available, especially when just a subset of the strong optical nebular emission lines are detected, as is the case for nearly all high-redshift galaxies.

Recent observational and theoretical work has suggested that the Fe/H of massive stars may be deficient relative to the O/H of the ionized gas on a solar abundance scale in $z > 1$ galaxies (i.e., $\text{O}/\text{Fe} > \text{O}/\text{Fe}_\odot$; Steidel et al. 2016; Matthee & Schaye 2018; Strom et al. 2018; Cullen et al. 2019). This O/Fe enhancement is thought to be caused by the rapid formation timescales ($\lesssim 1$ Gyr; e.g., Reddy et al. 2012, 2018) of high-redshift galaxies, in which chemical en-

richment is dominated by Type II SNe that yield super-solar O/Fe ratios (Nomoto et al. 2006; Kobayashi et al. 2006). This enhancement in O/Fe relative to a solar abundance pattern is brought about because the majority of Fe is produced in Type Ia SNe, most of which occur on timescales ~ 1 Gyr after a star-formation event, while O is produced promptly in core-collapse Type II SNe on timescales of $\lesssim 10$ Myr, the lifetimes of massive stars.

Using the unique direct-method nebular metallicity constraints of our $z > 1$ auroral-line sample, we fix the input nebular metallicity (i.e., O/H) in grids of photoionization models, allowing us to unambiguously constraint the stellar metallicity (i.e., Fe/H) and the ionization parameter, U , for this set of high-redshift star-forming galaxies.

4.1 Description of the photoionization models and fitting procedure

We utilize the code Cloudy (v17.01; Ferland et al. 2017) to produce a grid of photoionization models for use in constraining the ionization parameter (U) and stellar ionizing spectral shape for the $z > 1$ auroral-line sample. We construct simple H II region models assuming a plane-parallel geometry ionized by a single star cluster, where the calculation is stopped at the edge of the fully-ionized H zone. The input parameters of the models are the ionization parameter U , electron density n_e , nebular metallicity $Z_{\text{neb}}^{\text{in}}$, and stellar metallicity Z_* . In practice, we fix n_e to a constant value and vary U , $Z_{\text{neb}}^{\text{in}}$, and Z_* for the calculation of the model grids, as described below. Using this set of model grids, we fix $Z_{\text{neb}}^{\text{in}}$ to a value matched to the direct-method metallicity for each object and unambiguously fit for U and Z_* .

4.1.1 Photoionization model grids

The intensity of the radiation field is set by the dimensionless ionization parameter, $U = n_{\text{Ly}\alpha}/n_{\text{H}}$, where $n_{\text{Ly}\alpha}$ is the volume density of hydrogen-ionizing photons and n_{H} is the hydrogen gas volume density, which can be approximated by the electron density n_e . We vary $\log(U)$ from -1.0 to -4.0 in 0.1 dex steps. We assume a constant density of $n_e = 250 \text{ cm}^{-3}$, a typical value for $z \sim 2$ star-forming galaxies (e.g., Sanders et al. 2016a; Steidel et al. 2016; Strom et al. 2017).

The gas-phase elemental abundances are assumed to follow a solar abundance pattern, such that the abundances of each element is set by the oxygen abundance, O/H. To avoid confusion with the nebular metallicity measured via the direct-method from observations (Z_{neb}), we refer to the model input nebular metallicity as $Z_{\text{neb}}^{\text{in}}$. While the abundances of elements with secondary production channels (C, N) depend on Z_{neb} , we do not utilize any lines of these elements in the fitting procedure described below, and thus simply leave them fixed at a solar scale for convenience. This assumption has a negligible effect on the line ratios of O, Ne, and H across the range of parameters explored here. We adopt a range of values for the nebular metallicity: $Z_{\text{neb}}^{\text{in}}/Z_{\odot} = [0.05, 0.1, 0.2, 0.3, 0.4, 0.5, 0.6, 0.7, 0.8, 0.9, 1.0, 1.25, 1.5]$ ($7.4 \leq 12 + \log(\text{O}/\text{H})^{\text{in}} \leq 8.9$).

Following Steidel et al. (2016) and Strom et al. (2018), the stellar metallicity, Z_* , is allowed to vary freely from

$Z_{\text{neb}}^{\text{in}}$. Only the hydrogen-ionizing photons ($h\nu > 13.6 \text{ eV}$; $\lambda < 912 \text{ \AA}$) produced by the stellar ionizing source affect the emission-line production of the ionized nebula, as these photons are responsible for liberating and heating the free electron population. The spectrum of massive stars at $\lambda < 912 \text{ \AA}$ is primarily governed by the opacity of the photosphere from line-blanketing of iron-peak elements. This opacity, driven by Fe/H, strongly affects the evolution of massive stars. Larger opacity due to higher Fe/H results in stronger stellar winds, driving larger mass loss rates and decreasing rotation. Accordingly, stars with lower Fe/H produce a larger number of ionizing photons, have a harder spectral shape due to a hotter effective temperature, and can potentially continue producing copious amounts of ionizing photons for a longer time period due to effects such as quasi-homogeneous evolution (Eldridge et al. 2011; Eldridge & Stanway 2012). We assume that Z_* , which sets the shape of the ionizing stellar spectrum, effectively traces Fe/H. Thus, decoupling Z_* and $Z_{\text{neb}}^{\text{in}}$ allows us to investigate non-solar O/Fe ratios and vary the hardness of the ionizing spectrum at fixed O/H.

We adopt the ‘‘Binary Population and Spectral Synthesis’’ v2.2.1 models (BPASS; Stanway & Eldridge 2018), which include the effects of binarity on the evolution of massive stars. We use the binary BPASS models with a high-mass IMF slope of -2.35 and a high-mass cutoff of $100 M_{\odot}$ as our fiducial set of ionizing spectra. We vary the BPASS stellar metallicities over the range $Z_* = 10^{-5} - 0.020$ ($0.0007 - 1.4 Z_{\odot}$ based on $Z_{\odot} = 0.014$ from Asplund et al. 2009). For comparison, we also utilize single-star models from Starburst99 (SB99; Leitherer et al. 2014) with the same IMF slope and cutoff, with a metallicity range of $0.001 - 0.040$ ($0.07 - 2.8 Z_{\odot}$). The input stellar populations are assumed to have continuous star formation, with an age of 100 Myr. The ionizing spectra of both BPASS and SB99 models reach equilibrium after 10 Myr of continuous star formation, so the nebular emission-line predictions are appropriate for systems with stellar populations older than 10 Myr.

The photoionization models are stopped at the edge of the H II zone, and thus do not include any DIG component. We have ensured that the empirical data sets we model can be well represented by H II-only emission. The $z \sim 0$ composites of AM13 have been corrected for DIG contamination following Sanders et al. (2017). For star-forming galaxies at $z > 1$, and in particular the extremely high-sSFR $z > 1$ auroral-line sample, DIG emission is expected to be negligible due to their high SFRs and compact sizes (Shapley et al. 2019). This expectation assumes no redshift evolution of the relation between SFR surface density and the fractional importance of DIG to line emission, empirically established at $z = 0$ (Oey et al. 2007).

No dust grains or depletion of gas-phase elements onto grains are included in the photoionization models. We thus assume that the effects of dust depletion on the derived gas-phase O/H for the $z > 1$ auroral-line sample and the $z \sim 0$ AM13 stacks is negligible. Steidel et al. (2016) derived an O depletion factor of 0.09 dex for the KBSS-LM1 composite that has $12 + \log(\text{O}/\text{H}) = 8.14$ and $E(\text{B}-\text{V})_{\text{gas}} = 0.24$. The bulk of the $z > 1$ sample has lower metallicity and less dust reddening than KBSS-LM1 ($(12 + \log(\text{O}/\text{H})) \approx 8.00$ and $\langle E(\text{B}-\text{V})_{\text{gas}} \rangle \approx 0.10$). At such low metallicities, O depletion has been found to be negligible in local star-forming

galaxy samples, and O depletion is not observed to much exceed 0.1 dex even at near-solar metallicities (Izotov et al. 2006). We thus conclude that our assumption of no O depletion is valid for the $z > 1$ auroral-line sample and $z \sim 0$ galaxies at comparably low metallicities, but that depletion may bias metallicities low by up to 0.1 dex for $z \sim 0$ galaxies at higher metallicities. Adding a 0.1 dex correction to the derived temperature-based metallicities does not produce qualitatively different results from the photoionization model fitting.

4.1.2 U and Z_* fitting procedure

Utilizing the model grids described above, we produce constraints on the ionization state of the $z > 1$ auroral-line sample by fixing $Z_{\text{neb}}^{\text{in}}$ to a value appropriate for each galaxy. Thus, a critical step to utilizing these photoionization models to constrain U and Z_* is matching the measured direct-method Z_{neb} to $Z_{\text{neb}}^{\text{in}}$ of a particular set of models. The simplest assumption is $Z_{\text{neb}}^{\text{in}} = Z_{\text{neb}}$, that is, the direct-method O/H represents the “true” gas-phase metallicity in an unbiased manner. In the left column of Figure 8, we compare the measured O3 and O2 line ratios of $z > 1$ galaxies to model grids directly matched in metallicity. We find that both BPASS and SB99 grids significantly underpredict O3 and O2 of the majority of $z > 1$ galaxies when $Z_{\text{neb}}^{\text{in}} = Z_{\text{neb}}$, even at the lowest Z_* (hardest ionizing spectrum).

There is evidence that the temperature-based metallicities are systematically biased and thus do not represent the “true” gas-phase metallicity. There is a longstanding disagreement between temperature-based metallicities from collisionally-excited auroral lines (direct method) and metallicities determined using O recombination lines (RL method), known as the abundance discrepancy factor (ADF) problem (e.g., Peimbert 1967; Esteban et al. 2014). Direct-method metallicities are systematically lower than RL-method metallicities measured for the same targets. The value of the ADF appears to be roughly constant as a function of metallicity, with the direct method yielding ≈ 0.24 dex lower metallicities than the RL method on average (e.g., Esteban et al. 2014; Blanc et al. 2015). The ADF has been proposed to be caused by fluctuations in the temperature field of the ionized nebula, such that hotter regions dominate the auroral-line emission and bias temperature measurements high and, consequently, direct-method O/H measurements low (Peimbert 1967; García-Rojas & Esteban 2007). Alternatively, a chemically inhomogeneous medium with metal-rich small-scale overdensities provides an explanation of the ADF in which RL metallicities are biased high (Tsamis & Péquignot 2005; Stasińska et al. 2007). Both of these phenomena could be present in H II regions. There is an ongoing debate whether the direct-method or RL metallicities represent the true gas-phase abundance scale (Maiolino & Mannucci 2019). Attempts have been made to solve this problem by comparing the stellar oxygen abundance of young A and B supergiants to the RL and direct method metallicities of the H II regions they occupy, with conflicting results. The stellar O/H agrees with the RL method in some H II regions and the direct method in oth-

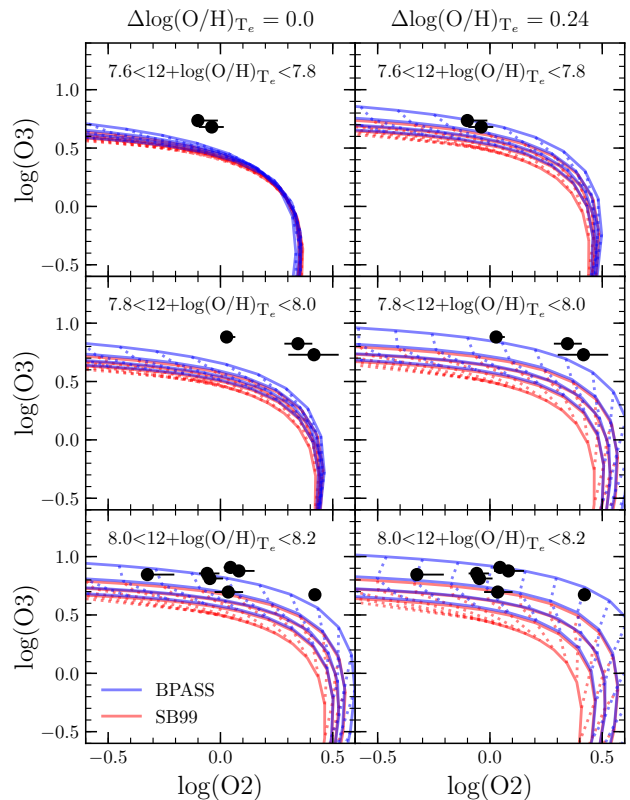


Figure 8. Comparison of photoionization model grids to observed line-ratios (O3 vs. O2) at $z > 1$, in three bins of metallicity. Grids are shown from the BPASS (blue) and SB99 (red) models at fixed nebular metallicity, with varying stellar metallicity and ionization parameter. Lines of constant stellar metallicity are solid, while lines of constant ionization parameter are dotted. In the left column, the input nebular metallicity to the models is assumed to be the same as the direct-method metallicity of the observed galaxies ($\Delta \log(\text{O}/\text{H})_{T_e} = 0.0$), such that the input nebular metallicity for the top-, middle-, and bottom-left panels is $12 + \log(\text{O}/\text{H}) = 7.7, 7.9,$ and $8.1,$ respectively. In the right column, the input nebular metallicity to the models is instead assumed to be larger than the observed direct-method metallicity by 0.24 dex ($\Delta \log(\text{O}/\text{H})_{T_e} = 0.24$), the mean difference between electron-temperature and recombination line metallicities of $z \sim 0$ H II regions. The input nebular metallicity of the models in the top-, middle-, and bottom-right panels is thus $12 + \log(\text{O}/\text{H}) = 7.94, 8.14,$ and $8.34,$ respectively. The SB99 models fail to produce large enough O3 and O2 values to match observations in all panels. The BPASS models fail to match observations when $\Delta \log(\text{O}/\text{H})_{T_e} = 0.0$. The ability of the BPASS models to reproduce the range of O3 and O2 values observed at fixed O/H significantly improved when assuming $\Delta \log(\text{O}/\text{H})_{T_e} = 0.24$. We adopt this as a fiducial assumption when matching models to observations.

ers (Bresolin et al. 2016; Toribio San Cipriano et al. 2016, 2017). It is not clear which method yields the true Z_{neb} .⁵

⁵ While temperature fluctuations may bias the normalization of direct-method metallicities by $\sim 0.2 - 0.3$ dex, relative differences in direct-method metallicity are much more robust. The direct-method metallicity results on strong-line calibrations and scaling relations presented in Sec. 3 would only be biased if the magni-

Regardless of the remaining uncertainties regarding direct vs. RL methods, we have found that the models cannot reproduce the observations when $Z_{\text{neb}}^{\text{in}} = Z_{\text{neb}}$, where the latter is determined using the direct method (Fig. 8, left column). In the right column of Figure 8, we show the resulting model grids when we apply the typical ADF of 0.24 dex between the RL and direct methods to our measured $z > 1$ direct-method O/H values ($\log(Z_{\text{neb}}^{\text{in}}) = \log(Z_{\text{neb}}) + 0.24$). The BPASS grids (blue) now span the range of measured O3 and O2 of the majority of the $z > 1$ sample. Steidel et al. (2016) similarly found that applying a 0.24 dex ADF to the direct-method O/H of their stack of $z \sim 2.3$ star-forming galaxies was necessary for model grids to match measured line ratios. We proceed under the assumption that $\log(Z_{\text{neb}}^{\text{in}}) = \log(Z_{\text{neb}}) + 0.24$. We note that the SB99 grids fail to overlap the $z > 1$ galaxies even under this assumption because they do not produce hard enough ionizing spectra even at the lowest available metallicity, $Z_* = 0.07 Z_{\odot}$. Therefore, we conclude that SB99 ionizing spectra cannot reproduce the emission-line properties of our $z > 1$ sample and only show results using the BPASS binary models for the remainder of the analysis.

We fit for the ionization parameter and stellar metallicity of each galaxy using the following procedure. We first interpolate the photoionization model grids in nebular metallicity to construct a grid of strong-line ratios as a function of U and Z_* at fixed $Z_{\text{neb}}^{\text{in}}$ according to $\log(Z_{\text{neb}}^{\text{in}}) = \log(Z_{\text{neb}}) + 0.24$, where Z_{neb} is the measured direct-method O/H given in Table 2. We fit for U and Z_* by performing a χ^2 minimization using the measured reddening-corrected strong-line ratios simultaneously. For the fitting procedure, we do not include ratios involving lines of N because of uncertainty in the N/O vs. O/H relation at high redshifts (Masters et al. 2014; Steidel et al. 2014; Sanders et al. 2015, 2016a; Shapley et al. 2015; Strom et al. 2018), and also exclude line ratios involving S because it has an ionization potential lower than that of H and may be emitted in partially-ionized regions that our photoionization models do not include. We use line ratios of collisionally-excited metal lines relative to H β only. Thus, the line ratios used in the fitting process include [O III] λ 5007/H β (O3), [O II] λ 3726/H β (O2), and [Ne III] λ 3869/H β (Ne3). Given the tight relation between O3 and Ne3 at sub-solar metallicities (Levesque & Richardson 2014), a galaxy must have at minimum detections of O3 and O2 to fit for U and Z_* , though Ne3 is also used when available. Examples of this fitting process are shown in the left panels of Figures 9 to 12 for the four MOSDEF [O III] λ 4363 emitters.

We estimate confidence intervals on the best-fit U and Z_* by perturbing the line ratios and direct-method O/H according to the uncertainties, and repeating the fitting procedure above on each realization, 5000 times in total. The uncertainties on U and Z_* thus include uncertainties in the direct-method O/H that sets $Z_{\text{neb}}^{\text{in}}$. The resulting distributions of U , Z_* , and $Z_*/Z_{\text{neb}}^{\text{in}}$ are displayed in the right panels of Figures 9 to 12. The red “X” and lines denote the best fit in each panel.

tude of temperature fluctuations evolves with redshift. There are currently no constraints on the ADF outside of the local universe and no theoretical expectations for an evolving ADF.

Table 3. Constraints on the ionization parameter and stellar metallicity for the $z > 1$ auroral-line sample.

Object	$\log(U)$	$\log(Z_*/Z_{\odot})$	$\log(Z_{\text{neb}}^{\text{in}}/Z_{\odot})$
AEGIS 11452	$-2.33^{+0.20}_{-0.14}$	$-0.73^{+0.51}_{-2.41}$	$-0.72^{+0.21}_{-0.15}$
GOODS-S 41547	$-2.76^{+0.16}_{-0.06}$	$< -0.14^a$	$-0.60^{+0.31}_{-0.22}$
COSMOS 1908	$-1.84^{+0.04}_{-0.18}$	$-1.03^{+0.08}_{-0.72}$	$-0.42^{+0.11}_{-0.14}$
COSMOS 23895	$-2.67^{+0.10}_{-0.06}$	$< -1.55^a$	$-0.45^{+0.25}_{-0.17}$
S13	$-2.30^{+0.05}_{-0.01}$	$< -1.95^a$	$-0.49^{+0.07}_{-0.07}$
J14	$-2.28^{+0.07}_{-0.14}$	$-0.85^{+0.12}_{-2.29}$	$-0.32^{+0.40}_{-0.22}$
C12a	$-2.35^{+0.22}_{-0.05}$	$—^b$	$-0.98^{+0.21}_{-0.20}$
C12b	$-2.80^{+0.01}_{-0.01}$	$-2.02^{+0.01}_{-0.06}$	$-0.30^{+0.03}_{-0.03}$
Ste14c	$-2.11^{+0.04}_{-0.07}$	$-1.72^{+0.28}_{-0.44}$	$-0.29^{+0.04}_{-0.06}$
Ste14a	$-2.33^{+0.09}_{-0.06}$	$< -1.33^a$	$-0.41^{+0.06}_{-0.06}$
Ste14b	$-2.15^{+0.04}_{-0.07}$	$< -0.55^a$	$-0.34^{+0.02}_{-0.06}$
C12c	$-2.27^{+0.04}_{-0.11}$	$-1.20^{+0.14}_{-1.94}$	$-0.68^{+0.01}_{-0.22}$
B14	$-2.23^{+0.05}_{-0.01}$	$< -2.42^a$	$-0.34^{+0.08}_{-0.08}$
composites			
MOSDEF	$-2.63^{+0.08}_{-0.02}$	$< -1.00^a$	$-0.57^{+0.09}_{-0.08}$
KBSS-LM1	$-2.85^{+0.02}_{-0.02}$	$-2.00^{+0.13}_{-0.21}$	$-0.30^{+0.03}_{-0.03}$

^a 3σ upper limit. ^b The 1σ limits on Z_* spanned the entire parameter space, thus no constraint or limit on Z_* was obtained.

Of the 18 $z > 1$ auroral-line emitters in our sample, 4 have limits on the [O II] flux and one lacks [O II] coverage and thus cannot be fit for U and Z_* . For the other 13 objects and two composites, the ionization parameter is always constrained, typically within ± 0.2 dex, and has a weak covariance with Z_* . The stellar metallicity is well-constrained (i.e., 1σ confidence intervals within the explored parameter space) for 6 $z > 1$ galaxies (see, e.g., Figs. 9 and 11), as well as the Steidel et al. (2016) composite. Six of the $z > 1$ galaxies and the MOSDEF stack have one-sided constraints on Z_* (e.g., Figs. 10 and 12), which we display as 3σ upper limits. No targets produced lower limits on Z_* . The single remaining $z > 1$ galaxy (C12a) has a 1σ Z_* confidence interval that spans the full parameter space, thus no constraint could be placed on Z_* , although U could still be constrained with larger uncertainties. The best-fit U and Z_* values assuming the BPASS grids are given in Table 3.

Our methodology of fixing the nebular metallicity of the models to fit for Z_* is complementary to the method of Steidel et al. (2016), who fixed Z_* according to the stacked FUV continuum spectrum and fit for nebular metallicity. For the Steidel et al. (2016) composite, we obtain a best-fit $\log(U) = -2.85$, consistent with their best-fit value of $\log(U) = -2.8$ when employing BPASS binary models with a 100 M_{\odot} IMF cutoff. We find a best-fit stellar metallicity of $Z_*/Z_{\odot} = 0.01$, somewhat lower than the best-fit value of $Z_*/Z_{\odot} = 0.07$ from Steidel et al. (2016). We note that Steidel et al. only considered BPASS models with $Z_*/Z_{\odot} \geq 0.07$ ($Z \geq 0.001$), such that the best-fit stellar metallicity was at the lower bound of the parameter space. In this work, we allow the stellar metallicity of the BPASS models to be as low as $Z_*/Z_{\odot} = 0.0007$ ($Z = 10^{-5}$). It is possible that the FUV continuum of the KBSS-LM1 stack could favor an even lower Z_* if the range of permitted metallicities was increased. We

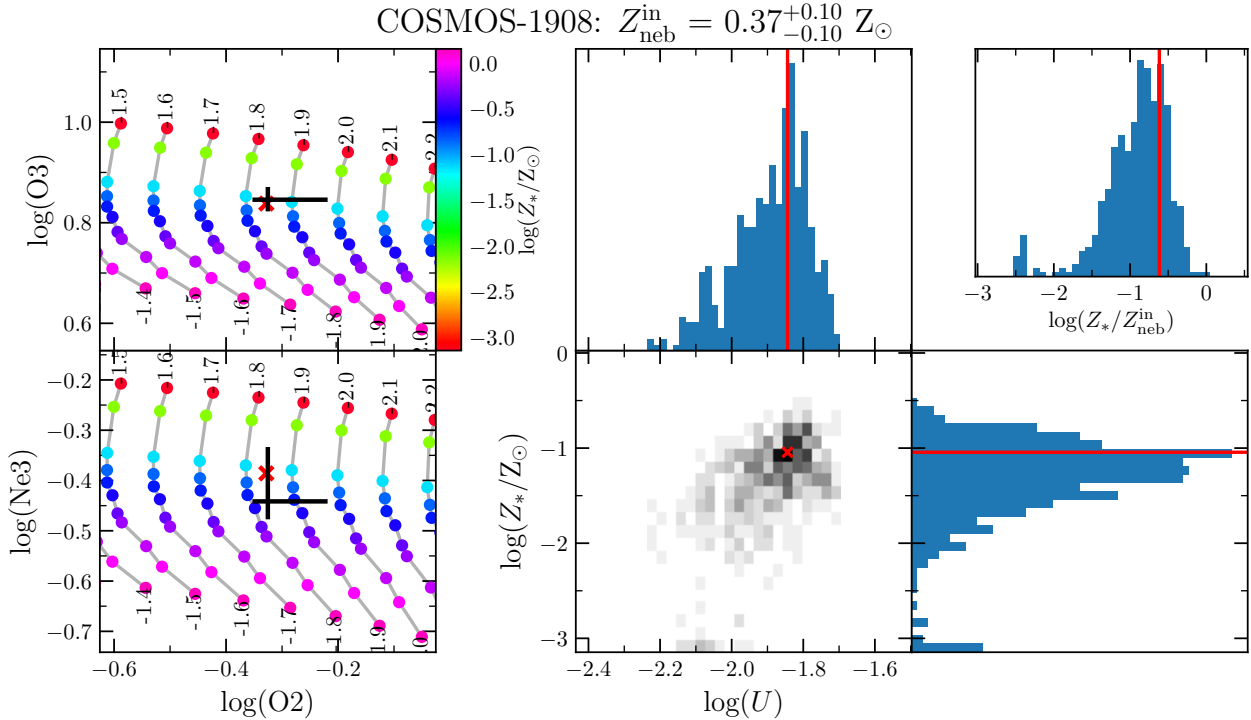


Figure 9. Best-fit solutions for COSMOS-1908 of ionization parameter, U , and stellar metallicity, Z_* , from the BPASS photoionization models. LEFT: Line-ratio diagrams displaying the observed strong-line ratios (black error bars), model grid (colored points and gray lines), and best-fit solution (red X). The displayed model grid has nebular metallicity fixed to the nebular metallicity inferred for COSMOS-1908. Model grid-points are color-coded by stellar metallicity. Gray lines connect points of constant ionization parameter, with the value of $\log(U)$ labeling the lowest and highest stellar metallicity points. RIGHT: Distribution of U and Z_* from Monte Carlo simulations. The best-fit solution is shown by the red lines or red X in each panel. The upper-right panel shows the constraint on $Z_*/Z_{\text{neb}}^{\text{in}}$, which we take to be equivalent to Fe/O.

conclude that both our method and that presented in [Steidel et al. \(2016\)](#) reliably constrain U , but further investigation is required to understand whether both methods infer similar Z_* . In the future, we will analyze individual $z > 1$ galaxies with both auroral-line and FUV spectral continuum measurements to provide a more rigorous validation of these techniques and test of the stellar models.

4.2 Stellar metallicity and O/Fe at $z > 1$

We now utilize these best-fit values of the ionization parameter and stellar metallicity to explore the ionization state of $z > 1$ star-forming regions and the redshift evolution of these properties. In [Figure 13](#), we compare the best-fit Z_* (i.e., Fe/H) with the nebular metallicity $Z_{\text{neb}}^{\text{in}}$ (i.e., O/H) of each $z > 1$ galaxy. The solid black line shows a one-to-one relation where $Z_* = Z_{\text{neb}}^{\text{in}}$ on a solar scale or, equivalently, $\text{O/Fe} = \text{O/Fe}_{\odot}$. Overall, we find a strong preference for super-solar O/Fe ($Z_* < Z_{\text{neb}}^{\text{in}}$).⁶ Only two galaxies have constraints or limits that are consistent with $Z_* = Z_{\text{neb}}^{\text{in}}$, and the one that

is not an upper limit has a large uncertainty towards lower Z_* . The remaining 11 individual galaxies and two composites favor $Z_* < Z_{\text{neb}}^{\text{in}}$.

Six galaxies and the [Steidel et al. \(2016\)](#) stack have inferred Z_* less than $1/5 Z_{\text{neb}}^{\text{in}}$, where $\approx 5 \times \text{O/Fe}_{\odot}$ is the theoretical limit for α -enhancement from pure Type II supernova enrichment (dotted line in [Fig. 13](#); [Nomoto et al. 2006](#)). These galaxies are thus in tension with the standard picture of chemical enrichment through star formation. It is possible that uncertainties on elemental yields in very metal-poor stars ($Z_* < 0.03 Z_{\odot}$) could relieve this tension if metal-poor supernovae have lower Fe yields relative to O. However, some objects fall > 1 dex below the Type II SNe limit. The ionizing spectra of metal-poor massive stars is highly uncertain, and few observational constraints currently exist ([Senchyna et al. 2017, 2019](#); [Stanway & Eldridge 2019](#)). If metal-poor massive stars produce *harder* ionizing spectra than the current stellar models predict, then the true stellar metallicities would in fact be higher.

Alternatively, a top-heavy IMF at high redshifts may relieve tension with the theoretical Type II SNe limit. The limit of $5 \times \text{O/Fe}_{\odot}$ is an IMF-integrated value assuming a canonical high-mass IMF slope of ≈ -2.3 . SNe of very massive ($\gtrsim 25 M_{\odot}$) stars yield $> 10 \times \text{O/Fe}_{\odot}$ ([Nomoto et al.](#)

⁶ The preference for super-solar O/Fe is not driven by our assumption that $\log(Z_{\text{neb}}^{\text{in}}) = \log(Z_{\text{neb}}) + 0.24$. If we instead assumed $Z_{\text{neb}}^{\text{in}} = Z_{\text{neb}}$, O/Hⁱⁿ would be lower than in our fiducial case, but *even lower* values of Z_* (i.e., Fe/H) than those in [Table 3](#) would be required to fit the observed line ratios. In many cases, $Z_* < 0.0007 Z_{\odot}$ (the lowest stellar metallicity in the BPASS mod-

els) would be required ([Fig. 8](#), left column) and the inferred O/Fe would increase compared to our fiducial case.

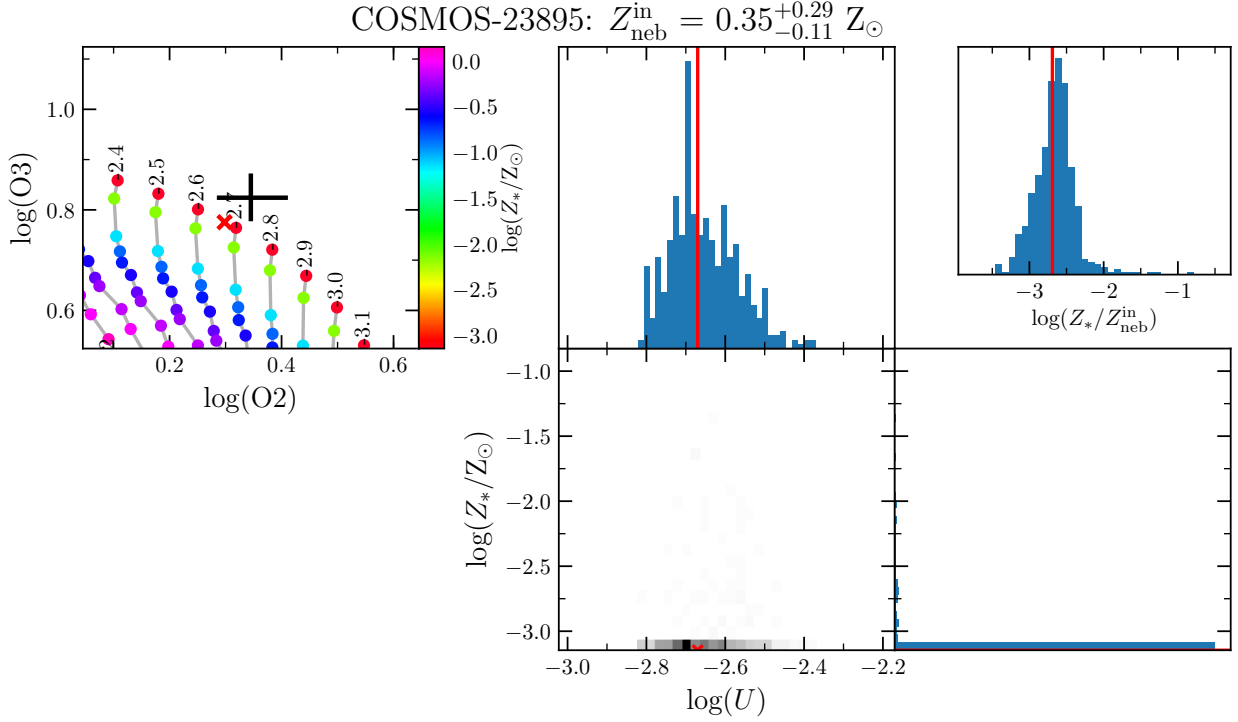


Figure 10. Same as Figure 9 for COSMOS-23895. The best-fit solution is at the lower bound of the explored parameter space for Z_* , thus only a 3σ lower limit on Z_* is obtained.

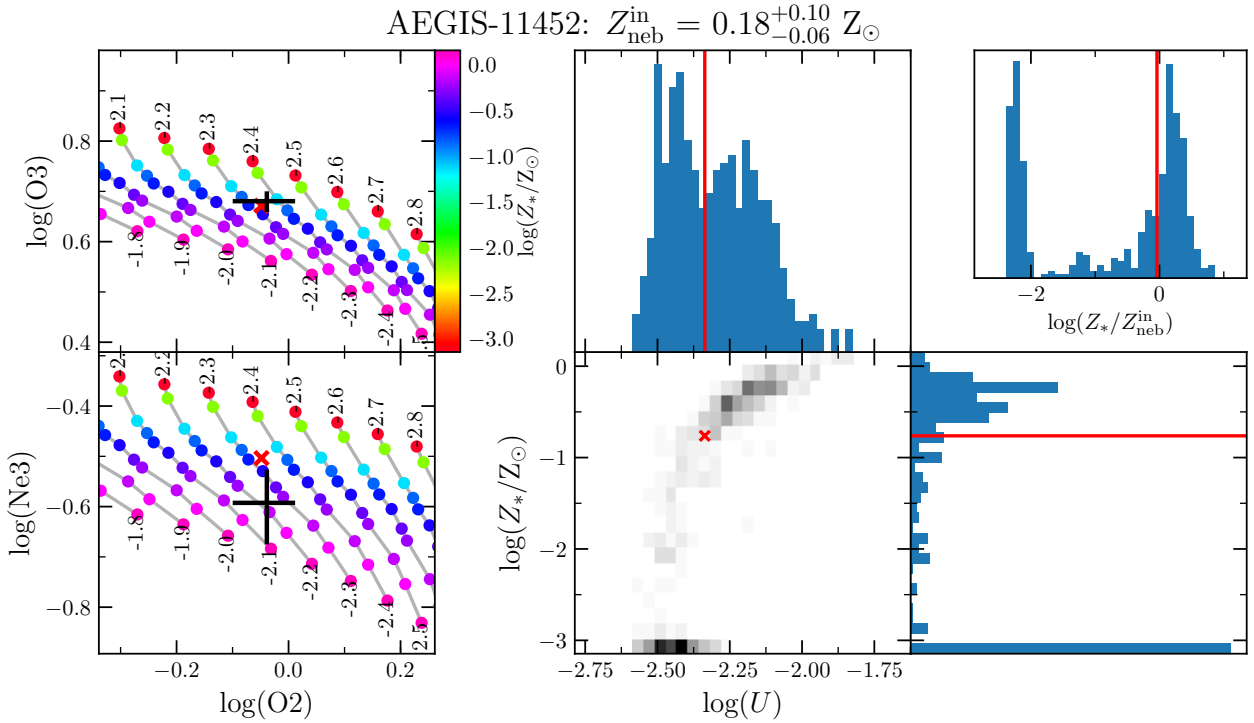


Figure 11. Same as Figure 9 for AEGIS-11452.

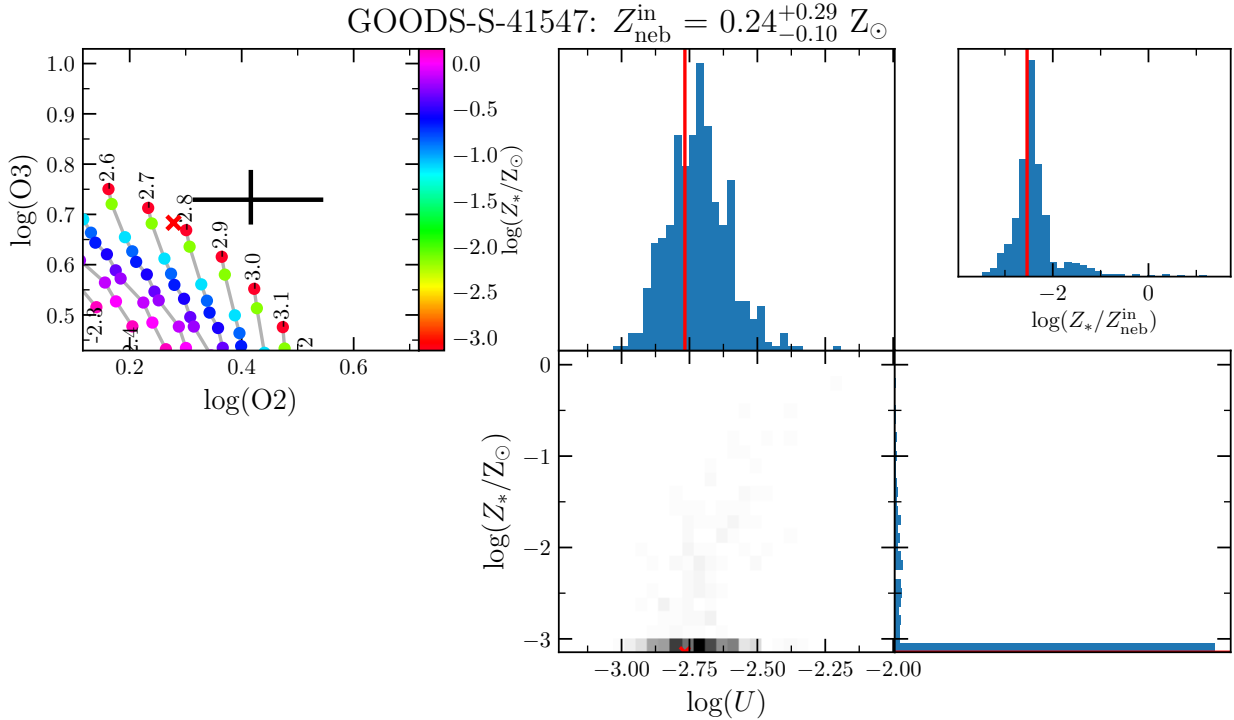


Figure 12. Same as Figure 9 for GOODS-S-41547. The best-fit solution is at the lower bound of the explored parameter space for Z_* , thus only a 3σ lower limit on Z_* is obtained.

2006; Kobayashi et al. 2006), such that the IMF-integrated O/Fe can be larger than $5\times\text{O}/\text{Fe}_\odot$ for top-heavy IMFs (i.e., with high-mass slope shallower than -2.3). A top-heavy IMF would also imply a harder ionizing spectrum at fixed metallicity due to the increased relative abundance of hotter, more massive stars. Thus, for the case of a top-heavy IMF, $> 5\times\text{O}/\text{Fe}_\odot$ is allowed and a higher Z_* (i.e., Fe/H) would best fit the observed line ratios compared to the values of Z_* inferred under our fiducial model (assuming a Chabrier 2003 IMF), lowering the inferred O/Fe. Recent observational and theoretical work has suggested that the IMF grows more top-heavy in low-metallicity and high-SFR environments common among high-redshift galaxies (Jeřábková et al. 2018; Schneider et al. 2018). The potential impact of IMF variations on the ionizing spectrum in high-redshift star-forming regions should be further investigated in future work.

Despite the large uncertainty on the ionizing spectra of metal-poor stellar populations at high redshift, our results still strongly disfavor a scenario in which $Z_* = Z_{\text{neb}}^{\text{in}}$, which would occur at stellar metallicities where better observational constraints are available ($\sim 1/3 - 1/2 Z_\odot$). A third possibility is that the sources below the Type II SNe limit have additional ionization mechanisms beyond star formation that harden the galaxy-averaged ionizing spectrum, such as shocks or weak AGN. The galaxies in the $z > 1$ sample do not exhibit any obvious signatures of AGN, but a low-luminosity AGN in a highly star-forming galaxy may only slightly shift the observed line ratios. However, it is unlikely that the presence of shocks or AGN are responsible for the position of the Steidel et al. (2016) stack of 30 galaxies unless such a phenomenon is ubiquitous among typical star-forming galaxies at $z \sim 2$. Ultimately, we require more

confidence in stellar models of metal-poor ($\lesssim 0.2 Z_\odot$) massive stars to understand the behavior of galaxies falling below the Type II SNe limit.

We show the O/Fe ratio as a function of stellar population age for the MOSDEF [O III] $\lambda 4363$ emitters and stack in Figure 14. The stellar population age is derived from the best-fit SED models, and O/Fe is on a solar scale such that $[\text{O}/\text{Fe}] = \log((\text{O}/\text{Fe})/(\text{O}/\text{Fe}_\odot))$. We find that all four galaxies have young stellar populations (< 300 Myr), with three younger than 100 Myr. Two of the MOSDEF galaxies are constrained to have super-solar O/Fe, while the other two do not have strong constraints. The composite spectrum yields a 3σ lower-limit of $\text{O}/\text{Fe} \approx 3\times\text{O}/\text{Fe}_\odot$. The ages of the MOSDEF [O III] $\lambda 4363$ emitters are consistent with the presence of super-solar O/Fe from an enrichment history dominated by Type II SNe, with solar O/Fe expected to be reached only at ages $\gtrsim 1$ Gyr. The [O III] $\lambda 4363$ emitters have ages younger than 90% of MOSDEF star-forming galaxies matched in M_* and redshift. While the precise stellar population ages are significantly uncertain due to systematics associated with the assumed star-formation history, attenuation law, and metallicity for SED fitting, relative ages should be robust under our assumption of constant star formation. Furthermore, the large sSFRs and emission-line equivalent widths of the $z > 1$ sample (Table 2) suggest very young ages, in agreement with results from the SED fitting. The four MOSDEF [O III] $\lambda 4363$ emitters appear to be very young star-forming galaxies in which the delayed Fe enrichment from Type Ia SNe has not yet occurred for the bulk of past star formation.

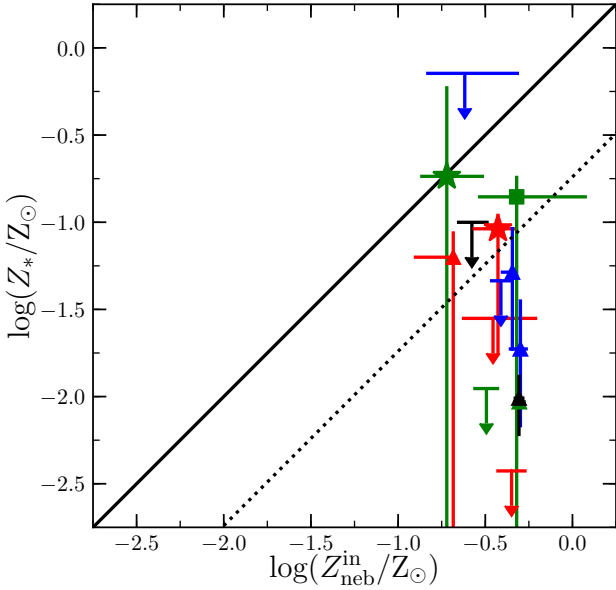


Figure 13. Best-fit stellar metallicity (Z_*) vs. input nebular metallicity ($Z_{\text{neb}}^{\text{in}}$) for $z > 1$ galaxies. The input nebular metallicity is set by adding 0.24 dex to the observed direct-method $12+\log(\text{O}/\text{H})$ given in Table 2. Points and color-coding are as in Figure 3. The solid black line shows a one-to-one relation, while the dotted black line shows $Z_* = 1/5 Z_{\text{neb}}^{\text{in}}$, the theoretical limit from pure Type II SNe enrichment (Nomoto et al. 2006). The $z > 1$ sample strongly prefers $Z_{\text{neb}}^{\text{in}} > Z_*$ (i.e., super-solar O/Fe).

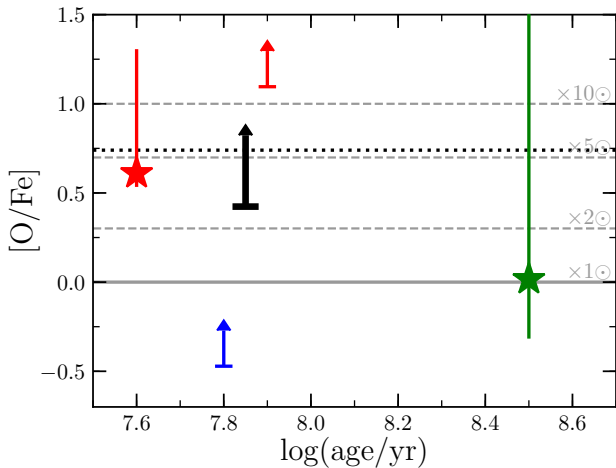


Figure 14. O/Fe abundance ratio relative to the solar value vs. stellar population age from SED fitting for the four MOSDEF [O III] $\lambda 4363$ metallicity sample. Points are color-coded by redshift as in Figure 3. The thick black point shows the value inferred from the MOSDEF [O III] $\lambda 4363$ composite spectrum, adopting the median age of the individual galaxies. The black dashed line shows the theoretical upper-limit of $[\text{O}/\text{Fe}]=0.74$ from pure Type II SNe enrichment at $Z_* = 0.07 Z_{\odot}$ (Nomoto et al. 2006). Gray lines show 1, 2, 5, and 10 times $\text{O}/\text{Fe}_{\odot}$.

4.3 Ionization parameter at $z > 1$

The $z > 1$ star-forming galaxy population has considerably higher ionization parameters than are typical of $z \sim 0$ samples (e.g., SDSS), as evidenced by significantly higher O32 and O3 at fixed M_* (e.g., Nakajima & Ouchi 2014; Sanders et al. 2016a, 2018; Dickey et al. 2016; Holden et al. 2016; Kashino et al. 2017; Strom et al. 2017; Kashino et al. 2019). sSFR has been shown to strongly correlate with O32 and O3 (e.g., Nakajima & Ouchi 2014; Sanders et al. 2016a; Kewley et al. 2015; Dickey et al. 2016; Kashino & Inoue 2019), and is consequently closely tied to U . However, sSFR is anticorrelated with O/H according to the M_* -SFR-O/H relation present at low and high redshifts: galaxies with higher SFR at fixed M_* (i.e., higher sSFR) have lower O/H (e.g., Mannucci et al. 2010; Lara-López et al. 2010; Andrews & Martini 2013; Sanders et al. 2018). Furthermore, U is tightly anticorrelated with O/H in the local universe (Dopita et al. 2006b,a; Pérez-Montero 2014; Sánchez et al. 2015; Kashino & Inoue 2019). It is therefore possible that the high values of U inferred at high redshifts are simply a byproduct of the lower metallicities and higher sSFRs of high-redshift galaxies compared to the local universe. It has been proposed that the redshift evolution of strong-line ratio sequences is primarily driven by enhanced U at high redshifts compared to typical $z \sim 0$ values at fixed O/H (Kewley et al. 2015, 2016; Kashino et al. 2017, 2019; Kaasinen et al. 2018). In other words, the U -O/H relation evolves with redshift such that U increases at fixed O/H with increasing redshift. We test this scenario by comparing U , sSFR, and direct-method O/H of our $z > 1$ sample to the corresponding measurements of local star-forming galaxies.

Figure 15 compares U , sSFR, and temperature-based O/H for the $z > 1$ auroral-line sample and $z \sim 0$ M_* -binned composites of Andrews & Martini (2013). We determine U for the Andrews & Martini (2013) stacks using the same models and fitting procedure described in Section 4.1, except that we fix $Z_* = Z_{\text{neb}}^{\text{in}}$ as expected for $z \sim 0$ galaxies with more extended star-formation histories than high-redshift galaxies. We note that allowing Z_* to vary freely does not significantly change the results. Median values of the $z > 1$ sample of individual galaxies are also displayed in each panel as a open black diamond.

As expected, we find that U is anticorrelated with O/H for $z \sim 0$ galaxies, as shown in the top panel of Figure 15. We find our mean U -O/H relation for $z \sim 0$ SDSS stacks closely matches that found by Pérez-Montero (2014) for $z = 0$ H II regions (shaded light gray region). The $z > 1$ auroral-line sample scatters above and below the local relation defined by the $z \sim 0$ stacks. We do not have a suitable sample size or dynamic range in O/H to look for an anticorrelation among the high-redshift galaxies alone. The $z > 1$ galaxies display a significant scatter in U at fixed O/H, but the intrinsic scatter is similar to the range spanned by local H II regions after accounting for measurement uncertainties, ~ 0.25 dex in U at fixed O/H. The median values of the $z > 1$ sample are $12+\log(\text{O}/\text{H})^{\text{med}} = 8.02^{+0.06}_{-0.09}$ and $\log(U)^{\text{med}} = -2.30^{+0.06}_{-0.06}$. The median of the $z > 1$ sample is in remarkable agreement with the $z \sim 0$ U -O/H relation of both local galaxies and individual H II regions.

We show U vs. sSFR in the middle panel of Figure 15. We find a correlation between U and sSFR among the $z \sim 0$

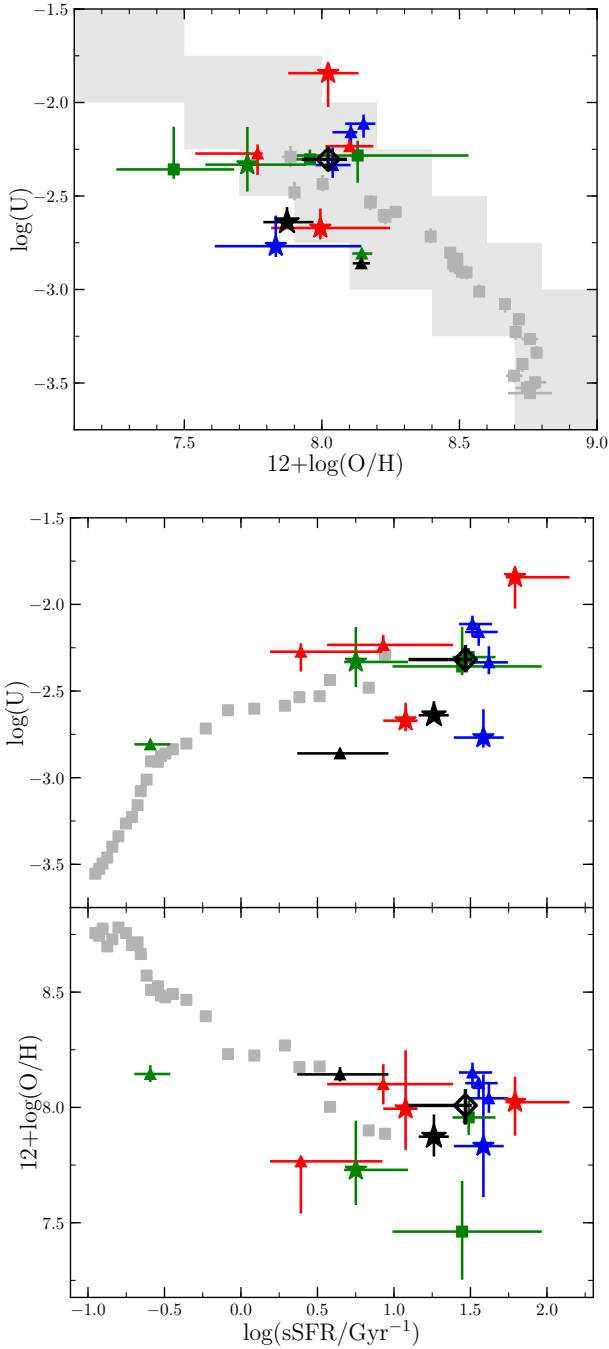


Figure 15. Relationships between U , direct-method nebular O/H , and $sSFR$ for $z > 1$ galaxies (colored points) and stacked spectra of $z \sim 0$ galaxies (gray points; [Andrews & Martini 2013](#)). Shapes and colors are as in [Figure 3](#), with the black open diamond denoting the median of the $z > 1$ sample. The light-gray shaded region in the top panel shows the range of U and $12+\log(O/H)$ of local $H\ II$ regions found by [Pérez-Montero \(2014\)](#). On average, galaxies at $z > 1$ do not show a significant offset from the mean $z \sim 0$ U - O/H , U - $sSFR$, and $sSFR$ - O/H relations.

stacks. Once again, the $z > 1$ auroral-line sample scatters both above and below the $z \sim 0$ relation. Interestingly, the lowest- $sSFR$ galaxy in the $z > 1$ sample (C12b; [Christensen et al. 2012a,b](#)), with $sSFR \sim 1.5$ dex below the sample average, falls directly on the $z \sim 0$ relation and has a particularly tightly-constrained U and O/H . The lowest-mass [Andrews & Martini \(2013\)](#) bins have similar $sSFR$ to the range spanned by the $z > 1$ sample ([Fig. 5](#)). The median $z > 1$ values fall on the U - $sSFR$ relation defined by the $z \sim 0$ composites.

In the bottom panel of [Figure 15](#), we present O/H vs. $sSFR$, finding the anticorrelation between O/H and $sSFR$ at $z \sim 0$ as expected from the FMR. The $z > 1$ galaxies follow the same relation between O/H and $sSFR$ displayed by the $z \sim 0$ galaxies. This result is expected based on the agreement between $z \sim 0$, $z \sim 0.8$, and $z \sim 2.2$ samples in the FMR projection shown in the bottom panel of [Figure 7](#). The $z > 1$ median falls on the extrapolation of the relation displayed $z \sim 0$ stacks with lower $sSFR$.

In summary, [Figure 15](#) shows that, on average, the $z > 1$ galaxies fall on the local relationships between U , O/H , and $sSFR$. The high ionization parameters of the $z > 1$ sample are therefore as expected in accordance with their low metallicities and high $sSFR$ s, and are not in excess of what is expected at fixed O/H compared to $z \sim 0$ galaxies. This result suggests that variations in U beyond local relations is not a significant driver of the evolving strong-line ratios of galaxies. Combining these results with those presented in [Section 4.2](#), we conclude that the primary cause of strong-line ratio evolution at fixed O/H ([Fig. 3](#)) for our $z > 1$ auroral-line sample is a harder ionizing spectrum at fixed nebular metallicity compared to what is typical in $z \sim 0$ galaxy populations. The harder spectrum at fixed O/H in the $z > 1$ auroral-line sample is naturally explained by the youth of their stellar populations, leading to chemically-immature galaxies that have super-solar O/Fe due to the predominance of Type II SNe enrichment that promptly produces O and a lack of time-delayed Type Ia SNe that are the main source of Fe . The Fe -poor massive stars produce harder ionizing spectra than their counterparts at solar O/Fe .

5 DISCUSSION

In this work, we have used a sample of 18 individual $z > 1$ galaxies with direct-method metallicities to test strong-line metallicity indicators, construct the mass-metallicity relationship, investigate the redshift invariance of the M_* - $sSFR$ - O/H relation, and demonstrate that the high ionization state of this sample is driven by an ionizing spectrum that is harder than that of $z \sim 0$ galaxies at fixed O/H . In this section, we discuss the implications of these results for typical galaxy populations at $z \sim 1 - 3$, extreme emission-line galaxy samples at $z \sim 1 - 3$, and galaxies in the epoch of reionization at $z > 6$.

5.1 Implications for typical $z \sim 1 - 3$ galaxies

Obtaining accurate metallicity estimates from strong-line ratios for large existing spectroscopic survey data sets at $z \sim 1 - 3$ (e.g., MOSDEF, [Kriek et al. 2015](#); KBSS, [Steidel et al. 2014](#); 3D-HST, [Brammer et al. 2012a](#); FMOS-COSMOS, [Kashino et al. 2019](#)) requires knowledge of the

ionization state of the ISM in typical high-redshift galaxies. We have shown that our $z > 1$ auroral-line sample has significantly higher SFR at fixed M_* than galaxies falling on the mean M_* -SFR relation at the same redshifts (Fig. 5). We now put the $z > 1$ auroral-line sample in the context of a representative sample of star-forming galaxies at $z \sim 2.3$, and discuss which conclusions, if any, can be extended to the typical galaxy population at $z > 1$.

In Figure 16, we present SFR, O32, and $EW_0([\text{O III}]\lambda 5007)$ as a function of stellar mass. We compare the $z > 1$ auroral-line sample (red points) to a sample of $z \sim 2.3$ star-forming galaxies from MOSDEF representative of the typical population at $\log(M_*/M_\odot) = 9 - 11$ from Sanders et al. (2018) (open blue circles). Black circles show the mean properties of this sample obtained via spectral stacking in four M_* bins, where we have derived the mean $EW_0([\text{O III}]\lambda 5007)$ in each bin according to the method described in Section 2.3.1. We find that all but two galaxies in the auroral-line sample (median redshift of 2.2) fall above the mean $z \sim 2.3$ M_* -SFR relation, with a mean offset of $\langle \Delta \log(\text{SFR}) \rangle \sim 0.6$ dex. The O32 values of the typical $z \sim 2.3$ sample are much lower than those of the auroral-line sample, but the typical sample has a significantly higher average stellar mass. When comparing at $\log(M_*/M_\odot) = 9.0 - 9.5$ where the two samples overlap, the auroral-line sample has O32 values ~ 0.5 dex higher on average. The equivalent widths of the auroral-line sample span $EW_0([\text{O III}]\lambda 5007) = 300 - 2000 \text{ \AA}$, with a median value of $\sim 500 \text{ \AA}$. This value is much larger than the mean value of the $z \sim 2.3$ comparison sample ($\sim 100 \text{ \AA}$). It is important to take into account the fact that $EW_0([\text{O III}]\lambda 5007)$ has a strong dependence on stellar mass (Reddy et al. 2018). However, even when comparing at fixed M_* , the auroral-line sample displays $EW_0([\text{O III}]\lambda 5007)$ that is larger by a factor of 3.

We show O32 and $EW_0(\text{H}\beta)$ vs. $EW_0([\text{O III}]\lambda 5007)$ in Figure 17, and once again find that the auroral-line sample is nearly disjoint from the typical $z \sim 2.3$ sample, having higher emission-line equivalent widths suggestive of younger ages and higher O32 values implying lower O/H and higher U . We select the subset of the $z \sim 2.3$ comparison sample with $EW_0([\text{O III}]\lambda 5007) > 300 \text{ \AA}$ (matched to the auroral-line sample), displayed as filled blue circles in Figures 16 and 17. The EW-matched $z \sim 2.3$ sample reproduces the properties of the auroral-line sample in the range of stellar mass overlap, selecting a subset lying above the M_* -SFR relation at $\log(M_*/M_\odot) = 9.0 - 9.5$ with similarly high O32 values. However, this EW-matched subset makes up only 11% (22/203) of the typical $\log(M_*/M_\odot) \gtrsim 9.0$ star-forming population at $z \sim 2.3$ from MOSDEF.

Based on the high sSFRs, O32 values, and emission-line equivalent widths, the $z > 1$ auroral-line sample is made up of galaxies that are younger and more metal-poor than the bulk of the typical $z \sim 1 - 3$ galaxy population at $\log(M_*/M_\odot) > 9.0$, the mass range that most high-redshift spectroscopic surveys probe. Accordingly, it is not clear that our conclusions regarding metallicity calibration evolution and O/Fe enhancement apply to the bulk of the $z \sim 2$ star-forming population. Based on the high-redshift analog O32 strong-line calibration of BKD18, $\sim 90\%$ of the $z \sim 2.3$ comparison sample has oxygen abundances higher than $12 + \log(\text{O}/\text{H}) = 8.14$, the highest direct-method O/H of

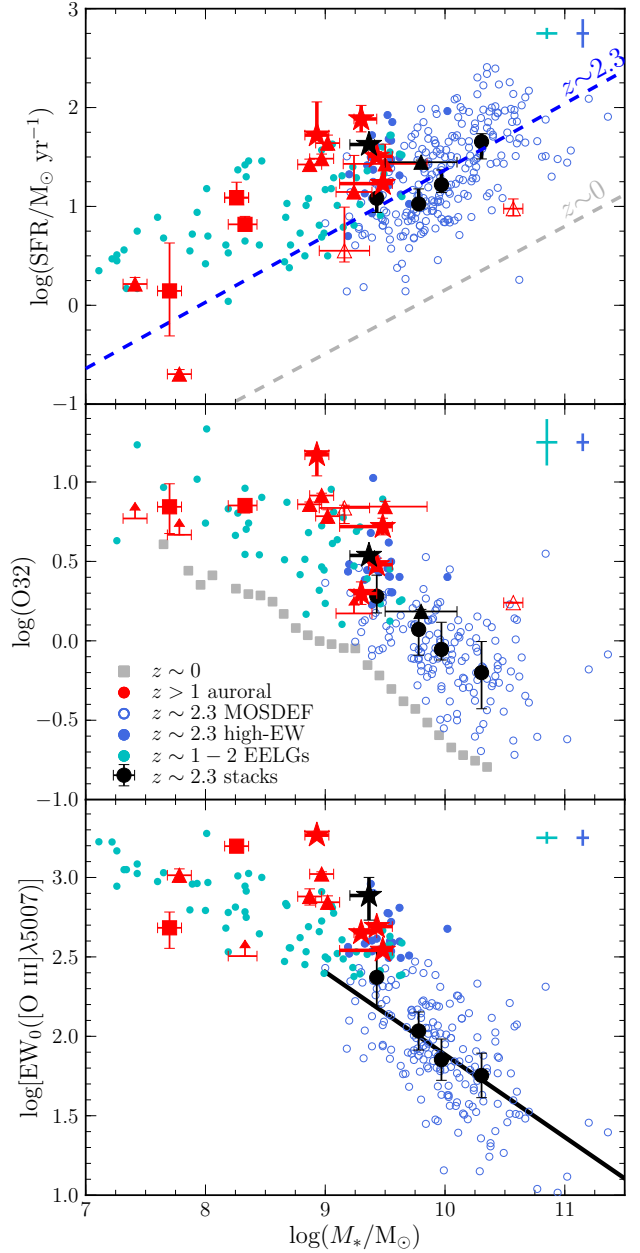


Figure 16. SFR (top), O32 (middle), and $EW_0([\text{O III}]\lambda 5007)$ (bottom) vs. M_* for high-redshift galaxy samples. The $z > 1$ auroral-line sample is shown as red points, with shapes as in Fig. 3. Hollow triangles denote the two probable mergers (C12b and C12c). Open blue circles display a representative sample of $z \sim 2.3$ star-forming galaxies from MOSDEF (Sanders et al. 2018), while filled blue circles denote the subset of that sample with $EW_0([\text{O III}]\lambda 5007) > 300 \text{ \AA}$. The $z \sim 2$ extreme emission-line galaxy sample of Tang et al. (2018) is presented as cyan circles. In each panel, the cyan and blue error bar denotes the mean uncertainty of the Tang et al. (2018) and $z \sim 2.3$ MOSDEF samples, respectively. Composite spectra are shown in black for the stack of MOSDEF $[\text{O III}]\lambda 4363$ emitters (star), Steidel et al. (2016, ; triangle), and typical $z \sim 2.3$ MOSDEF galaxies (circles; Sanders et al. 2018). The blue dashed line in the top panel shows the best-fit M_* -SFR relation of equation 8. Gray points and dashed line show mean $z \sim 0$ relations (Andrews & Martini 2013). The mean $z \sim 2.3$ $EW_0([\text{O III}]\lambda 5007)$ vs. M_* relation from Reddy et al. (2018) is shown as the solid black line in the bottom panel.

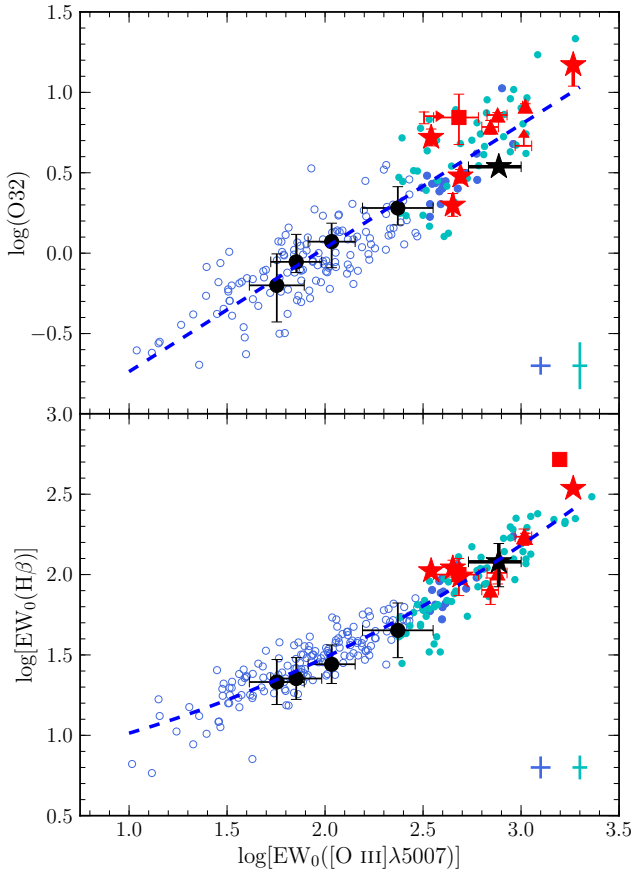


Figure 17. O32 (top) and $EW_0(H\beta)$ (bottom) as a function of $EW_0([O\ III]\lambda 5007)$. Points are as in Figure 16. Both panels display remarkably tight correlations over 2.5 orders of magnitude in $EW_0([O\ III]\lambda 5007)$.

the auroral-line sample. Therefore, the strong-line indicators considered in Figure 3 have not been tested over the metallicity range of the bulk of the $\log(M_*/M_\odot) > 9.0$ galaxy population at $z \sim 2$. However, given that the auroral-line sample represents the most extreme subset of the MOSDEF $z \sim 2.3$ sample, it is expected that the strong-line ratio vs. O/H relations of typical $z \sim 2$ galaxies will show *at most* the same level of evolution as the auroral-line sample (~ 0.1 dex in O/H at fixed strong-line ratio). The BKD18 high-redshift analog calibrations are likely good to within the same amount for the typical $z \sim 2$ population when calculating sample average abundances.

The very young ages of the auroral-line sample implied by large emission-line equivalent widths and sSFRs are consistent with the super-solar O/Fe values found from the photoionization models. However, typical $z \sim 2$ galaxies at $\log(M_*/M_\odot) > 9.0$ appear to have older stellar populations. Star-forming galaxies with stellar populations 300 Myr to ~ 1 Gyr old may still display some level of O/Fe enhancement relative to solar values, while the abundance ratios of galaxies older than ~ 1 Gyr will lie close to O/Fe_\odot . The age of the universe at $z = 2.3$ is 2.8 Gyr, and can thus accommodate stellar populations older than 1 Gyr. Reddy et al. (2018) find that galaxies with $EW_0([O\ III]\lambda 5007) < 100 \text{ \AA}$

(the typical value at $\log(M_*/M_\odot) \sim 10.0$ and $z \sim 2.3$) have ages > 1 Gyr according to SED fitting. It is therefore possible that roughly half of the $z \sim 2.3$ MOSDEF sample has O/Fe_\odot while the other half has enhanced O/Fe. However, ages inferred from SED fitting are sensitive to assumptions regarding the stellar population models, stellar metallicity, attenuation curve, and star-formation history, such that there are large systematic uncertainties on the ages.

To confirm or deny the presence of O/Fe enhancement in the typical $z \sim 2$ population requires measurements of either auroral-lines or high-S/N rest-FUV continuum, from which Fe/H can be inferred, for individual galaxies spanning the M_* -SFR relation. Detecting $[O\ III]\lambda 4363$ is currently out of reach for galaxies on the mean M_* -SFR relation where fluxes are expected to be $\sim 5 - 200$ times weaker than for the MOSDEF $[O\ III]\lambda 4363$ emitters in this work. With current facilities, obtaining high-S/N spectra of the rest-FUV is the most viable option over a wide range of M_* , SFR, and metallicity, especially for massive metal-rich galaxies.

If the $z \sim 2$ star-forming population is “mixed” as implied by the ages in Reddy et al. (2018), with chemically-immature low-mass galaxies having super-solar O/Fe and mature high-mass galaxies having solar O/Fe, it carries implications for measurements of metallicity scaling relations. Assuming a single metallicity calibration in one of the two extremes (i.e., the high-redshift analog vs. $z \sim 0$ reference calibrations of BKD18) would lead to systematic biases in the slope of the MZR, such that the measured MZR would be artificially steepened. If such a scenario holds, a different metallicity calibration must be applied in the low- and high-mass regimes, or else age-dependent calibrations must be constructed. There is likely an age gradient above and below the M_* -SFR relation as well, which will bias measurements of the M_* -SFR-O/H relation for a mixed population. The strong-line metallicities of the highest-sSFR local galaxies, analogous to $z \sim 2$ systems, may also be biased. To fully characterize the evolution of gas-phase metallicity with global galaxy properties, we must understand at what redshift O/Fe enhancement begins affecting the star-forming population, the relation of O/Fe with M_* and SFR, and at what redshift the full star-forming population is dominated by Type II SNe enrichment.

Steidel et al. (2016) find super-solar O/Fe using a composite spectrum of 30 star-forming galaxies at $z \sim 2.3$ falling on the M_* -SFR relation, and we find consistent results when applying our methodology. This finding may signify that many $z \sim 2$ galaxies on the M_* -SFR relation are O/Fe enhanced, but the sample-averaged measurement cannot address how O/Fe varies across the sample, a pressing question given that stellar population age (and thus O/Fe) varies with M_* and sSFR. Additionally, there are concerns that the Steidel et al. (2016) KBSS-LM1 stack may be biased such that it is not representative of typical $z \sim 2$ samples. In Figure 15, the KBSS-LM1 stack (black triangle) has a peculiar low ionization parameter for its direct-method O/H and sSFR, falling significantly below the $z \sim 0$ relations and lower than any galaxies in our $z > 1$ sample. Expectations are that high-redshift galaxies will have *at least* as high U as local galaxies at fixed O/H and sSFR. The offset of the KBSS-LM1 stack is much more significant than individual galaxies scattering low in these relations since it is an average of 30 galaxies. It is possible that the stacking procedure

ture has systematically biased the rest-optical lines towards lower-excitation ratios. Individual determinations of O/Fe (via auroral lines or rest-UV continuum) at higher M_* and lower sSFR than our $z > 1$ auroral-line sample are sorely needed to validate stacking methods and explore O/Fe as a function of galaxy properties.

Steidel et al. (2016) and Strom et al. (2018) find that harder ionizing spectra at fixed O/H produced by super-solar O/Fe stellar populations are responsible for driving the well-known offset of $z \sim 2$ galaxies from the local star-forming sequence in the [N II] BPT diagram. Strom et al. (2018) further find that elevated N/O at fixed O/H is required to explain the most highly-offset $z \sim 2$ objects. Our results are consistent with this scenario. However, with the current sample, we cannot evaluate whether this is the case for the more massive galaxies for which the [N II] BPT offset is observed, if O/Fe enhancement alone can fully account for the observed offset, and what the role of N/O variation is. Our current $z > 1$ auroral-line sample lacks [N II] coverage and detections in most galaxies. Future high-redshift auroral-line samples spanning a wider dynamic range in M_* and metallicity will directly address the nature of the [N II] BPT diagram offset.

5.2 Implications for $z \sim 1 - 3$ extreme emission-line galaxies

Extreme emission-line galaxies (EELGs) are a population of galaxies with spectra dominated by high equivalent width emission lines, including the “green peas” in the local universe (Cardamone et al. 2009). The large equivalent widths of our $z > 1$ auroral-line sample imply similarities to EELGs. We show the EELG sample of Tang et al. (2018) at $1.3 < z < 2.4$ in Figures 15 and 16 (cyan points). This sample was selected to have $EW_0([\text{O III}]\lambda 5007) > 300 \text{ \AA}$. We find that the $z > 1$ auroral-line sample spans a similar range of SFR, O32, and $EW_0([\text{O III}]\lambda 5007)$ at fixed M_* as the EELGs, which are high-excitation galaxies lying above the M_* -SFR relation at $\log(M_*/M_\odot) \sim 7 - 9.5$. The high-EW $z \sim 2.3$ MOSDEF subsample overlaps with the most massive EELGs.

In Figure 16, the auroral-line sample again aligns with the EELG sample, with similar O32 and $EW_0(\text{H}\beta)$ at fixed $EW_0([\text{O III}]\lambda 5007)$. The EELGs appear to be a continuation of the relation between O32, $EW_0(\text{H}\beta)$, and $EW_0([\text{O III}]\lambda 5007)$ defined by the $z \sim 2.3$ MOSDEF sample, forming remarkably tight sequences over 2.5 orders of magnitude in $EW_0([\text{O III}]\lambda 5007)$. We fit these relations, obtaining:

$$\log(\text{O32}) = 0.77x - 1.50 \quad (12)$$

$$\log[EW_0(\text{H}\beta)] = 0.12x^2 + 0.12x + 0.77 \quad (13)$$

where $x = \log[EW_0([\text{O III}]\lambda 5007)]$, with 0.18 and 0.11 dex scatter in O32 and $EW_0(\text{H}\beta)$, respectively. These relations can be used to obtain rough information about the O/H and ionization parameter of galaxies with large equivalent widths where $EW_0([\text{O III}]\lambda 5007)$ can be inferred from broadband photometry.

Given the common properties of the $z \sim 2$ EELGs and $z > 1$ auroral-line sample, we conclude that the EELGs are

also young metal-poor galaxies with super-solar O/Fe, driving extremely hard ionizing spectra in their H II regions. By modeling the photometry and rest-optical spectra simultaneously, Tang et al. (2018) find ages younger than 300 Myr for the majority of their sample. Tang et al. (2018) suggest EELGs have hard ionizing spectra and high ionization parameters based on their large O32 values. The O32 high-redshift analog calibration of BKD18 yields metallicities spanning $12 + \log(\text{O}/\text{H}) = 7.7 - 8.4$ for the EELG sample, with a median of $12 + \log(\text{O}/\text{H})_{\text{med}} = 8.07$, similar to the O/H distribution of the auroral-line sample. At these metallicities, the $z = 0$ U-O/H relation predicts high ionization parameters of $\log(U) = -2.0$ to -2.5 (Pérez-Montero 2014). When modeling the nebular spectra of EELGs, we suggest using BPASS models including binaries, and assuming $Z_* = 1/5Z_{\text{neb}}$ (the pure Type II SNe limit) and the $z = 0$ U-O/H relation.

5.3 Implications for typical $z > 6$ galaxies and reionization

Star-forming galaxies at $z > 6$ are thought to be the sources of ionizing photons that powered reionization (e.g., Bouwens et al. 2012, 2015; Robertson et al. 2015; Stark 2016). Through SED fitting and broadband photometric excess, these galaxies have been found to have very large $EW_0([\text{O III}]\lambda 5007)$, with typical values of $\sim 670 \text{ \AA}$ and extending up to $> 1500 \text{ \AA}$ for extreme sources, and high sSFRs ($\sim 10 \text{ Gyr}^{-1}$) (Labbé et al. 2013; Smit et al. 2014, 2015; Roberts-Borsani et al. 2016). These properties are similar to those of the $z > 1$ auroral-line sample and the $z \sim 2$ EELGs. Indeed, the Tang et al. (2018) sample was selected to be analogs of epoch of reionization galaxies. Given the similar properties of these two samples, we suggest that typical star-forming galaxies at $z > 6$ have super-solar O/Fe.

The age of the universe at $z = 6$ is 900 Myr. Assuming the first galaxies began forming ~ 200 Myr after the big bang, the oldest possible stellar populations at $z = 6$ would have an age of ~ 700 Myr. This maximum age would decrease at higher redshifts when reionization was in progress (~ 400 and 250 Myr at $z = 8$ and 10 , respectively). A spectroscopically-confirmed $z \sim 10$ galaxy has been found to have an age of 340 Myr, close to the age limit (Hoag et al. 2018). Labbé et al. (2013) find a younger age of 100 Myr for a stacked SED of $z \sim 8$ galaxies. Due to the maximum possible age of galaxies at $z > 6$, every galaxy in the epoch of reionization should host an O/Fe-enhanced stellar population. The properties of our $z > 1$ auroral-line sample provide observational evidence for this expectation. Just as for $z \sim 1 - 3$ EELGs, we suggest employing BPASS binary stellar models with $Z_* = 1/5Z_{\text{neb}}$ and the local relation between U and O/H when modeling the nebular spectra of $z > 6$ galaxies. Based on the results in Figure 3, we find that the most useful strong-line ratios for determining gas-phase oxygen abundance from rest-optical spectroscopy of $z > 6$ galaxies are O32 and Ne3O2, which will be accessible out to $z \sim 9$ and 12 , respectively, with JWST/NIRSpec and NIRCам spectroscopy. While it is possible that [N II]-based indicators may also be useful, these can only be observed out to $z \approx 6.6$ with NIRSpec and NIRCам.

Super-solar O/Fe values carry important implications for reionization. Massive stars with lower Fe abundances produce harder spectra and a larger number of ionizing

photons per unit stellar mass. The latter makes it easier for star-forming galaxies to reionize the universe, requiring lower escape fractions. Low-mass, faint galaxies are thought to provide the bulk of the ionizing photons due to their number (e.g., [Bouwens et al. 2012, 2015](#); [Finkelstein et al. 2012](#); [Stark 2016](#)). Such galaxies should form latest and thus have the youngest stellar populations with maximal $O/Fe \approx 5 \times O/Fe_{\odot}$ based on current Type II SNe yields ([Nomoto et al. 2006](#)). Assuming $z > 6$ galaxies follow the relations in Figure 17, we use equations 12 and 13 to estimate O32 values of $z > 6$ galaxies. [Labbé et al. \(2013\)](#) use stacked broadband photometry to estimate $EW_0([O\ III]+H\beta) = 670\ \text{\AA}$ of L^* galaxies at $z \sim 8$. This equivalent width corresponds to $EW_0([O\ III]\lambda 5007) = 420\ \text{\AA}$, $EW_0(H\beta) = 80\ \text{\AA}$, $\log(O32) = 0.52$, and $12 + \log(O/H) = 8.15$ ($0.3 Z_{\odot}$), assuming the high-redshift analog O32 calibration of BKD18. In the case of $5 \times O/Fe_{\odot}$, the stellar metallicity would be $Z_* = 0.06 Z_{\odot}$. [Roberts-Borsani et al. \(2016\)](#) find $EW_0([O\ III]+H\beta) \sim 1500\ \text{\AA}$ for four bright galaxies at $z \sim 7-9$, implying $EW_0([O\ III]\lambda 5007) = 1000\ \text{\AA}$, $EW_0(H\beta) = 160\ \text{\AA}$, $\log(O32) = 0.8$, and $12 + \log(O/H) = 8.0$ ($0.2 Z_{\odot}$). For the [Roberts-Borsani et al. \(2016\)](#) sample, maximal O/Fe enhancement implies $Z_* = 0.04 Z_{\odot}$. These rough estimates suggest that metal-poor massive stars with $\lesssim 5\% Z_{\odot}$ power the ionizing spectra of the star-forming galaxies responsible for reionizing the universe.

6 SUMMARY & CONCLUSIONS

We have compiled a sample of 18 individual star-forming galaxies at $z = 1.4-3.7$ with detections of auroral $[O\ III]\lambda 4363$ or $[O\ III]\lambda 11663$, for which temperature-based nebular oxygen abundances can be derived independent of strong-line ratio calibrations. Four of these are galaxies with $[O\ III]\lambda 4363$ detections from the MOSDEF survey, three of which have not been previously published. We utilized this sample to investigate the chemical abundances and ionization states of star-forming regions at $z > 1$. For the first time, we have constructed metallicity scaling relations, including the mass-metallicity relation and fundamental metallicity relation, at $z > 1$ based purely on direct-method metallicities. The independently-constrained nebular metallicities enable us to unambiguously constrain the stellar metallicities and ionization parameters of these galaxies using photoionization models, providing unprecedented insight into the gas physical conditions in $z > 1$ H II regions. We summarize our main results and conclusions below.

(i) We investigated whether strong-line metallicity calibrations change with redshift by directly comparing the strong-line ratios O3, O2, R23, O32, and Ne3O2 at fixed direct-method metallicity for samples at $z \sim 0-2.2$ (Fig. 3). Over $12 + \log(O/H) = 7.7-8.1$, we find that O3 and R23 are saturated and are not useful metallicity indicators. The median values of the $z > 1$ auroral-line sample closely match the $z \sim 0$ high-redshift analogs of BKD18 to within ~ 0.1 dex in O/H at fixed line ratio. We suggest the use of the BKD18 high-redshift analog calibrations at $z > 1$, with O32 and Ne3O2 providing the most utility as these ratios are monotonic with metallicity over $7.7 < 12 + \log(O/H) < 8.1$. With *JWST*, spectroscopic measurements of O32 and Ne3O2

can be made to $z \sim 9$ and $z \sim 12$, respectively. Local H II region calibrations should not be utilized at $12 + \log(O/H) \lesssim 8.0$ for this set of strong-line ratios. Our auroral-line sample did not have sufficient $[N\ II]$ coverage and detections to investigate N/O and nitrogen-based metallicity indicators.

(ii) We construct the stellar mass—gas-phase metallicity relation using temperature-based metallicities for the first time at $z > 1$ (Fig. 4). We find a correlation between M_* and direct-method O/H (eq. 11). After correcting for SFR biases in the $z > 1$ sample, we find that metallicity decreases by 0.4 ± 0.1 dex from $z \sim 0$ to $z \sim 2.2$ at $\log(M_*/M_{\odot}) = 7.5-9.5$, consistent with results based on strong-line methods. We find tentative evidence for a M_* -SFR-O/H relation at $z \sim 2.2$ based on direct-method metallicities (Fig. 6). Galaxies at $z > 1$ have the same oxygen abundance of galaxies at $z \sim 0$ at fixed M_* and SFR to within 0.1 dex, suggesting that the FMR does not significantly evolve with redshift (Fig. 7).

(iii) Using photoionization models, we uniquely leverage the direct-method nebular metallicity measurements to obtain constraints on the ionization parameter, U , and stellar metallicity of massive stars, Z_* , in star-forming regions in the $z > 1$ auroral-line galaxies (Sec. 4). For the majority of the $z > 1$ auroral-line sample, we find that Z_* , which traces Fe/H, is lower than the nebular metallicity (i.e., O/H) on a solar abundance scale. This result implies super-solar O/Fe values, in contrast to typical $z \sim 0$ systems which have $Z_* = Z_{\text{neb}}$. The super-solar O/Fe values can be explained by a physically-motivated picture in which the young stellar populations of these galaxies have been enriched by Type II SNe that occur promptly following a star-formation event and are the dominant production channel for O, but have not yet been fully enriched by Type Ia SNe that are delayed $\sim 0.3-1$ Gyr and are the dominant producer of Fe-peak elements. The four MOSDEF $[O\ III]\lambda 4363$ emitters have ages ≤ 300 Myr, and are younger than 90% of MOSDEF galaxies matched in redshift and M_* .

(iv) On average, the $z > 1$ auroral-line sample has the same U as local galaxies and H II regions with the same O/H, and the same U and O/H as $z \sim 0$ galaxies matched in sSFR (Fig. 15). The high ionization parameters of the $z > 1$ sample are driven by their high sSFRs and low oxygen abundances, with U values as expected from local relations between U , sSFR, and O/H. We conclude that evolution in U at fixed O/H is not a significant driver of the evolution of strong-line ratios with redshift. Harder ionizing spectra at fixed O/H compared to the local universe are a cause of strong-line ratio evolution for our $z > 1$ auroral-line sample due to super-solar O/Fe. Due to a lack of $[N\ II]$ coverage and detections, we are unable to evaluate the role of N/O with the current sample and cannot draw conclusions about the positions of $z \sim 2$ galaxies in the $[N\ II]$ BPT diagram.

(v) The $z > 1$ auroral-line sample has significantly higher sSFR, O32, and emission-line equivalent widths than typical $z \sim 2.3$ galaxies (Figs. 16 and 17), indicating they are younger and more metal-poor than the bulk of the $z \sim 2$ star-forming population. It is therefore unclear if our results carry over to typical galaxies at these redshifts, in particular because stellar population age is expected to vary with M_* and sSFR. It is possible that $z \sim 2$ galaxies are a mixed population, where low-mass and starburst galaxies are young and have super-solar O/Fe, while more massive galaxies have lower levels of O/Fe enhancement, potentially solar O/Fe at

$\log(M_*/M_\odot) \gtrsim 10.5$. As a result of such variation, metallicity measurements would be biased as a function of M_* and SFR when assuming a single calibration for the full sample, affecting the measured shape of the MZR and M_* -SFR-O/H relation. O/Fe constraints for galaxies falling on the M_* -SFR relation and more massive, metal-rich galaxies are needed to obtain robust constraints on metallicity scaling relations in the high-redshift universe.

(vi) The properties of the $z > 1$ auroral-line sample are closely matched to those of extreme emission-line galaxies at $z \sim 2$ (Tang et al. 2018). We conclude that EELGs have super-solar O/Fe, but similar U to local galaxies with the same O/H. We find that typical $z \sim 2.3$ MOSDEF galaxies and EELGs form a tight sequence in O32 and $EW_0(H\beta)$ as a function of $EW_0([O\ III]\lambda 5007)$ across 2.5 orders of magnitude (eqs. 12 and 13).

(vii) The emission-line equivalent widths and sSFRs of $z > 6$ galaxies also match the properties of the $z > 1$ auroral-line sample. We extend our results to typical star-forming galaxies in the epoch of reionization, implying more efficient production of ionizing photons from Fe-poor massive stars. Because of a maximum stellar population age imposed by the age of the universe, all galaxies at $z > 6$ are expected to have super-solar O/Fe. We use the O32 and $EW_0(H\beta)$ vs. $EW_0([O\ III]\lambda 5007)$ relations to estimate the nebular and stellar metallicities of UV-luminous $z > 6$ galaxies, finding typical values of $Z_{\text{neb}} \sim 0.25 Z_\odot$ and $Z_* \sim 0.05 Z_\odot$.

Ultimately, a larger sample of $z > 1$ auroral-line emitters spanning a wider dynamic range in oxygen abundance is needed to make a full assessment of metallicity indicators across the range of metallicities spanned by large spectroscopic survey datasets. Such a sample would allow for tests of calibration shapes, not just normalization as performed in this work. Our results suggest that finding galaxies with $[O\ III]\lambda 4363$ that can be detected with current facilities can be achieved by identifying galaxies with $EW_0([O\ III]\lambda 5007) \gtrsim 300 \text{ \AA}$ and high SFR ($\gtrsim 10 M_\odot \text{ yr}^{-1}$), but this selection will only yield metal-poor, low-mass galaxies. Obtaining auroral $[O\ II]\lambda 7320, 7330$ measurements for massive, moderately metal-rich galaxies with high SFRs presents a potential avenue to extend the metallicity baseline, improving calibration tests and constraints on the mass-metallicity relation.

The ionizing spectrum of massive stars is so strongly tied to the production of emission lines that it is imperative to understand the properties of massive stars at low and high redshifts in order to extract robust star-formation rates, metallicities, and ionization state information from spectra. To gain a more complete picture of massive stars at high redshifts, we must constrain O/Fe of individual galaxies spanning the M_* and SFR range of the star-forming population. Reaching this goal will require auroral-line measurements and high-S/N FUV continuum spectroscopy of a large number of high-redshift galaxies over a wide dynamic range of properties. The increased sensitivity of *JWST* and 30 m-class telescopes will be needed to achieve this goal. Until that time, we must continue extrapolating from small samples with detailed observations to infer the chemical enrichment of the large spectroscopic datasets currently available at $z \sim 1 - 3$.

ACKNOWLEDGEMENTS

Based on data obtained at the W.M. Keck Observatory, which is operated as a scientific partnership among the California Institute of Technology, the University of California, and NASA, and was made possible by the generous financial support of the W.M. Keck Foundation. We acknowledge support from NSF AAG grants AST-1312780, 1312547, 1312764, and 1313171, archival grant AR-13907 provided by NASA through the Space Telescope Science Institute, and grant NNX16AF54G from the NASA ADAP program. We also acknowledge a NASA contract supporting the *Å*IJW-FIRST Extragalactic Potential Observations (EXPO) Science Investigation Team *Å*I (15-WFIRST15-0004), administered by GSFC. We additionally acknowledge the 3D-HST collaboration for providing spectroscopic and photometric catalogs used in the MOSDEF survey. We wish to extend special thanks to those of Hawaiian ancestry on whose sacred mountain we are privileged to be guests. Without their generous hospitality, the work presented herein would not have been possible.

REFERENCES

- Aggarwal K. M., Keenan F. P., 1999, *ApJS*, **123**, 311
 Andrews B. H., Martini P., 2013, *ApJ*, **765**, 140
 Asplund M., Grevesse N., Sauval A. J., Scott P., 2009, *ARA&A*, **47**, 481
 Atek H., et al., 2011, *ApJ*, **743**, 121
 Azadi M., et al., 2017, *ApJ*, **835**, 27
 Baldwin J. A., Phillips M. M., Terlevich R., 1981, *PASP*, **93**, 5
 Bayliss M. B., Rigby J. R., Sharon K., Wuyts E., Florian M., Gladders M. D., Johnson T., Oguri M., 2014, *ApJ*, **790**, 144
 Berg D. A., Skillman E. D., Croxall K. V., Pogge R. W., Moustakas J., Johnson-Groh M., 2015, *ApJ*, **806**, 16
 Berg D. A., Erb D. K., Auger M. W., Pettini M., Brammer G. B., 2018, *ApJ*, **859**, 164
 Bian F., Kewley L. J., Dopita M. A., 2018, *ApJ*, **859**, 175
 Blanc G. A., Kewley L., Vogt F. P. A., Dopita M. A., 2015, *ApJ*, **798**, 99
 Bouwens R. J., et al., 2012, *ApJ*, **752**, L5
 Bouwens R. J., Illingworth G. D., Oesch P. A., Caruana J., Holwerda B., Smit R., Wilkins S., 2015, *ApJ*, **811**, 140
 Brammer G. B., et al., 2012a, *ApJS*, **200**, 13
 Brammer G. B., et al., 2012b, *ApJ*, **758**, L17
 Bresolin F., Kudritzki R.-P., Urbaneja M. A., Gieren W., Ho I.-T., Pietrzyński G., 2016, *ApJ*, **830**, 64
 Brinchmann J., Charlot S., White S. D. M., Tremonti C., Kauffmann G., Heckman T., Brinkmann J., 2004, *MNRAS*, **351**, 1151
 Brown J. S., Martini P., Andrews B. H., 2016, *MNRAS*, **458**, 1529
 Bruzual G., Charlot S., 2003, *MNRAS*, **344**, 1000
 Calzetti D., Armus L., Bohlin R. C., Kinney A. L., Koornneef J., Storchi-Bergmann T., 2000, *ApJ*, **533**, 682
 Campbell A., Terlevich R., Melnick J., 1986, *MNRAS*, **223**, 811
 Cardamone C., et al., 2009, *MNRAS*, **399**, 1191
 Cardelli J. A., Clayton G. C., Mathis J. S., 1989, *ApJ*, **345**, 245
 Chabrier G., 2003, *PASP*, **115**, 763
 Christensen L., et al., 2012a, *MNRAS*, **427**, 1953
 Christensen L., et al., 2012b, *MNRAS*, **427**, 1973
 Coil A. L., et al., 2015, *ApJ*, **801**, 35
 Conroy C., Gunn J. E., White M., 2009, *ApJ*, **699**, 486
 Cowie L. L., Barger A. J., Songaila A., 2016, *ApJ*, **817**, 57
 Cresci G., Mannucci F., Curti M., 2019, *A&A*, **627**, A42

- Croxall K. V., Pogge R. W., Berg D. A., Skillman E. D., Moustakas J., 2015, *ApJ*, **808**, 42
- Croxall K. V., Pogge R. W., Berg D. A., Skillman E. D., Moustakas J., 2016, *ApJ*, **830**, 4
- Cullen F., Cirasuolo M., McLure R. J., Dunlop J. S., Bowler R. A. A., 2014, *MNRAS*, **440**, 2300
- Cullen F., et al., 2019, *MNRAS*, **487**, 2038
- Curti M., Cresci G., Mannucci F., Marconi A., Maiolino R., Esposito S., 2017, *MNRAS*, **465**, 1384
- Davé R., Finlator K., Oppenheimer B. D., 2012, *MNRAS*, **421**, 98
- Davé R., Rafieferantsoa M. H., Thompson R. J., Hopkins P. F., 2017, *MNRAS*, **467**, 115
- Davé R., Anglés-Alcázar D., Narayanan D., Li Q., Rafieferantsoa M. H., Appleby S., 2019, *MNRAS*, **486**, 2827
- De Rossi M. E., Bower R. G., Font A. S., Schaye J., Theuns T., 2017, preprint, ([arXiv:1704.00006](https://arxiv.org/abs/1704.00006))
- Dickey C. M., et al., 2016, *ApJ*, **828**, L11
- Dopita M. A., et al., 2006a, *ApJS*, **167**, 177
- Dopita M. A., et al., 2006b, *ApJ*, **647**, 244
- Dopita M. A., Kewley L. J., Sutherland R. S., Nicholls D. C., 2016, *Ap&SS*, **361**, 61
- Eldridge J. J., Stanway E. R., 2012, *MNRAS*, **419**, 479
- Eldridge J. J., Langer N., Tout C. A., 2011, *MNRAS*, **414**, 3501
- Ellison S. L., Patton D. R., Simard L., McConnachie A. W., 2008, *ApJ*, **672**, L107
- Erb D. K., Shapley A. E., Pettini M., Steidel C. C., Reddy N. A., Adelberger K. L., 2006, *ApJ*, **644**, 813
- Erb D. K., Pettini M., Shapley A. E., Steidel C. C., Law D. R., Reddy N. A., 2010, *ApJ*, **719**, 1168
- Erb D. K., Pettini M., Steidel C. C., Strom A. L., Rudie G. C., Trainor R. F., Shapley A. E., Reddy N. A., 2016, *ApJ*, **830**, 52
- Esteban C., García-Rojas J., Carigi L., Peimbert M., Bresolin F., López-Sánchez A. R., Mesa-Delgado A., 2014, *MNRAS*, **443**, 624
- Fensch J., et al., 2017, *MNRAS*, **465**, 1934
- Ferland G. J., et al., 2017, *RMxAA*, **53**, 385
- Finkelstein S. L., et al., 2012, *ApJ*, **758**, 93
- Finlator K., Davé R., 2008, *MNRAS*, **385**, 2181
- Fischer C. F., Tachiev G., 2014, MCHF/MCDHF Collection, Version 2, Ref No. 10 & 20, Available online at <http://physics.nist.gov/mchf>, National Institute of Standards and Technology, <http://physics.nist.gov/mchf>
- Fosbury R. A. E., et al., 2003, *ApJ*, **596**, 797
- Freeman W. R., et al., 2019, *ApJ*, **873**, 102
- García-Rojas J., Esteban C., 2007, *ApJ*, **670**, 457
- Gburek T., et al., 2019, arXiv e-prints, [p. arXiv:1906.11849](https://arxiv.org/abs/1906.11849)
- Grogin N. A., et al., 2011, *ApJS*, **197**, 35
- Hainline K. N., Shapley A. E., Kornei K. A., Pettini M., Buckley-Geer E., Allam S. S., Tucker D. L., 2009, *ApJ*, **701**, 52
- Hao C.-N., Kennicutt R. C., Johnson B. D., Calzetti D., Dale D. A., Moustakas J., 2011, *ApJ*, **741**, 124
- Henry A., et al., 2013, *ApJ*, **776**, L27
- Hoag A., et al., 2018, *ApJ*, **854**, 39
- Holden B. P., et al., 2016, *ApJ*, **820**, 73
- Horne K., 1986, *PASP*, **98**, 609
- Izotov Y. I., Stasińska G., Meynet G., Guseva N. G., Thuan T. X., 2006, *A&A*, **448**, 955
- James B. L., et al., 2014, *MNRAS*, **440**, 1794
- Jeřábková T., Hasani Zonoozi A., Kroupa P., Beccari G., Yan Z., Vazdekis A., Zhang Z. Y., 2018, *A&A*, **620**, A39
- Jones T., Martin C., Cooper M. C., 2015, *ApJ*, **813**, 126
- Kaasinen M., Bian F., Groves B., Kewley L. J., Gupta A., 2017, *MNRAS*, **465**, 3220
- Kaasinen M., Kewley L., Bian F., Groves B., Kashino D., Silverman J., Kartaltepe J., 2018, *MNRAS*, **477**, 5568
- Kashino D., Inoue A. K., 2019, *MNRAS*, **486**, 1053
- Kashino D., et al., 2017, *ApJ*, **835**, 88
- Kashino D., et al., 2019, *ApJS*, **241**, 10
- Kauffmann G., et al., 2003, *MNRAS*, **341**, 33
- Kewley L. J., Dopita M. A., 2002, *ApJS*, **142**, 35
- Kewley L. J., Ellison S. L., 2008, *ApJ*, **681**, 1183
- Kewley L. J., Dopita M. A., Leitherer C., Davé R., Yuan T., Allen M., Groves B., Sutherland R., 2013a, *ApJ*, **774**, 100
- Kewley L. J., Dopita M. A., Leitherer C., Davé R., Yuan T., Allen M., Groves B., Sutherland R., 2013b, *ApJ*, **774**, 100
- Kewley L. J., Zahid H. J., Geller M. J., Dopita M. A., Hwang H. S., Fabricant D., 2015, *ApJ*, **812**, L20
- Kewley L. J., et al., 2016, *ApJ*, **819**, 100
- Kobayashi C., Umeda H., Nomoto K., Tominaga N., Ohkubo T., 2006, *ApJ*, **653**, 1145
- Kobulnicky H. A., Kewley L. J., 2004, *ApJ*, **617**, 240
- Koekemoer A. M., et al., 2011, *ApJS*, **197**, 36
- Kojima T., Ouchi M., Nakajima K., Shibuya T., Harikane Y., Ono Y., 2017, *PASJ*, **69**, 44
- Kriek M., van Dokkum P. G., Labbé I., Franx M., Illingworth G. D., Mareschini D., Quadri R. F., 2009, *ApJ*, **700**, 221
- Kriek M., et al., 2015, *ApJS*, **218**, 15
- Labbé I., et al., 2013, *ApJ*, **777**, L19
- Lara-López M. A., et al., 2010, *A&A*, **521**, L53
- Leitherer C., Ekström S., Meynet G., Schaerer D., Agienko K. B., Levesque E. M., 2014, *ApJS*, **212**, 14
- Levesque E. M., Richardson M. L. A., 2014, *ApJ*, **780**, 100
- Lilly S. J., Carollo C. M., Pipino A., Renzini A., Peng Y., 2013, *ApJ*, **772**, 119
- Ly C., Malkan M. A., Rigby J. R., Nagao T., 2016, *ApJ*, **828**, 67
- Ma X., Hopkins P. F., Faucher-Giguère C.-A., Zolman N., Muratov A. L., Kereš D., Quataert E., 2016, *MNRAS*, **456**, 2140
- Maier C., Lilly S. J., Ziegler B. L., Contini T., Pérez Montero E., Peng Y., Balestra I., 2014, *ApJ*, **792**, 3
- Maiolino R., Mannucci F., 2019, *A&ARv*, **27**, 3
- Maiolino R., et al., 2008, *A&A*, **488**, 463
- Mannucci F., Cresci G., Maiolino R., Marconi A., Gnerucci A., 2010, *MNRAS*, **408**, 2115
- Marino R. A., et al., 2013, *A&A*, **559**, A114
- Masters D., et al., 2014, *ApJ*, **785**, 153
- Matthee J., Schaye J., 2018, *MNRAS*, **479**, L34
- McLean I. S., et al., 2012, in Society of Photo-Optical Instrumentation Engineers (SPIE) Conference Series. , [doi:10.1117/12.924794](https://doi.org/10.1117/12.924794)
- Momcheva I. G., et al., 2016, *ApJS*, **225**, 27
- Nakajima K., Ouchi M., 2014, *MNRAS*, **442**, 900
- Nomoto K., Tominaga N., Umeda H., Kobayashi C., Maeda K., 2006, *Nuclear Physics A*, **777**, 424
- Oey M. S., et al., 2007, *ApJ*, **661**, 801
- Oke J. B., Gunn J. E., 1983, *ApJ*, **266**, 713
- Osterbrock D. E., Ferland G. J., 2006, *Astrophysics of gaseous nebulae and active galactic nuclei*
- Patrício V., et al., 2016, *MNRAS*, **456**, 4191
- Patrício V., Christensen L., Rhodin H., Cañameras R., Lara-López M. A., 2018, *MNRAS*, **481**, 3520
- Peeples M. S., Shankar F., 2011, *MNRAS*, **417**, 2962
- Peimbert M., 1967, *ApJ*, **150**, 825
- Pérez-Montero E., 2014, *MNRAS*, **441**, 2663
- Pettini M., Pagel B. E. J., 2004, *MNRAS*, **348**, L59
- Pilyugin L. S., Grebel E. K., 2016, *MNRAS*, **457**, 3678
- Pilyugin L. S., Thuan T. X., 2005, *ApJ*, **631**, 231
- Pilyugin L. S., Mattsson L., Vílchez J. M., Cedrés B., 2009, *MNRAS*, **398**, 485
- Pilyugin L. S., Grebel E. K., Mattsson L., 2012, *MNRAS*, **424**, 2316
- Reddy N. A., Pettini M., Steidel C. C., Shapley A. E., Erb D. K., Law D. R., 2012, *ApJ*, **754**, 25
- Reddy N. A., et al., 2015, *ApJ*, **806**, 259
- Reddy N. A., et al., 2018, *ApJ*, **869**, 92

- Roberts-Borsani G. W., et al., 2016, *ApJ*, **823**, 143
- Robertson B. E., Ellis R. S., Furlanetto S. R., Dunlop J. S., 2015, *ApJ*, **802**, L19
- Salim S., et al., 2007, *ApJS*, **173**, 267
- Salim S., Lee J. C., Ly C., Brinchmann J., Davé R., Dickinson M., Salzer J. J., Charlot S., 2014, *ApJ*, **797**, 126
- Salim S., Lee J. C., Davé R., Dickinson M., 2015, *ApJ*, **808**, 25
- Sánchez S. F., et al., 2015, *A&A*, **574**, A47
- Sanders R. L., et al., 2015, *ApJ*, **799**, 138
- Sanders R. L., et al., 2016a, *ApJ*, **816**, 23
- Sanders R. L., et al., 2016b, *ApJ*, **825**, L23
- Sanders R. L., Shapley A. E., Zhang K., Yan R., 2017, *ApJ*, **850**, 136
- Sanders R. L., et al., 2018, *ApJ*, **858**, 99
- Savaglio S., et al., 2005, *ApJ*, **635**, 260
- Schneider F. R. N., et al., 2018, *Science*, **359**, 69
- Scudder J. M., Ellison S. L., Torrey P., Patton D. R., Mendel J. T., 2012, *MNRAS*, **426**, 549
- Senchyna P., et al., 2017, *MNRAS*, **472**, 2608
- Senchyna P., Stark D. P., Chevallard J., Charlot S., Jones T., Vidal García A., 2019, arXiv e-prints, p. arXiv:1904.01615
- Shapley A. E., Coil A. L., Ma C.-P., Bundy K., 2005, *ApJ*, **635**, 1006
- Shapley A. E., et al., 2015, *ApJ*, **801**, 88
- Shapley A. E., et al., 2019, *ApJ*, **881**, L35
- Shaw R. A., Dufour R. J., 1994, in Crabtree D. R., Hanisch R. J., Barnes J., eds, *Astronomical Society of the Pacific Conference Series Vol. 61, Astronomical Data Analysis Software and Systems III*. p. 327
- Skelton R. E., et al., 2014, *ApJS*, **214**, 24
- Smit R., et al., 2014, *ApJ*, **784**, 58
- Smit R., et al., 2015, *ApJ*, **801**, 122
- Speagle J. S., Steinhardt C. L., Capak P. L., Silverman J. D., 2014, *ApJS*, **214**, 15
- Stanway E. R., Eldridge J. J., 2018, *MNRAS*, **479**, 75
- Stanway E. R., Eldridge J. J., 2019, *A&A*, **621**, A105
- Stark D. P., 2016, *ARA&A*, **54**, 761
- Stark D. P., et al., 2013, *MNRAS*, **436**, 1040
- Stark D. P., et al., 2014, *MNRAS*, **445**, 3200
- Stasińska G., Tenorio-Tagle G., Rodríguez M., Henney W. J., 2007, *A&A*, **471**, 193
- Steidel C. C., et al., 2014, *ApJ*, **795**, 165
- Steidel C. C., Strom A. L., Pettini M., Rudie G. C., Reddy N. A., Trainor R. F., 2016, *ApJ*, **826**, 159
- Storey P. J., Sochi T., Badnell N. R., 2014, *MNRAS*, **441**, 3028
- Strom A. L., Steidel C. C., Rudie G. C., Trainor R. F., Pettini M., Reddy N. A., 2017, *ApJ*, **836**, 164
- Strom A. L., Steidel C. C., Rudie G. C., Trainor R. F., Pettini M., 2018, *ApJ*, **868**, 117
- Tang M., Stark D., Chevallard J., Charlot S., 2018, arXiv e-prints,
- Tayal S. S., 2007, *ApJS*, **171**, 331
- Toribio San Cipriano L., García-Rojas J., Esteban C., Bresolin F., Peimbert M., 2016, *MNRAS*, **458**, 1866
- Toribio San Cipriano L., Domínguez-Guzmán G., Esteban C., García-Rojas J., Mesa-Delgado A., Bresolin F., Rodríguez M., Simón-Díaz S., 2017, *MNRAS*, **467**, 3759
- Torrey P., et al., 2018, *MNRAS*, **477**, L16
- Torrey P., et al., 2019, *MNRAS*, **484**, 5587
- Tremonti C. A., et al., 2004, *ApJ*, **613**, 898
- Troncoso P., et al., 2014, *A&A*, **563**, A58
- Tsamis Y. G., Péquignot D., 2005, *MNRAS*, **364**, 687
- Villar-Martín M., Cerviño M., González Delgado R. M., 2004, *MNRAS*, **355**, 1132
- Wilson T. J., et al., 2019, *ApJ*, **874**, 18
- Yates R. M., Kauffmann G., Guo Q., 2012, *MNRAS*, **422**, 215
- Yuan T.-T., Kewley L. J., 2009, *ApJ*, **699**, L161
- Zahid H. J., Dima G. I., Kudritzki R.-P., Kewley L. J., Geller M. J., Hwang H. S., Silverman J. D., Kashino D., 2014a, *ApJ*, **791**, 130
- Zahid H. J., et al., 2014b, *ApJ*, **792**, 75

APPENDIX A: LITERATURE $z > 1$ AURORAL-LINE SAMPLE

In this appendix, we describe the details of the oxygen abundance and galaxy property calculations on a case-by-case basis for each of the [O III] λ 4363 and O III] λ 1663 emitters taken from the literature. We also explain why we do not include the claimed [O III] λ 4363 detection from Yuan & Kewley (2009) in our analysis.

A1 Literature [O iii] λ 4363 emitters

Brammer et al. (2012b) report a marginal 1.7σ detection of [O III] λ 4363 for SL2SJ02176-0513 (B18), a star-forming galaxy at $z = 1.847$ magnified by a factor of 19. We estimate zero nebular reddening according to the observed Balmer ratio of $H\delta/H\beta = 0.18 \pm 0.03$, assuming an intrinsic value of $H\delta/H\beta = 0.259$. The [O II] λ 3726,3729 doublet is not included in the *HST*/WFC3 G141 grism wavelength coverage. Following Brammer et al. (2012b), we instead assume a uniform distribution of [2.5, 9.0] for the [O III] λ 5007/[O II] λ 3726,3729 ratio (Erb et al. 2010; Atek et al. 2011) and the mean value of [O III] λ 5007/[O II] λ 3726,3729 = 5.75 for calculating the metallicity. This range of [O III]/[O II] values is typical of galaxies at the same stellar mass as B18 (see Fig. 17). The oxygen abundance under this set of assumptions is $12+\log(\text{O}/\text{H}) = 7.56^{+0.51}_{-0.25}$. We note that O^+ makes up at most 30% of O under the range of assumed [O III]/[O II] values, and the total oxygen abundance only varies by ± 0.06 dex. Properties of B18 are also reported in Berg et al. (2018) (see A2).

Christensen et al. (2012a,b) report a 3.4σ detection of [O III] λ 4363 for a lensed galaxy at $z = 1.8339$, Abell 1689 arc ID 31.1 (C12a), magnified by a factor of 26.6. Nebular reddening is estimated from $H\gamma$ and $H\beta$, with $H\delta/H\beta = 0.40 \pm 0.07$ corresponding to $E(\text{B}-\text{V})_{\text{gas}} = 0.31^{+0.35}_{-0.31}$, assuming an intrinsic ratio of $H\delta/H\beta = 0.468$. The direct-method oxygen abundance is $12+\log(\text{O}/\text{H}) = 7.46^{+0.23}_{-0.23}$. We adopt the rest-frame equivalent width reported in Stark et al. (2014, ID 876.330 therein) of $\text{EW}_0([\text{O III}]\lambda 4959, 5007 + \text{H}\beta) = 740 \pm 190 \text{ \AA}$, and determine $\text{EW}_0([\text{O III}]\lambda 5007)$ and $\text{EW}_0(\text{H}\beta)$ based on the measured O3 ratio.

Stark et al. (2013) report a detection of [O III] λ 4363 for CSWA 141 (S13) at $z = 1.425$ with a significance of 7.3σ . S13 is magnified by a factor of 5.5. Nebular reddening is estimated from $H\beta$, $H\gamma$, and $H\delta$, and is found to be small ($E(\text{B}-\text{V})_{\text{gas}} = 0.03$). The total oxygen abundance is $12+\log(\text{O}/\text{H}) = 7.96^{+0.07}_{-0.07}$. The stellar mass of S13 is $\log(M_*/M_\odot) = 8.33^{+0.10}_{-0.14}$ (private communication, D. Stark & R. Mainali).

A marginal 1.7σ detection of [O III] λ 4363 is reported by James et al. (2014) for CSWA 20 (J14), a star-forming galaxy at $z = 1.433$ magnified by a factor of 11.5. $H\alpha$, $H\beta$, and $H\gamma$ are used to determine nebular reddening. The total oxygen abundance of J14 based on [O III] λ 4363 is

$12+\log(\text{O}/\text{H}) = 8.13^{+0.35}_{-0.21}$. [Patrício et al. \(2018\)](#) report a stellar mass of $\log(M_*/M_\odot) = 10.3 \pm 0.3$ for J14, estimated by fitting the galaxy SED obtained from SDSS broadband photometry, with z-band being the reddest filter at $\lambda_{\text{rest}} \approx 3700 \text{ \AA}$. [James et al. \(2014\)](#) measure a line width of $34.9 \pm 0.7 \text{ km s}^{-1}$ for the narrow systemic component of strong nebular emission features in the spectrum of J14, which also display a broad blueshifted component. The high stellar mass of [Patrício et al. \(2018\)](#) is inconsistent with such narrow line widths for standard disk and spheroid geometries, requiring unphysically large virial coefficients to reconcile the two in dynamical modeling. Additionally considering systematic uncertainties in lens modeling and the lack of broadband photometry blueward of the Balmer break, we conclude that the reported stellar mass of J14 from [Patrício et al. \(2018\)](#) is not reliable and likely overestimates the true stellar mass. We do not report M_* or sSFR for J14 in Table 2.

A2 Literature O iii]λ1663,1666 emitters

[Christensen et al. \(2012a,b\)](#) report O iii]λ1663 detections for three strongly lensed galaxies at $z > 1$. Abell 1689 arc ID 31.1 (C12a) has detections of both O iii]λ1663 and O iii]λ4363. C12a has a total oxygen abundance of $12+\log(\text{O}/\text{H}) = 7.34^{+0.44}_{-0.70}$ based on O iii]λ1663. Despite a remarkable 21.2σ detection of O iii]λ1663, the uncertainty on the metallicity is very large due to the large uncertainty of the dust correction and the extreme sensitivity of O iii]λ1663/[O iii]λ5007 to reddening. The oxygen abundance derived using O iii]λ1663 is consistent with that based on [O iii]λ4363 (see A1), although the uncertainty is significantly lower when using [O iii]λ4363. We adopt the total oxygen abundance based on [O iii]λ4363 for this target.

SMACS J0304 (C12b) at $z = 1.9634$ has a 7.5σ detection of O iii]λ1663 ([Christensen et al. 2012a,b](#)). Nebular reddening is estimated using H α , H β , H γ , and H δ . The direct-method oxygen abundance is $12+\log(\text{O}/\text{H}) = 8.14^{+0.04}_{-0.04}$. [Christensen et al. \(2012a\)](#) note C12b as a merging system based on its complex morphology, with 5 distinct components at close projected separation ($\lesssim 20 \text{ kpc}$, uncorrected for magnification) in *HST* imaging.

A 12.7σ O iii]λ1663 detection is reported for M2031 (C12c; [Christensen et al. 2012a,b](#)). H β and H ϵ suggest little nebular reddening assuming an intrinsic ratio of $\text{H}\epsilon/\text{H}\beta = 0.159$ ([Osterbrock & Ferland 2006](#)). The total oxygen abundance is $12+\log(\text{O}/\text{H}) = 7.77^{+0.02}_{-0.30}$. C12c is an interacting system, with a companion located at the same redshift ($\Delta v < 50 \text{ km s}^{-1}$) and 11.2 kpc projected separation in the source plane ([Patrício et al. 2016](#)).

[James et al. \(2014\)](#) report a 2.4σ detection of O iii]λ1663 for the gravitationally-lensed galaxy CSWA 20 (J14), which also has a marginal detection of [O iii]λ4363 (see A1). The direct-method oxygen abundance derived from O iii]λ1663 is $12+\log(\text{O}/\text{H}) = 7.86^{+0.15}_{-0.14}$. The metallicity based on [O iii]λ4363 is $\sim 1\sigma$ consistent with this value. Given that both [O iii]λ4363 and O iii]λ1663 are marginally detected (1.7σ and 2.4σ , respectively), the derived O/H uncertainties are comparable, and the large sensitivity to reddening correction for O iii]λ1663, we utilize the metallicity based on [O iii]λ4363 for J14. Our results do not change

significantly when instead utilizing the O iii]λ1663-based metallicity.

[Bayliss et al. \(2014\)](#) present a 6.9σ O iii]λ1663 detection for a lensed star-forming galaxy at $z = 3.6252$ (B14). H β and H γ are both detected, but H γ is contaminated by skylines. The measured $\text{H}\gamma/\text{H}\beta = 0.52 \pm 0.02$ is 2.5σ inconsistent with the maximum value of 0.468 in the case of no nebular reddening ([Osterbrock & Ferland 2006](#)), again suggesting H γ is unreliable. Following [Bayliss et al. \(2014\)](#), we adopt $A_V = 1.0 \pm 0.2$ from their SED fitting and assume that the nebular and stellar reddening is equal. This assumption yields $12+\log(\text{O}/\text{H}) = 8.10^{+0.09}_{-0.08}$.

[Stark et al. \(2014\)](#) present 3.5σ detections of O iii]λ1663 for two lensed galaxies: Abell 860_359 at $z = 1.7024$ (S14a) and MACS 0451 ID 1.1b at $z = 2.0596$ (S14b). Nebular reddening is estimated from H α and H β for each source. [O ii]λ3726,3729 is not detected for either galaxy, but 2σ upper limits are reported. We adopt the 2σ [O ii] upper limit values when calculating the metallicity, and a uniform distribution between zero and 3σ for [O ii] when creating realizations for uncertainty estimation. Under this assumption, both objects are still dominated by doubly-ionized oxygen, with $\sim 20\%$ of O in O $^+$. Varying the assumed [O ii] values between zero and 3σ changes the total oxygen abundances by $< 0.07 \text{ dex}$. The derived direct-method oxygen abundances are $12+\log(\text{O}/\text{H}) = 8.05^{+0.11}_{-0.08}$ for S14a and $12+\log(\text{O}/\text{H}) = 7.31^{+0.09}_{-0.14}$ for S14b. The $\text{EW}_0([\text{O iii}]\lambda 5007)$ and $\text{EW}_0(\text{H}\beta)$ of 860_359 is inferred from the reported $\text{EW}_0([\text{O iii}]\lambda 4959, 5007 + \text{H}\beta) = 1550 \pm 150 \text{ \AA}$ based on the measured O3 ratio.

[Steidel et al. \(2014\)](#) present three unlensed galaxies from the KBSS survey with detections of O iii]λ1663. These galaxies are BX74 (Ste14a), BX418 (Ste14b), and BX660 (Ste14c) at $z = 2.1889$, 2.3054 , and 2.1742 , respectively, with 7.5σ , 7.7σ , and 5.5σ detections of O iii]λ1663. Line ratios for these three galaxies are presented in both [Steidel et al. \(2014\)](#) and [Erb et al. \(2016\)](#), where individual line fluxes were derived from the latter in [Patrício et al. \(2018\)](#). The rest-optical line ratios disagree between [Steidel et al. \(2014\)](#) and [Erb et al. \(2016\)](#), with the latter yielding significantly lower O/H for all three galaxies. We utilize the measurements in [Steidel et al. \(2014\)](#) because this work included a more robust treatment of differential slit losses between filters, resulting in more accurate line ratios. For all three galaxies, we use the combination of line ratios from [Steidel et al. \(2014\)](#) and H α fluxes from [Erb et al. \(2016\)](#) to derive observed line fluxes and uncertainties. We also take stellar masses from [Steidel et al. \(2014\)](#), where the photometry used for SED fitting was corrected for rest-optical emission-line contamination. We obtain SFRs, temperatures, densities, and metallicities that are consistent with the values reported in [Steidel et al. \(2014\)](#). The total oxygen abundances are $12+\log(\text{O}/\text{H}) = 8.03^{+0.06}_{-0.06}$ for Ste14a, $12+\log(\text{O}/\text{H}) = 8.10^{+0.02}_{-0.06}$ for Ste14b, and $12+\log(\text{O}/\text{H}) = 8.15^{+0.04}_{-0.06}$ for Ste14c.

[Kojima et al. \(2017\)](#) report a 6.5σ detection of O iii]λ1663 for COSMOS 12805 (K17), an unlensed galaxy at $z = 2.159$. A 2σ upper limit is reported for [O ii]λ3726,3729. We adopt the same strategy as for the two galaxies from [Stark et al. \(2014\)](#), finding a total oxygen abundance of $12+\log(\text{O}/\text{H}) = 8.26^{+0.03}_{-0.30}$. Assuming the 2σ [O ii] upper limit for the abundance calculation gives 34% of total O in the

singly-ionized state. The significant uncertainty of the [O II] flux and, consequently, the O^+ abundance is the cause of the large lower error on O/H .

Berg et al. (2018) present a very high S/N rest-UV spectrum of SL2SJ02176-0513 (B18) with $S/N > 50$ in each component of the O III] $\lambda\lambda 1661, 1666$ doublet. Rest-optical *HST*/grism spectroscopy has also revealed a marginal [O III] $\lambda 4363$ detection (Brammer et al. 2012b, see A1). We adopt the updated magnification factor and stellar mass of B18 from Berg et al. (2018). The rest-UV spectrum reveals an extremely high level of ionization based on strong nebular C IV and He II, and models presented in Berg et al. (2018) suggest $< 2\%$ of O is in O^+ with a non-negligible fraction in O^{3+} . We employ their oxygen ionization correction factor of $O/H = 1.055 \times O^{2+}/H$ and find the total oxygen abundance to be $12 + \log(O/H) = 7.53^{+0.09}_{-0.05}$ using O III] $\lambda 1663$. We adopt this metallicity value for B18, which is consistent with but better constrained than the abundance based on the marginal [O III] $\lambda 4363$ detection from Brammer et al. (2012b).

The O III] $\lambda 1663$ doublet is detected at 14.3σ significance for the highly-magnified Lynx arc at $z = 3.357$ (V04; Fosbury et al. 2003; Villar-Martín et al. 2004). Reddening cannot be estimated from Balmer lines since only $H\beta$ is available. Following Patricio et al. (2018), we assume zero nebular reddening based on SED modeling of the rest-optical and rest-UV spectrum (Villar-Martín et al. 2004). In the absence of a detection of [O II], we follow the same procedure as for the two galaxies from Stark et al. (2014). We note that the Lynx arc is highly ionized, with O^+ making up at most 4% of O (3σ upper limit), such that the [O II] non-detection has a negligible impact on the nebular metallicity determination. The total oxygen abundance is $12 + \log(O/H) = 7.76^{+0.04}_{-0.04}$. While a stellar mass is given in Villar-Martín et al. (2004), it is important to note that they only observe one bright knot of the highly-magnified arc with a particularly low mass-to-light ratio (possibly a single lensed H II region) and that the stellar mass is that of an instantaneous burst simple stellar population able to power the $H\beta$ emission. The stellar mass from Villar-Martín et al. (2004) thus only represents the mass of a star cluster ionizing the H II region, not the global stellar mass of the galaxy, and is not suitable for studying metallicity scaling relations with global galaxy properties.

A3 The case of the Yuan & Kewley (2009) [O III] $\lambda 4363$ detection

A detection of [O III] $\lambda 4363$ for Abell 1689 Lens 22.3 at $z = 1.706$ was presented in Yuan & Kewley (2009), with a magnification of 15.5. The reported [O III] $\lambda 4363$ flux is 0.27 ± 0.1 on a normalized scale where the $H\beta$ flux is 1.0. Yuan & Kewley (2009) measure a redshift from [O III] $\lambda 4363$ of $z = 1.696$ that is $\Delta z = 0.009$ lower than the redshift measured from strong rest-optical lines, $z = 1.705$. This redshift offset corresponds to a velocity offset of $\sim 1000 \text{ km s}^{-1}$ ($\Delta\lambda = 15 \text{ \AA}$ in the rest-frame), and calls into question the legitimacy of the [O III] $\lambda 4363$ detection given that [O III] $\lambda 4363$ emission should be at rest with respect to other rest-optical nebular emission lines. Based on the redshift from the strong lines ($z = 1.705$), the rest-frame centroid of the line in question is 4348 \AA , close to the wavelength of $H\gamma$ (4342 \AA). Given that the spectrum in Yuan & Kewley (2009) has a low spectral resolution of $R \sim 500$ (9 \AA resolution in the

rest-frame at $\lambda = 4350 \text{ \AA}$), we argue that $H\gamma$ was misidentified as [O III] $\lambda 4363$. Indeed, $H\gamma$ is almost always significantly stronger than [O III] $\lambda 4363$ (the case for every other source in our $z > 1$ auroral-line sample), and should be easily detected if [O III] $\lambda 4363$ is also detected unless $H\gamma$ is contaminated by a sky line. Yuan & Kewley (2009) report a detector response-corrected ratio of $H\alpha/H\beta = 5.03$. This Balmer ratio implies a nebular reddening of $E(B-V)_{\text{gas}} = 0.57$. Based on this $E(B-V)_{\text{gas}}$ value, the expected $H\gamma/H\beta$ ratio is 0.34, consistent with the reported [O III] $\lambda 4363/H\beta = 0.27 \pm 0.1$ from Yuan & Kewley (2009). We conclude that the claimed [O III] $\lambda 4363$ detection in Yuan & Kewley (2009) is in fact a misidentification of $H\gamma$, and exclude this source from our literature $z > 1$ auroral-line sample. Gburek et al. (2019) have recently obtained a deep $R \sim 3000$ spectrum of Lens 22.3 and confirmed that the line reported in Yuan & Kewley (2009) is $H\gamma$ and no significant [O III] $\lambda 4363$ is present.

APPENDIX B: CALIBRATION SAMPLE BIASES OF CURTI ET AL. (2017)

Curti et al. (2017) constructed $z \sim 0$ metallicity calibrations using stacked spectra in bins of line ratio in the O3 vs. O2 diagram. The stacked spectra only reached down to $12 + \log(O/H) \approx 8.4$, and C17 supplemented the calibration sample with individual galaxies meeting the original selection criteria that additionally had [O III] $\lambda 4363$ detected with $> 10\sigma$ significance. The C17 calibration fits are thus dominated by this [O III] $\lambda 4363$ -detected subsample at $12 + \log(O/H) \lesssim 8.4$, and will be affected by biases associated with the cut on [O III] $\lambda 4363$ S/N. To investigate biases in the C17 calibration sample, we have used their selection criteria to select the same $z \sim 0$ stacking sample from the MPA-JHU DR7 catalogs (Kauffmann et al. 2003; Brinchmann et al. 2004; Tremonti et al. 2004; Salim et al. 2007). We select the individual [O III] $\lambda 4363$ -detected subsample by further requiring $S/N > 10$ for [O III] $\lambda 4363$. We plot the C17 stacking sample (gray histogram) and [O III] $\lambda 4363$ -detected subsample (red points) in the SFR vs. M_* diagram in Figure B1. For comparison, we also show the mean $z \sim 0$ and $z \sim 2.3$ M_* -SFR relations from Fig. 5, and the median M_* and SFRs of the BKD18 high-redshift analog stacks (cyan squares).

We find that the vast majority of the C17 [O III] $\lambda 4363$ -detected subsample has low mass ($\log(M_*/M_\odot) \lesssim 9.5$) and lies significantly above the mean $z \sim 0$ M_* -SFR relation. The C17 [O III] $\lambda 4363$ -detected subsample is in fact coincident with the $z \sim 2.3$ M_* -SFR relation (blue dashed line) and the BKD18 high-redshift analogs, selected to have a similar offset in the BPT diagram as $z \sim 2$ galaxies. The C17 subset with $S/N > 10$ for [O III] $\lambda 4363$ thus has high-sSFR typical of high-redshift galaxies that has been found to correlate with extreme ISM conditions (Kewley et al. 2015; Kaasinen et al. 2017, 2018; Kashino & Inoue 2019). Consequently, the C17 calibrations trace extreme ISM conditions typical at $z > 1$ at $12 + \log(O/H) \lesssim 8.4$ where the individual [O III] $\lambda 4363$ -detected subsample dominates, and normal $z \sim 0$ ISM conditions only at $12 + \log(O/H) \gtrsim 8.4$ where the representative stacking sample dominates. The agreement between the $z > 1$ auroral-line sample and C17 calibrations in Fig. 3 does not indicate that $z \sim 0$ calibrations are applicable at

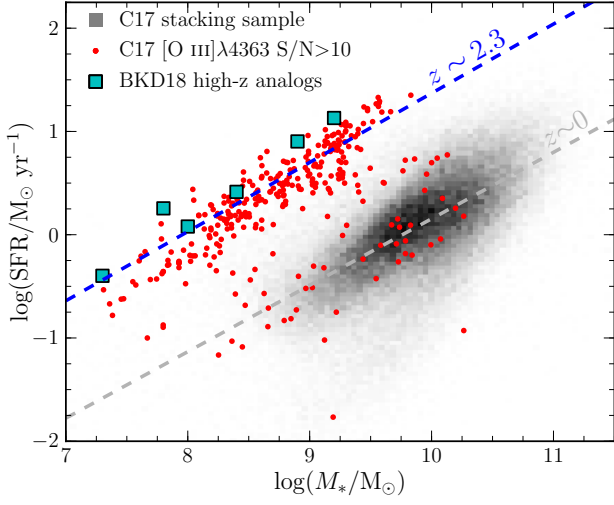


Figure B1. SFR vs. M_* for the Curti et al. (2017) $z \sim 0$ SDSS stacking sample (gray histogram) and the subset with $[\text{O III}]\lambda 4363$ at $>10\sigma$ (red points). The gray and blue dashed lines show the mean M_* -SFR relation at $z \sim 0$ and $z \sim 2.3$, respectively. The cyan squares show the median M_* and SFR for each bin of the Bian et al. (2018) high-redshift analog composites.

high redshifts, but instead is a result of the biased nature of the C17 calibrations at low metallicities.

This paper has been typeset from a $\text{T}_\text{E}\text{X}/\text{L}^\text{A}\text{T}_\text{E}\text{X}$ file prepared by the author.